

博士論文

Anhydrous Proton Conductivity of Imidazolium Hydrogen Dicarboxylates

(イミダゾールジカルボン酸塩の無水プロトン伝導性に関する研究)

砂入 允哉

博士論文

Anhydrous Proton Conductivity of
Imidazolium Hydrogen Dicarboxylates
(イミダゾールジカルボン酸塩の
無水プロトン伝導性に関する研究)

砂入 允哉

Contents

Chapter 1.

General Introduction	1
1.1. Proton migration in solids	1
1.2. Hydrous solid proton conductors	2
1.3. Anhydrous solid proton conductors	5
1.4. Anhydrous organic solid proton conductors	8
1.5. Organic acid–base crystalline proton conductors, imidazolium hydrogen dicarboxylates	11
1.6. The purpose of the research and structure of this thesis	14
1.7. Reference	17

Chapter 2.

Intrinsic Proton Conductivity and its Anisotropy Related to “Static”

Molecular Arrangements and H-bond Manners	21
2.1. Introduction	21
2.2. Experiments	22
2.3. Results and discussion	24
2.3.1. Crystal structure and thermal stability of imidazolium hydrogen succinate	24
2.3.2. Single crystal proton conductivity of imidazolium hydrogen succinate	27
2.3.3. Anisotropy of proton conductivity between directions parallel and perpendicular to the hydrogen-bond networks in imidazolium hydrogen succinate	31
2.3.4. Anisotropy of proton conductivity in the hydrogen-bond network of imidazolium hydrogen succinate	36
2.4. Conclusion	37
2.5. Reference	39

Chapter 3.

Effects of Proton Donating Abilities (pK_a) of Constituent Molecules as “Static”

Factor of Anhydrous Proton Conductivity	41
3.1. Introduction	41
3.2. Experiments	42
3.3.1. Crystal structures and anisotropy of the proton conductivities of imidazolium hydrogen glutarate and fumarate	44
3.3.2. The effect of the pK_a on the anhydrous proton conductivity	59
3.4. Conclusion	62
3.5. Reference	64

Chapter 4.

Effects of Molecular “Dynamics” on Anhydrous Proton Conductivity	65
4.1. Introduction	65
4.2. Experiments	67
4.3. Results and discussion	73
4.3.1. Activation of molecular motion of imidazolium cations and its effects on proton conduction in imidazolium hydrogen succinate	73
4.3.2. Local libration motion of imidazolium cations and its effect on the anhydrous proton conduction in the three analogue salts	84
4.3.3. Effects of molecular dynamics on proton conduction from viewpoint of molecular arrangements	98
4.4. Conclusion	103
4.5. Reference	105

Chapter 5.

General Conclusion	107
List of Publications	113
Acknowledgements	114

Chapter 1.

General Introduction

1.1. Proton migration in solids

Proton (hydrogen cation, H^+) migration plays an important role in solid materials, and thus has attracted much attention not only from the viewpoints of fundamental science such as quantum diffusion or tunneling of hydrogen atoms in materials, but also in the field of applied science because proton conducting materials are promising candidates for solid-state electrolytes in fuel cells, hydrogen separators, steam electrolyzers, sensors, metal protectors, and biological transport systems.¹⁾ In particular, a lot of researches have been focused on the development of highly proton conducting materials and the elucidation of the conduction mechanism, which are pivotal issues in the research field of proton conductors.

Among a lot of proton conducting solids developed ever, most of them are classified to hydrous proton conductors, in which proton conduction is mediated by water molecules. In the hydrous systems, there have been proposed two kinds of proton conduction mechanisms, vehicle and Grotthuss mechanisms.^{1a,1b,2,3)} In the vehicle mechanism,²⁾ protons are attached to H_2O molecules, and the protonated molecule itself diffuses in the material [Figure 1-1(a)]. The observed proton conductivity thus strongly depends on the density and diffusion rates of the protonated molecules.^{1b)} On the other hand, in the Grotthuss mechanism,³⁾ protons are transferred from one water molecule to another through hydrogen bonds (H-bonds) formed among the water molecules. During the proton transfer in this conduction mechanism, formation and breaking of H-bonds and local dynamics, that is, reorientation of the molecules, should continuously occur [Figure 1-1(b)]. Although the H-bonded network structure observed as the averaged structure is important, the reorientation of the H-bonded molecules can further

extend the network structure by forming transient H-bonds, thus is thought to be important in the Grotthuss mechanism. Therefore, the conductivity following this mechanism is considered to depend on reorientation rates of the water molecules.^{1b)}

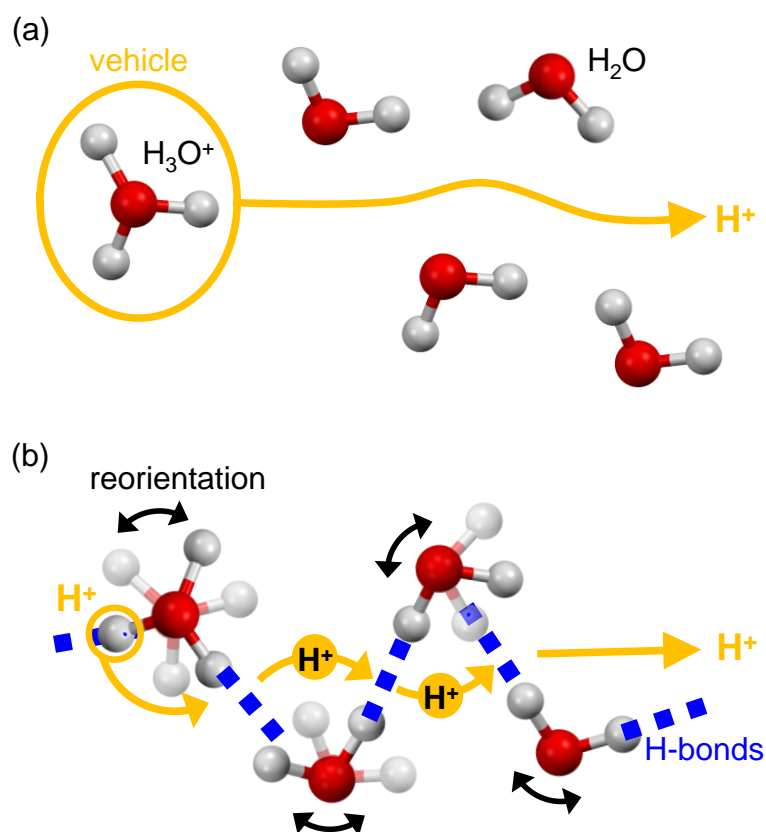


Figure 1-1. Schematic images of two kinds of proton conduction mechanisms, (a) vehicle and (b) Grotthuss mechanisms in the hydrous systems.

1.2. Hydrous solid proton conductors

As mentioned above, most of the reported proton conductors are hydrous systems showing proton conductivity under humidified conditions. For example, Nafion[®] [Figure 1-2(a)], the one of the most famous proton conducting organic polymer utilized in the fuel cells,⁴⁾ can uptake a lot of water molecules under humidified conditions below 100 °C, and shows high proton conductivity up to $10^{-1} \text{ S cm}^{-1}$ [Figure 1-2(b)].^{4b-e)} Here, protons are supplied by the sulfonic acid groups, and migrate via the sorbed water molecules by both the vehicle and Grotthuss

mechanisms, and vehicle mechanism becomes generally dominant with increasing temperature.

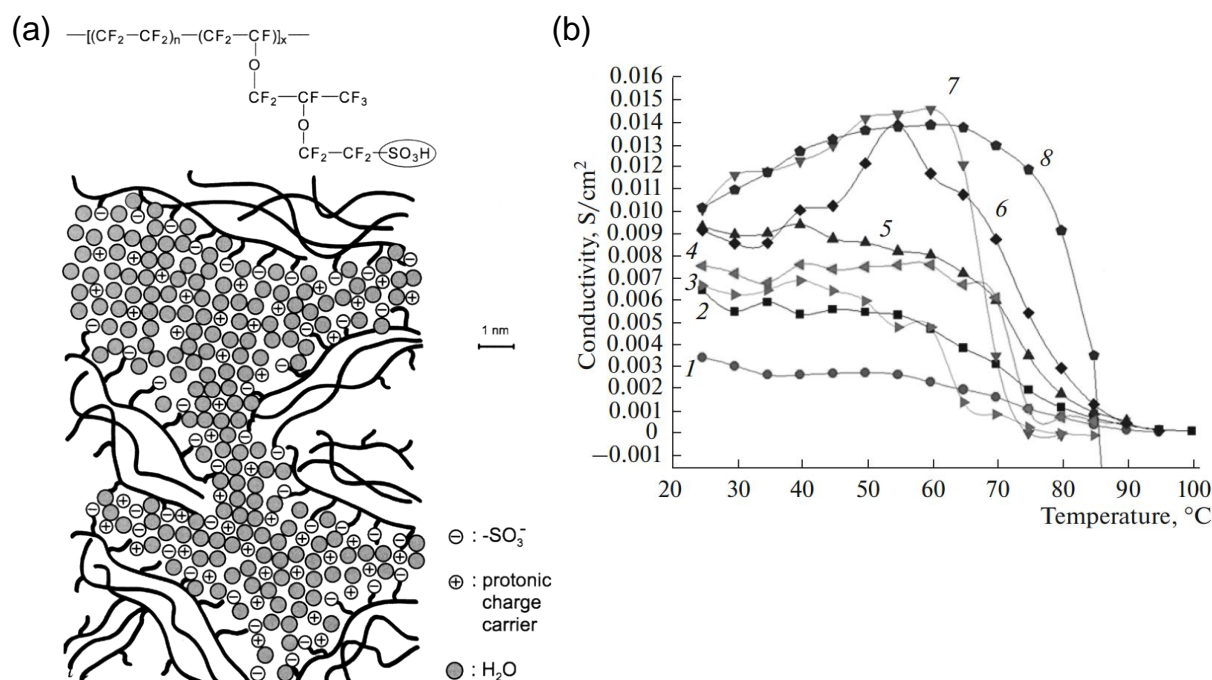


Figure 1-2. (a) (upper) General chemical structure and (lower) schematic image of the microstructures of Nafion[®] under humidified condition. {Reprinted with permission from [K. D. Kreuer, S. J. Paddison, E. Spohr, and M. Schuster, Chem. Rev. **104**, 4637 (2004)]. Copyright (2020) American Chemical Society.} (b) Temperature dependence of proton conductivities of humidified Nafion[®] membranes at 100% relative humidity (each sample was primarily exposed for 3 hours to 1: 0.05, 2: 0.025, 3: 2, 4: 1, 5: 0.1, 6: 3, 7: 0.5, 8: 0 mol/L hydrochloric acid solution). {This figure was published in [A. G. Ivanovaa, P. A. Il'in, A. A. Dmitrieva, O. A. Zagrebelnyy, A. Yu. Gruzinov, G. P. Kopitsa, I. Yu. Kruchinina, and O. A. Shilova, Glass Phys. Chem. **42**, 637 (2016)], Copyright Springer Nature (2020).}

As other examples of famous proton conducting solids, there are metal–organic frameworks (MOFs) constructed from metal ions coordinated by organic ligands forming two- or three-dimensional (2D or 3D) framework structures (Figure 1-3).⁵⁾ They have been attracted interests because they can show high proton conductivity up to 10^{-2} S cm⁻¹ mediated by water guest

molecules adsorbed in interlayer spaces or porous structures under highly humidified conditions.^{5a,d,g)} Typically, H^+ is supplied from acid functional groups of the organic ligands to the adsorbed water molecules. One of the advantages of MOFs is that the structures of the pores can be controlled by the choice of the metals and organic ligands, and the properties of the pores can also be modified by chemical functionalization of the ligands. For example, substitutions of the ligand functional groups with different acidities, that is, from $-H$ to $-NH_2$, $-OH$, or $-COOH$ changes the carrier concentration (*i.e.*, protonated water molecules), and thus affects the proton conductivity.^{5b)} Molecular arrangements of the water guest molecules depend on the structures of the pores, which also influences the proton conductivity. As in the case of the organic polymers, the proton conduction is realized by the vehicle and/or Grotthuss mechanisms.

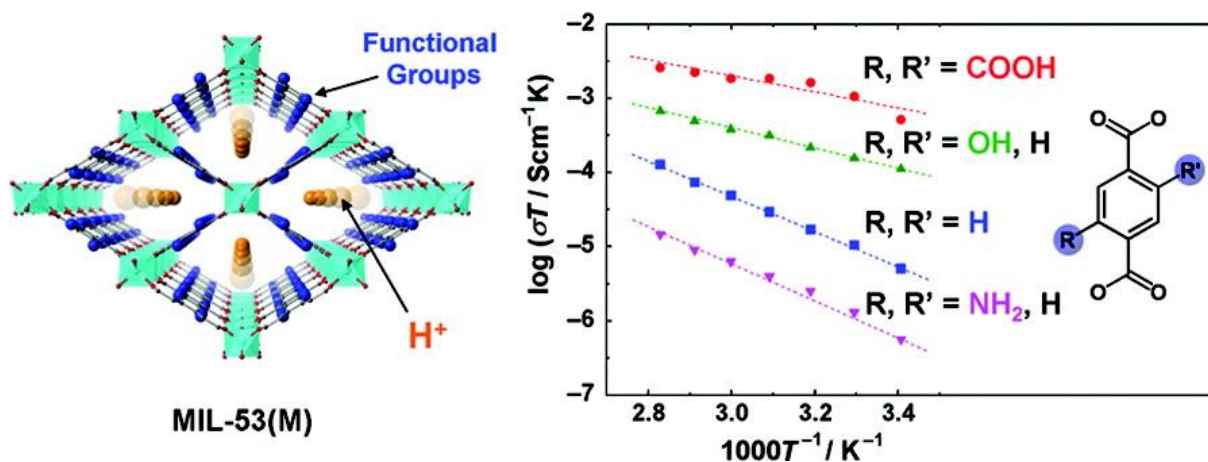


Figure 1-3. (left) A framework structure of a MOF with the ligand functional groups substituted from $-H$ to $-NH_2$, $-OH$, or $-COOH$ with different acidities [MIL-53(*M*)-*R* (*M* = Al or Fe, *R* = $-H$, $-NH_2$, $-OH$, or $-COOH$)] and (right) Arrhenius plots of $\log(\sigma T)$ for the MIL-53(*M*)-*R*. {Reprinted with permission from [A. Shigematsu, T. Yamada, and H. Kitagawa, J. Am. Chem. Soc. **133**, 2034 (2011)]. Copyright (2020) American Chemical Society.}

Although such hydrous proton conductors show high proton conductivity, they need

humidified conditions. Moreover, even under humidified conditions, they lose conductivity above 100 °C because of desorption of water molecules; decreasing conductivity with elevated temperature is shown in Figure 1-2(b). Consequently, anhydrous proton conductors, which can show proton conductivity without water molecules (*i.e.*, without humidification), have recently attracted much attention due to not only potential application for solid electrolytes above 100 °C but also scientific interests for the proton conduction mechanism mediated not by water molecules. Anhydrous proton conductivity can be realized by using molecules with proton donating/accepting ability (*e.g.*, amines, ammonia, phosphates, sulfates, carboxylates, *etc.*).

1.3. Anhydrous solid proton conductors

One of the simple strategies to realize the anhydrous proton conduction is to introduce the amphoteric guest molecules into polymer membranes or MOFs instead of water molecules. Actually, imidazole incorporated into MOFs and polymer membranes as guest molecules had been reported to show proton conductivity without humidified conditions.⁶⁾ Imidazole has not only proton donor/acceptor abilities similar to those of water but also a higher melting/boiling point, which give better high-temperature tolerance.^{6a)} For example, S. Kitagawa *et al.* have realized an anhydrous proton conductivity in a MOF up to 10^{-5} S cm⁻¹ at 120 °C by incorporation of the imidazole guest molecules into the pore of the MOF (Figure 1-4).^{6b)}

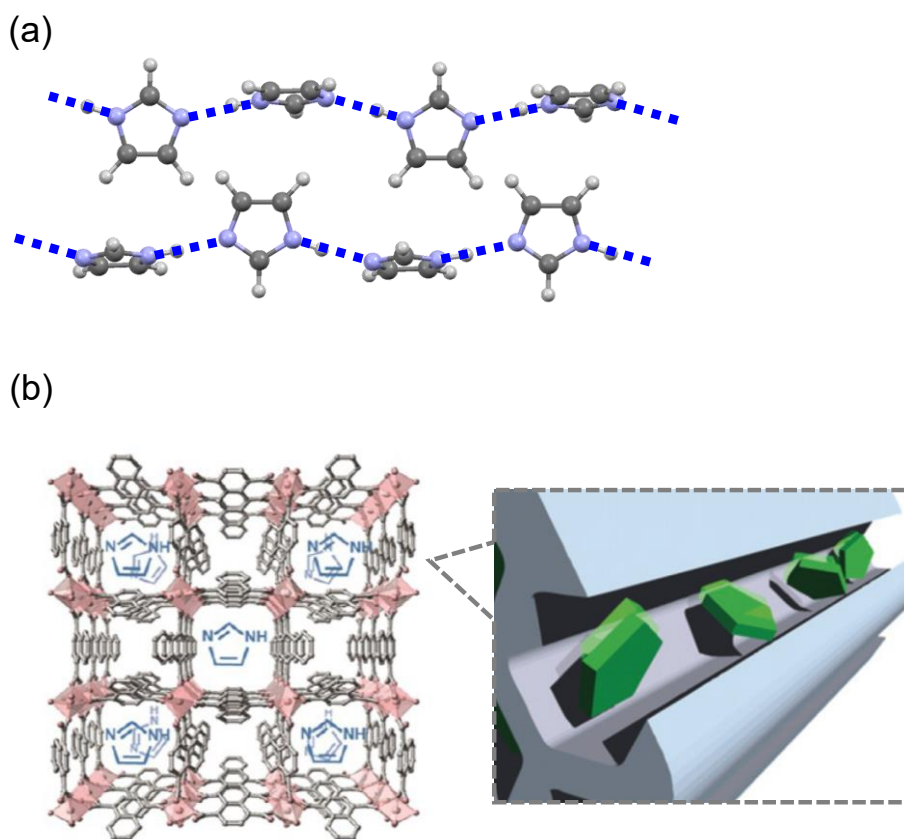


Figure 1-4. (a) The arrangements of imidazole molecules in the imidazole single crystal.⁷⁾ (b) Schematic images of imidazole guest molecules arranged in the framework of the MOFs showing higher proton conductivity than the imidazole single crystal.⁹⁾ {left: Reprinted with permission from [S. Horike, D. Umeyama, M. Inukai, T. Itakura, and S. Kitagawa, *Acc. Chem. Res.* **46**, 2376 (2013)]. Copyright (2020) American Chemical Society., right: This figure was published in [S. Bureekaew, S. Horike, M. Higuchi, M. Mizuno, T. Kawamura, D. Tanaka, N. Yanai, and S. Kitagawa, *Nat. Mater.* **8**, 831 (2009)], Copyright Springer Nature (2020).}

The other materials realizing the anhydrous proton conduction are molecular solids composed of the proton donors and acceptors forming H-bond networks. It is noted that the H-bonded molecular solids can show “intrinsic” proton conductivity without guest molecules, thus can show a peculiar conduction mechanism expected to be purely Grotthuss-type mechanism.

In fact, a series of inorganic salts consisting of metal cations and tetrahedral oxo-acid anions (*e.g.*, HSO_4^- , H_2PO_4^- , *etc.*) shows anhydrous proton conductivity realized by the Grotthuss-

type mechanism.¹⁰⁾ Protons migrate through the O–H···O H-bonds between the oxo-acid anions, accompanied with reorientation of the anions.^{10c,d,h)} Some of these salts show phase transition to the superprotonic conducting state ($> 10^{-3} \text{ S cm}^{-1}$) at high temperature, where orientational disorder of the oxo-acid anions results in an increase of the number of H-bond sites raising the symmetry of the crystal structure from monoclinic to cubic, and thus enhances proton conductivity (Figure 1-5). Although these materials show high proton conductivity applicable to solid-state electrolytes, there are problems such as dehydration and decomposition to polyphosphates and metaphosphates at the superprotonic conducting temperature.^{10h,11)} In these decades, improvements of the thermal stabilities at the superprotonic conducting phase and proton conductivity at lower temperature have been challenged, in which, however, material designs have gotten limited to the choice of metal species.

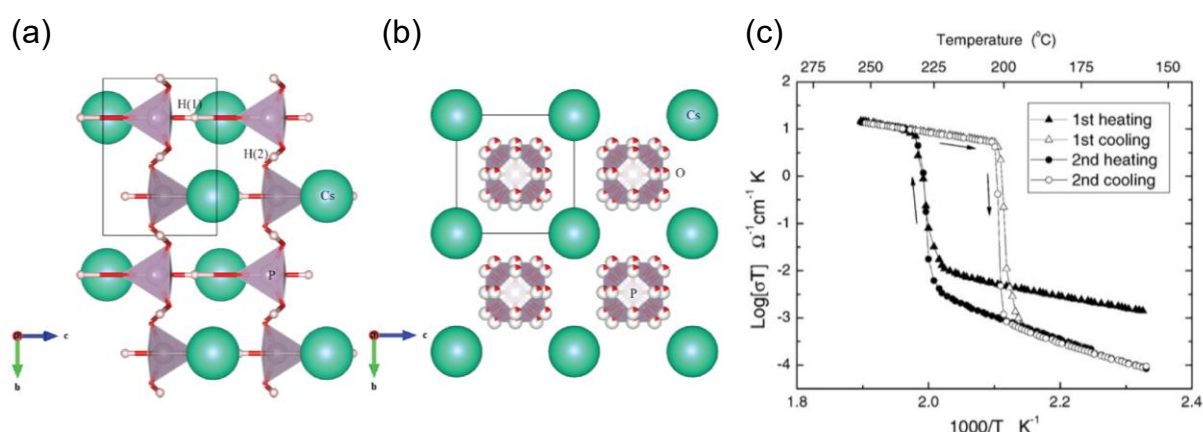


Figure 1-5. (a, b) Crystal structures of (a) the monoclinic paraelectric phase below 230 °C, and (b) the cubic superprotonic conducting phase above 230 °C. {Reprinted with permission from [G. Kim, F. Blanc, Yan-Yan Hu, and C. P. Grey, *J. Phys. Chem. C* **117**, 6504 (2013)]. Copyright (2020) American Chemical Society.} (c) Arrhenius plot [$\log(\sigma T)$ vs. $1000/T$] of CsH₂PO₄ (σ : proton conductivity, T : temperature). {Reproduced from [S. M. Haile, C. R. I. Chisholm, K. Sasaki, D. A. Boysen, and T. Uda, *Faraday Discuss.* **134**, 17 (2007)] with permission from The Royal Society of Chemistry.} In (a) and (b), green, red, white spheres represent cesium, oxygen, and hydrogen atoms, and purple tetrahedra represent phosphate units. In (c), the phase

transitions to the superprotonic conducting state are observed at around 230 °C in heating processes (conductivity was measured for two heating and cooling cycles).

1.4. Anhydrous organic solid proton conductors

Unlike the inorganic materials, organic materials have wide molecular/crystal structural variety, high designability, flexibility, *etc.* Thus, we can systematically design and synthesize proton conductors by utilizing the rich material designability, and investigate the structure–property relationship and proton conduction mechanism for development of anhydrous organic proton conductors with high performance. However, there have been only a few reports about anhydrous organic proton conductors, *e.g.*, imidazole, squaric acid derivatives, haloanilinium phosphates.^{9,12)}

A single crystal of imidazole [Figure 1-4(a)] shows proton conductivity under anhydrous condition. However, the value of proton conductivity is very low ($\sigma = 10^{-9} \text{ S cm}^{-1}$ at 80 °C).⁹⁾ On the other hand, as mentioned above, imidazole molecules introduced to the polymer membranes and MOFs showed higher proton conductivities ($\sigma = 10^{-5} - 10^{-3} \text{ S cm}^{-1}$) under anhydrous situations.⁶⁾ The improvement of proton conductivity indicates assembled arrangements of the imidazole molecules are important for the high proton conductivity of anhydrous imidazole-based solids [Figure 1-4(b)]. However, the molecular arrangements in the membranes and MOFs are difficult to be investigated in detail due to its low structural periodicity, which often makes the investigating methods complex.^{6d)} On the other hand, anhydrous organic crystals allow us to investigate the molecular arrangements and discuss its effects on proton conductivity in detail because of their crystalline nature.

Crystalline solids of squaric acid derivatives also showed anhydrous proton conductivity.^{12b)} H-bond network structures in the solids were modulated with chemical modifications of the squaric acid molecules [Figure 1-6(a)], which affected the proton conductivities (*e.g.*, *n*-butyl derivatives: $10^{-5} \text{ S cm}^{-1}$ at 110 °C, *tert*-butyl derivatives: $10^{-3} \text{ S cm}^{-1}$ at 110 °C). Also for

tetrahedral oxo-acid salts consisting of phosphate anions (HPO_4^{2-} , H_2PO_4^-) and haloanilinium cation derivatives [$a\text{-XAni}^+$ ($a = o, m$, and p positions, $X = \text{F, Cl, Br, and I}$)],^{12c)} the anhydrous proton conductivity was modulated by changing H-bond network structures [Figure 1-6(b)] of the phosphate anions associated with chemical modifications of $a\text{-XAni}^+$ cations. These results support not only the importance of H-bond network structures and molecular arrangements but also the potentials of organic materials for the systematic studies and material designs.

However, crystallinity of the squaric acid derivatives became lower with the chemical modifications than that of the crystal of squaric acid, and thus the molecular arrangements needed to be analyzed by the combination of powder X-ray diffraction experiments and its simulation analyses. In the haloanilinium phosphate salts, proton conducting paths are considered to be formed in the H-bond networks of phosphate anions, and thus the haloanilinium cation does not directly participate in the anhydrous proton conduction, that is, the proton conduction is realized by mainly the inorganic components with little contribution from the organic constituent molecules.

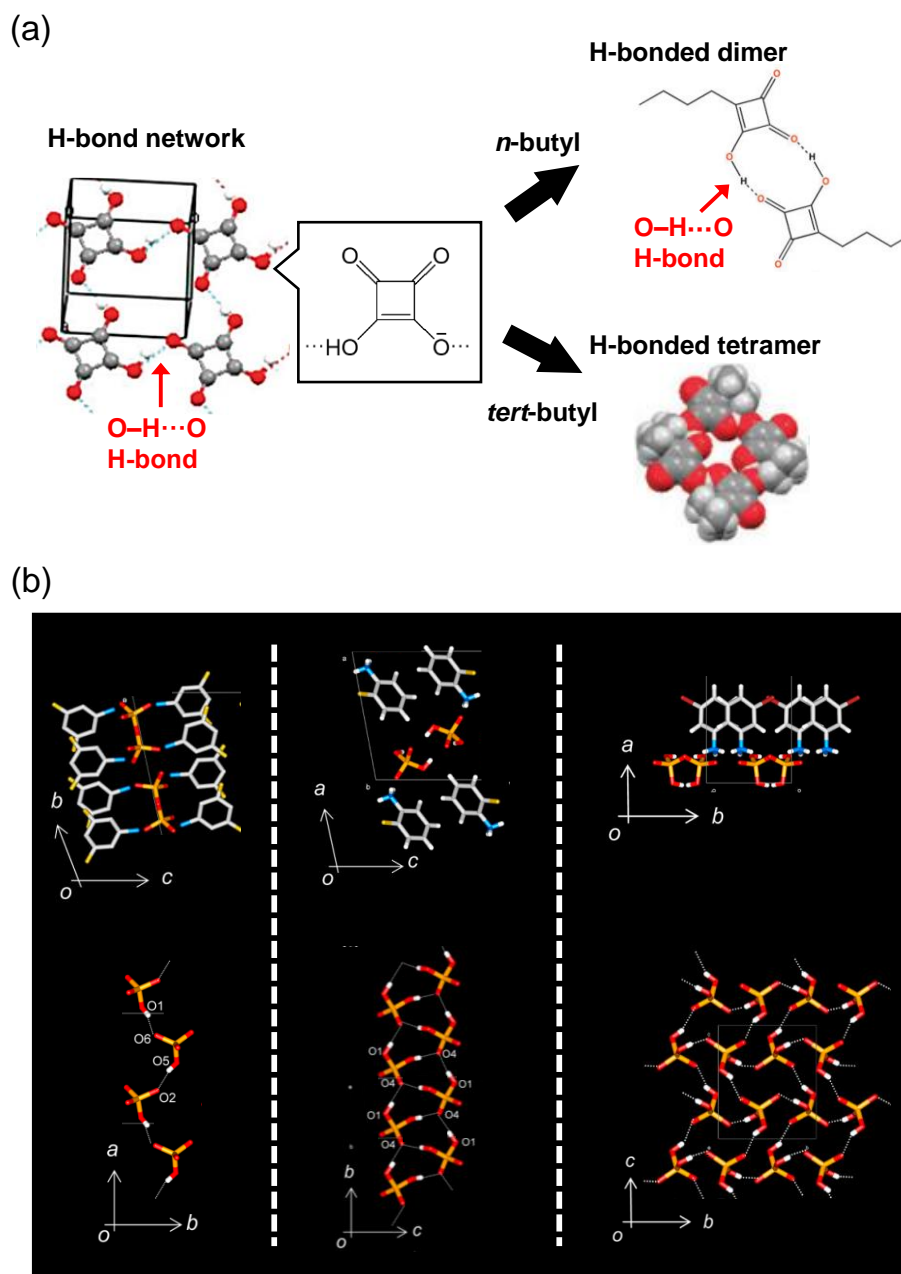


Figure 1-6. The H-bond network structures in (a) squaric acid derivatives and (b) haloanilinium [a -XAni⁺ ($a = o, m$, and p positions, X = F, Cl, Br, and I)] phosphate salts. {(a): Reproduced from [D. Basak, C. Versek, D. T. Toscano, S. Christensen, M. T. Tuominen, and D. Venkataraman, Chem. Commun. **48**, 5922 (2012)] with permission from The Royal Society of Chemistry., (b): Reprinted with permission from [Y. Yoshii, N. Hoshino, T. Takeda, and T. Akutagawa, J. Phys. Chem. C **119**, 20845 (2015)]. Copyright (2020) American Chemical Society.} In (a), H-bonded dimers or tetramers are formed in the H-bond networks in solids of the n - or $tert$ -butyl derivatives of squaric acid, respectively. In (b), the H-bond networks of

HPO_4^{2-} or H_2PO_4^- anions (lower) are modulated with changes of molecular packing (upper) associated with substitutions of $\alpha\text{-XAni}^+$ derivatives (left $[m\text{-FAni}^+]_2[\text{HPO}_4^{2-}]$: one-dimensional H-bond single chain, center $[o\text{-FAni}^+][\text{H}_2\text{PO}_4^-]$: one-dimensional H-bond ladder chain, right $[m\text{-BrAni}^+][\text{H}_2\text{PO}_4^-]$: two-dimensional H-bond network).

1.5. Organic acid–base crystalline proton conductors, imidazolium hydrogen dicarboxylates

In addition to the anhydrous organic proton conductors introduced in the previous section, purely organic acid–base H-bonded molecular crystals consisting of imidazole base combined with dicarboxylic acids, imidazolium hydrogen dicarboxylates (Figure 1-7), have also been reported to show anhydrous proton conductivities, which has been investigated relatively in detail among the previous researches of anhydrous proton conductivities of organic crystals.¹³⁾

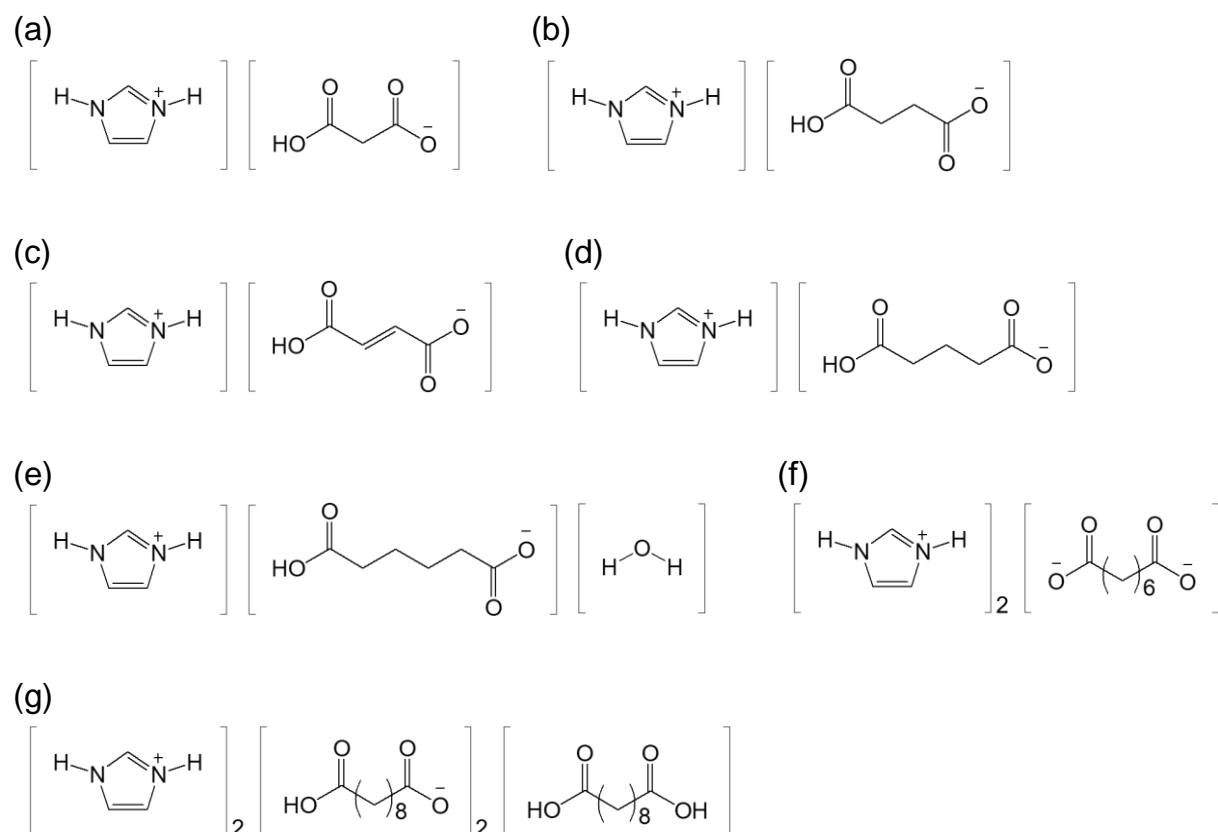


Figure 1-7. Chemical structures of the imidazolium hydrogen dicarboxylates: (a) Imidazolium

hydrogen malonate, (b) succinate, (c) fumarate, (d) glutarate, (e) adipate monohydrate, (f) bis(imidazolium) suberate, and (g) bis(imidazolium) bis(hydrogen sebacate) sebacic acid.

For example, for a series of the acid–base co-crystals using dicarboxylic acid derivatives [Figure 1-7 (a), (b), (d) – (g)], K. Pogorzelec-Glaser, *et al.* have investigated proton conductivities in the form of compressed pellets.^{13c,d,i)} They have prepared small single crystals by slow evaporation from acetone solution of imidazole and the corresponding dicarboxylic acid at room temperature. Because of the small size of the prepared crystals insufficient to operate single-crystal conductivity studies, they have powdered the crystals and compressed the powder into the pellet samples. As shown in Figure 1-8, the salts have similar layered structures of two-dimensional (2D) H-bond networks to each other [Figure 1-8(a)], and despite the fact that no water molecules are included, show relatively high proton conductivity [Figure 1-8(b): imidazolium hydrogen malonate: 10^{-5} S cm⁻¹, glutarate: 10^{-7} S cm⁻¹, adipate monohydrate: 10^{-5} S cm⁻¹, diimidazolium suberate: 10^{-6} S cm⁻¹, diimidazolium hydrogen disbacate sebacic acid: 10^{-3} S cm⁻¹ at 17 °C].^{13c)} In particular, the σ of the succinate salt [Figure 1-7(b)] reaches 10^{-3} S cm⁻¹ at around 127 °C, as shown in Figure 1-9(a).^{13d)} This high conductivity has been considered to be related to their 2D H-bond network structures formed by both the acid and base molecules. [Figure 1-9(b), (c)].^{13c,d,h,j)} Although the anhydrous proton conduction in the imidazolium hydrogen dicarboxylates is believed to be realized based upon the Grotthuss-type mechanism, the proton conduction mechanism has not fully been revealed due to the lack of single-crystal studies, as only the molecular dynamics in powdered sample have been investigated by solid-state NMR.^{13e–h)} The single-crystal studies of anhydrous proton conductivity can reveal the “intrinsic” proton conductivity related to arrangements and properties of the constituent molecules, which provides crucial insights into not only the origins and mechanisms of the anhydrous proton conduction but also the guideline for material design of the high performance anhydrous organic proton conductors.

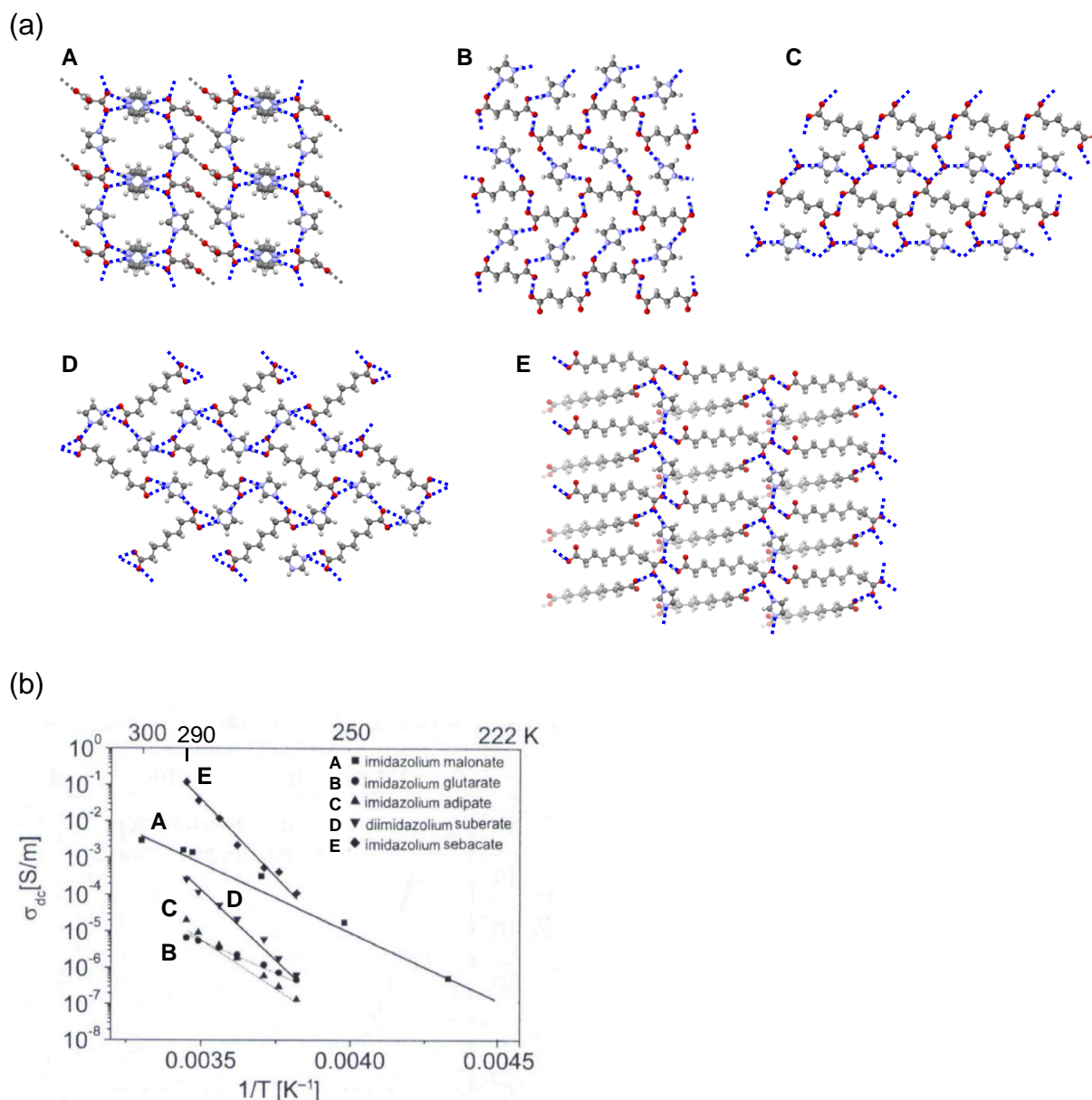


Figure 1-8. (a) The H-bond networks and (b) Arrhenius plots of proton conductivity (σ_{dc}) [$\text{S m}^{-1} = 10^{-2} \text{ S cm}^{-1}$] for the compressed pellets of a series of imidazolium hydrogen dicarboxylates {**A**: imidazolium hydrogen malonate [the chemical structure is shown in Figure 1-7 (a)], **B**: imidazolium hydrogen glutarate [Figure 1-7 (d)], **C**: imidazolium hydrogen adipate monohydrate [Figure 1-7 (e)], **D**: bis(imidazolium) suberate [Figure 1-7 (f)], **E**: bis(imidazolium) bis(hydrogen sebacate) sebacic acid [Figure 1-7 (g)]}.^{13b)} {(b): Reproduced from [Materials Science-Poland 2006, 24, 1, 245]}

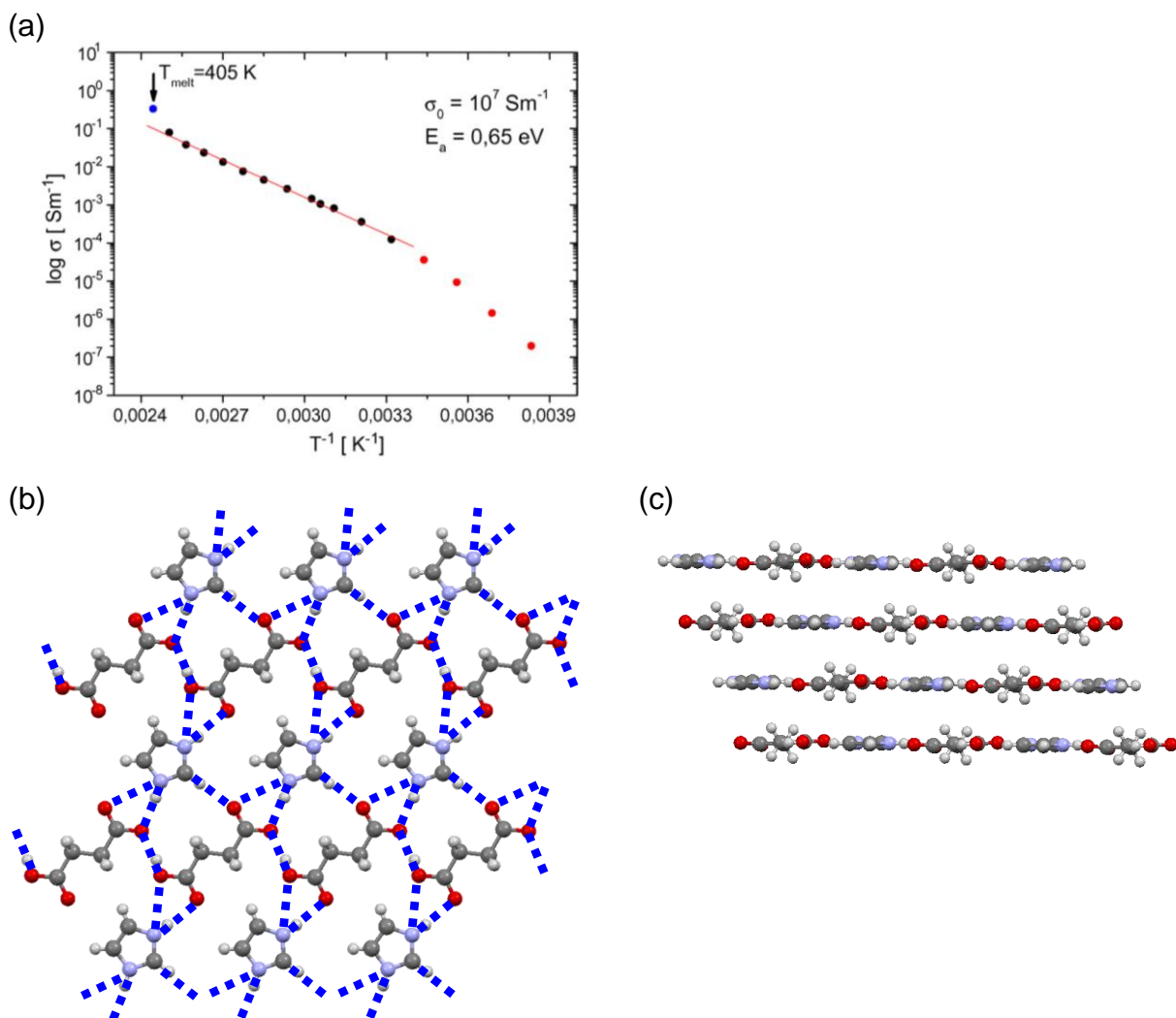


Figure 1-9. (a) Arrhenius plots of (σ) [S m⁻¹ = 10⁻² S cm⁻¹] for the compressed pellet of imidazolium hydrogen succinate [the chemical structure is shown in Figure 1-7 (b)]. {This figure was published in [K. Pogorzelec-Glaser, Cz. Pawlaczyk, A. Pietraszko, and E. Markiewicz, J. Power Sources **173**, 800 (2007)], Copyright Elsevier (2020).} (b) The H-bond network and (c) its stacking structure of the succinate salt.^{12a)}

1.6. The purpose of the research and structure of this thesis

The purpose of this research is to elucidate the origins and mechanisms of the anhydrous proton conductivity of imidazolium hydrogen dicarboxylates by systematic studies of single-crystal proton conductivity, in relation with molecular arrangements and dynamics of constituent molecules. Relationship between the proton conductivity and the “static” factors,

i.e., the molecular arrangements and proton donating abilities of the constituent molecules, and the effect of the molecular “dynamics” on the proton conductivity was investigated by using high-quality single crystals of a series of the imidazolium hydrogen dicarboxylates. In this thesis, intrinsic proton conductivity of the imidazolium hydrogen dicarboxylates obtained by using single crystals and its relationship with the “static” and “dynamics” factors are discussed over the following four chapters.

In Chapter 2, intrinsic proton conductivity without contributions from grain boundaries in the imidazolium hydrogen succinate (**1**) [see Figure 1-7(b) in Section 1.5] revealed by the single-crystal conductivity measurements is introduced and compared to the conductivity of the compressed powder (pellet) samples reported in the literature.^{13d)} In addition, anisotropy of the proton conductivity and its relationship with H-bond manners and molecular arrangements are discussed. Interestingly, the observed anisotropy demonstrates the importance of the H-bond network structure and the H-bonds between imidazole and dicarboxylic acid in the proton conduction, providing information of important “static” factors related to the crystal structure in the anhydrous proton conduction.

In Chapter 3, in order to investigate effects of proton donating abilities (pK_a) of the constituent molecules as another “static” factor related to molecular properties, the proton conductivities within the H-bond networks are compared between **1** and its analogue salts, imidazolium hydrogen glutarate (**2**) [see Figure 1-7(d) in Section 1.5] and imidazolium hydrogen fumarate (**3**) [Figure 1-7(c) in Section 1.5]. The proton conductivity is higher as difference of pK_a (ΔpK_a) between the dicarboxylic and conjugated acid of imidazole is smaller. This result indicates that the ΔpK_a is another important “static” factor for realization of the anhydrous proton conductivity of these salts. On the other hand, interestingly, the conductivities of **1** and **2** showed non-linear increases with elevated temperature in Arrhenius plots while that of **3** showed linear increase, which cannot be described only by the effects of the ΔpK_a .

In Chapter 4, in addition to the “static” factors for the anhydrous proton conductivity

discussed in the previous chapters, molecular “dynamics” of imidazolium cation investigated by high temperature single-crystal X-ray structure analyses for **1** and solid-state ^2H NMR spectroscopies using powder of imidazolium- d_3 (Im- d_3) hydrogen glutarate (**2- d_3**) and fumarate (**3- d_3**) are described. By comparison of the dynamics with the molecular arrangements in the H-bond networks, effects on the proton conduction are discussed. The libration motions of imidazolium cations were observed in the range of proton conducting temperatures for all the three salts, and their libration angles showed a relationship consistent with that of proton conductivities within the H-bond networks. Based on the discussion taking in account of the “static” factors, the author concludes that the molecular “dynamics” of imidazolium cation promote the anhydrous proton conduction of the imidazolium hydrogen dicarboxylates synergistically with the “static” factors such as the H-bond network structures and molecular arrangements.

The Chapter 5 is the conclusion of this thesis. The results of this research are summarized, and the significance of the obtained knowledge and future prospects are described in this chapter.

1.7. Reference

- 1) (a) P. Colomban: *Proton conductors: Solids, membranes and gels—materials and devices*, Cambridge, Cambridge University Press, U.K., 1992. (b) K. D. Kreuer, Chem. Mater. **8**, 610 (1996). (c) H. Iwahara, Solid State Ionics **86**, 9 (1996). (d) T. Norby, Solid State Ionics **125**, 1 (1999). (e) T. Norby, Nature **410**, 877 (2001). (f) B. C. H. Steele, and A. Heinzel, Nature **414**, 345 (2001). (g) K. D. Kreuer, S. J. Paddison, E. Spohr, and M. Schuster, Chem. Rev. **104**, 4637 (2004). (h) P. Knauth and M. L. Di Vona: *Solid State Proton Conductors: Properties and Applications in Fuel Cells*, John Wiley & Sons, Ltd., Chichester, U.K., 2012. (i) M. R. Karim, K. Hatakeyama, M. Koinuma, and S. Hayami, J. Mater. Chem. A **5**, 7243 (2017).
- 2) K. D. Kreuer, W. Weppner, and A. Rabenau, Angew. Chem., Int. Ed. Engl. **21**, 208 (1982).
- 3) (a) C. J. D. van Grotthuss, Ann. Chim. **58**, 54 (1806). (b) N. Agmon, Chem. Phys. Lett. **244**, 456 (1995).
- 4) (a) T. D. Gierke, G. E. Munn, and F. C. Wilson, J. Polym. Sci. Polym. Phys. Edn. **19**, 1687 (1981). (b) P. C. Rieke and N. E. Vanderborgh, J. Membr. Sci. **32**, 313 (1987). (c) Y. Sone, P. Ekdunge, and D. Simonsson, J. Electrochem. Soc. **143**, 1254 (1996). (d) S. J. Paddison, G. Bender, K. D. Kreuer, N. Nicoloso, and T. A. Zawodzinski Jr., J. New. Mater. Electrochem. Syst. **3**, 293 (2000). (e) K. D. Kreuer, J. Membr. Sci. **185**, 29 (2001). (f) S. Slade, S. A. Campbell, T. R. Ralph, and F. C. Walsh, J. Electrochem. Soc. **149**, A1556 (2002). (g) K. Schmidt-Rohr and Q. Chen, Nat. Mater. **7**, 75 (2008). (h) D. K. Paul, R. McCreery, and K. Karan, J. Electrochem. Soc. **161**, F1395 (2014). (i) A. G. Ivanovaa, P. A. Il'in, A. A. Dmitrieva, O. A. Zagrebelnyy, A. Yu. Gruzinov, G. P. Kopitsa, I. Yu. Kruchinina, and O. A. Shilova, Glass Phys. Chem. **42**, 637 (2016).
- 5) (a) M. Sadakiyo, T. Yamada, and H. Kitagawa, J. Am. Chem. Soc. **131**, 9906 (2009). (b) A. Shigematsu, T. Yamada, and H. Kitagawa, J. Am. Chem. Soc. **133**, 2034 (2011). (c) S. C. Sahoo and T. K. Banerjee, J. Am. Chem. Soc. **133**, 17950 (2011). (d) N. C. Jeong, B.

- Samanta, C. Y. Lee, O. K. Farha, and J. T. Hupp, *J. Am. Chem. Soc.* **134**, 51 (2012). (e) S. Kim, K. W. Dawson, B. S. Gelfand, J. M. Taylor, and G. K. H. Shimizu, *J. Am. Chem. Soc.* **135**, 963 (2013). (f) M. Sadakiyo, T. Yamada, and H. Kitagawa, *J. Am. Chem. Soc.* **136**, 13116 (2014). (g) J. M. Taylor, S. Dekura, R. Ikeda, and H. Kitagawa, *Chem. Mater.* **27**, 2286 (2015). (h) P. G. M. Mileo, S. Devautour-Vinot, G. Mouchaham, F. Faucher, N. Guillou, A. Vimont, C. Serre, and G. Maurin, *J. Phys. Chem. C* **120**, 24503 (2016). (i) Y. Yu, J. Zhu, J. Liu, Y. Yan, and X. Song, *Dalton Trans.* **46**, 9157 (2017). (j) S. S. Park, A. J. Rieth, C. H. Hendon, and M. Dincă, *J. Am. Chem. Soc.* **140**, 2016 (2018).
- 6) (a) K. D. Kreuer, *Solid State Ionics* **97**, 1 (1997). (b) S. Bureekaew, S. Horike, M. Higuchi, M. Mizuno, T. Kawamura, D. Tanaka, N. Yanai, and S. Kitagawa, *Nat. Mater.* **8**, 831 (2009). (c) S. Horike, D. Umeyama, M. Inukai, T. Itakura, and S. Kitagawa, *J. Am. Chem. Soc.* **134**, 7612 (2012). (d) E. Eisbeinm, Jan-Ole Joswig, and G. Seifert, *J. Phys. Chem. C* **118**, 13035 (2014). (e) Y. Ye, L. Zhang, Q. Peng, Guan-E Wang, Y. Shen, Z. Li, L. Wang, X. Ma, Qian-Huo Chen, Z. Zhang, and S. Xiang, *J. Am. Chem. Soc.* **137**, 913 (2015). (f) Feng-Ming Zhang, Long-Zhang Dong, Jun-Sheng Qin, W. Guan, J. Liu, Shun-Li Li, M. Lu, Ya-Qian Lan, Zhong-Min Su, and Hong-Cai Zhou, *J. Am. Chem. Soc.* **139**, 6183 (2017).
- 7) B. M. Craven, R. K. McMullan, J. D. Bell, and H. C. Freeman, *Acta Crystallogr. B* **33**, 2585 (1977).
- 8) S. Horike, D. Umeyama, M. Inukai, T. Itakura, and S. Kitagawa, *Acc. Chem. Res.* **46**, 2376 (2013).
- 9) A. Kawada, A. R. McGhie, and M. M. Labes, *J. Chem. Phys.* **52**, 3121 (1970).
- 10) (a) A. I. Baranov, L. Shuvalov, and N. Shchagina, *JETP Lett.* **36**, 459 (1982). (b) A. I. Baranov, V. P. Khiznichenko, and L. A. Shuvalov, *Ferroelectrics* **100**, 135 (1989). (c) A. I. Baranov, B. V. Merinov, A. V. Tregubchenko, V. P. Khiznichenko, L. A. Shuvalov, and N. M. Schagina, *Solid State Ionics* **36**, 279 (1989). (d) W. Münch, K. D. Kreuer, U. Traub, and J. Maier, *Solid State Ionics* **77**, 10 (1995). (e) T. Norby, M. Friesel, and B. E. Mellander,

- Solid State Ionics **77**, 105 (1995). (f) S. M. Haile, D. A. Boysen, C. R. I. Chisholm, and R. B. Merle, Nature **410**, 910 (2001). (g) D. A. Boysen and S. M. Haile, Chem. Mater. **15**, 727 (2003). (h) S. M. Haile, C. R. I. Chisholm, K. Sasaki, D. A. Boysen, and T. Uda, Faraday Discuss. **134**, 17 (2007). (i) G. Kim, F. Blanc, Yan-Yan Hu, and C. P. Grey, J. Phys. Chem. C **117**, 6504 (2013).
- 11) (a) J. Otomo, T. Tamaki, S. Nishida, S. Q. Wang, M. Ogura, T. Kobayashi, C. J. Wen, H. Nagamoto, and H. Takahashi, J. Appl. Electrochem. **35**, 865 (2005). (b) Y. K. Taninouchi, T. Uda, Y. Awakura, A. Ikeda, and S. M. Haile, J. Mater. Chem. **17**, 3182 (2007). (c) Y. K. Taninouchi, T. Uda, and Y. Awakura, Solid State Ionics **178**, 1648 (2008). (d) A. I. Baranov, E. M. Kopnin, V. V. Grebenev, A. Sin, Y. Dubitsky, P. Caracino, Phys. Status. Solidi. A **206**, 36 (2009). (e) C. R. I. Chisholm, D. A. Boysen, A. B. Papandrew, S. Zecevic, S. Cha, K. A. Sasaki, Á. Varga, K. P. Giapis, and S. M. Haile, Electrochem. Soc. Interface **18**, 53 (2009). (f) A. V. Nikiforov, R. W. Berg, and N. J. Bjerrum, Ionics **24**, 2761 (2018).
- 12) (a) N. Yutronic, J. Merchan, P. Jara, V. Manriquez, O. Wittke, and G. Gonzalez, Supramol. Chem. **16**, 411 (2004). (b) D. Basak, C. Versek, D. T. Toscano, S. Christensen, M. T. Tuominen, and D. Venkataraman, Chem. Commun. **48**, 5922 (2012). (c) Y. Yoshii, N. Hoshino, T. Takeda, and T. Akutagawa, J. Phys. Chem. C **119**, 20845 (2015). (d) M. Pulst, J. Balko, Y. Golitsyn, D. Reichert, K. Busse, and J. Kressler, Phys. Chem. Chem. Phys. **18**, 6153 (2016).
- 13) (a) J. C. MacDonald, P. C. Dorrestein, and M. M. Pilley, Cryst. Growth Des. **1**, 29 (2001). (b) J. Garbarczyk, and K. Pogorzelec-Glaser, Z. Kristallogr.-New Cryst. Struct. **218**, 567 (2003). (c) K. Pogorzelec-Glaser, J. Garbarczyk, Cz. Pawlaczyk, and E. Markiewicz, Mater. Sci.-Pol. **24**, 245 (2006). (d) K. Pogorzelec-Glaser, Cz. Pawlaczyk, A. Pietraszko, and E. Markiewicz, J. Power Sources **173**, 800 (2007). (e) A. Rachocki, K. Pogorzelec-Glaser, A. Pietraszko, and J. Tritt-Goc, J. Phys. Condens. Matter. **20**, 505101 (2008). (f) A. Rachocki, K. Pogorzelec-Glaser, and J. Tritt-Goc, App. Magn. Reason. **34**, 163 (2008). (g) M. Mizuno,

M. Chizuwa, T. Umiyama, Y. Kumagai, T. Miyatou, R. Ohashi, T. Ida, M. Tansho, and T. Shimizu, *Hyperfine Interact.* **230**, 95 (2015). (h) T. Umiyama, R. Ohashi, T. Ida, and M. Mizuno, *Chem. Lett.* **42**, 1323 (2013). (i) P. Ławniczak, K. Pogorzalec-Glaser, A. Pietraszko, and B. Hilczer, *Solid State Ionics* **306**, 25 (2017). (j) Y. Hori, T. Ida, and M. Mizuno, *Phys. Chem. Chem. Phys.* **19**, 16857 (2017).

Chapter 2.

Intrinsic Proton Conductivity and its Anisotropy Related to “Static” Molecular Arrangements and H-bond Manners

2.1. Introduction

As summarized in Chapter 1, anhydrous organic crystalline proton conductors are one of the critical materials to reveal the mechanism of the anhydrous proton conduction, and the imidazolium hydrogen dicarboxylates are attracting because they can be systematically investigated within similar 2D hydrogen-bond (H-bond) network structures.¹⁾ The proton conductivity of the imidazolium hydrogen succinate (**1**) [see Figure 1-7(b) in Section 1.5]²⁾ was as high as $\sim 10^{-3} \text{ S cm}^{-1}$ in the form of a pellet,³⁾ as mentioned in Section 1.5. On the other hand, the conductivity in the form of a single crystal has never been examined, which limits the understanding of the conduction mechanism. The scarce study with a single crystal form may originate from the difficulty in the preparations of the high-quality single crystals with sufficiently large sizes required to reveal the relationship between the proton conductivity and the crystal structures. In this study, high-quality single crystals of **1** were grown by a modified preparation method,²⁾ and the alternating-current (ac) impedances were measured along various crystal directions. The direct measurements using a single crystal provided the intrinsic proton conductivity of the sample itself⁴⁾ without contributions of grain boundaries, that were inevitably included in those using the compressed pellet samples.^{4b,c)} Through the direct method, the intrinsic proton conductivity of **1** was successfully determined for the first time. Based on these data, the relationship between the proton conductivity and “static” factors related to the crystal structure was discussed, including the molecular arrangements and H-bond manners.

2.2. Experiments

Preparation of single crystals

Single crystals of **1** were prepared by the modified method based on that described in the literatures.^{2,3)} All chemicals were commercially available and used as received. Imidazole [681 mg, 10 mmol, Wako Pure Chemical Industries (purity > 98%)] and succinic acid [1181 mg, 10 mmol, Wako Pure Chemical Industries (purity > 99.5%)] were suspended in a mixed solvent of dehydrated methanol [25 mL, Wako Pure Chemical Industries (purity > 99.8%)] and dehydrated acetonitrile [25 mL, Wako Pure Chemical Industries (purity > 99.8%)]. This suspension was stirred at 40 °C until all the materials were completely dissolved (about 10 min). The resulting solution was slowly evaporated for 3 days in an incubator (35 °C), and then the resulting precipitates were collected by filtration and washed with ethyl acetate to give the desired material as colorless crystals (see Figure 2-3 in Section 2.3.1).

Single-crystal X-ray structure analyses

The crystal structures of **1** were identified¹⁾ and the crystallographic orientations of the prepared single crystals were determined by X-ray diffraction analyses using a Rigaku Mercury II diffractometer with Mo $K\alpha$ radiation ($\lambda = 0.71073$ Å) at room temperature. The crystal structures were solved by direct methods using the SIR2008 program. Refinements were carried out by a full-matrix least-squares method using Crystal Structure 4.3.2 (Rigaku Corporation), in which the anisotropic temperature factors are refined for all the atoms.

Thermal analyses

In order to determine the temperature ranges of the ac impedance measurements for the single crystals of **1**, thermal stability of the crystals of **1** was evaluated by means of differential scanning calorimetry (DSC) using a Netzsch DSC 200 F3-T21 Maia calorimeter with an Al as a reference. The single crystals (3.6 mg) were encapsulated in an Al pan and the heat flow was

measured upon the heating of the sample from 20 to 300 °C with a rate of 5 °C min⁻¹ under nitrogen gas flow.

Alternating-current impedance spectroscopy

The ac impedance spectroscopy measurements were carried out by the two-probe method using a Solartron Impedance Analyzer SI 1260 and Dielectric Interface 1296. As-grown single crystals of **1** were cut into blocks (typical size of 0.4 × 0.4 × 0.5 mm³) to expose the desired faces for the anisotropy measurements. The probes were separately attached to the two opposite sides by using silver paste and gold wires (ϕ : 15 μ m). Note that this combination (silver paste and gold wires) is one of the typical materials to make the electrical contact for measuring the ac conductivity of solid materials, including proton conductors.⁴⁾ The complex impedance of the samples was measured from 1 Hz to 1 MHz in the temperature range of room temperature to 116 °C, where the temperature was controlled by using a home-built high-temperature oven. The upper limit temperature (116 °C) was set to the temperature at which melting of the crystal starts to appear in the DSC curve (see Figure 2-2 in Section 2.3.1).

The fitting for obtained complex impedance planes (Cole–Cole plots) was operated by using the circuit consisting of one series resistance R_{con} and one parallel combination of a single resistance R_{sam} and capacitance C_{sam} (see inset of Figure 2-4 in Section 2.3.2). The ac conductivity σ_{ac} values were estimated from $\sigma_{\text{ac}} = |Z(\omega)|^{-1} (l / S)$, where $Z(\omega)$ is the complex impedance at frequency ω of the applied electric field, l and S are thickness and area of samples. The σ_{ac} at 1 Hz was defined as the proton conductivity σ because 1 Hz was the lowest frequency of the region where the σ_{ac} was independent to frequency and thus corresponds to the direct-current (dc) conductivity in the temperature region of 103 to 116 °C.

2.3. Results and discussion

2.3.1. Crystal structure and thermal stability of imidazolium hydrogen succinate

In this thesis, the author established a reproducible method for the crystallization of **1** by modifying a method in the previous studies.^{2,3)} After screening of the crystallization conditions, the author found the optimum concentration of the starting materials (0.2 mol/L) and crystallization temperature (slow cooling from 40 °C to room temperature for 3 – 10 days) to grow large, high-quality single crystals of **1** with a typical size of $0.5 \times 0.7 \times 1.0 \text{ mm}^3$ (see the details in Experimental Section). The crystal structures of the prepared single crystals of **1** were identified to the same structure with the reported one in the literature²⁾ (Table 2-1 and Figure 2-1).

Table 2-1. Crystallographic data of **1**.

Sample	the literature ²⁾	this research
Temperature (°C)	24	20
Crystal system	triclinic	triclinic
Space group	<i>P</i> –1	<i>P</i> –1
<i>a</i> (Å)	6.583(2)	6.595(3)
<i>b</i> (Å)	7.421(3)	7.431(3)
<i>c</i> (Å)	9.648(2)	9.672(3)
α (°)	67.89(3)	67.859(10)
β (°)	73.91(2)	73.984(12)
γ (°)	81.40(3)	81.429(13)
Volume (Å ³)	419.02	421.5(3)
<i>Z</i>	2	2
<i>D</i> _{calc} (g cm ^{–1})	1.476	1.467
λ (Å)	0.71069	0.71073
<i>R</i> _{int}	—	0.0172
<i>R</i> ₁ (<i>I</i> > 2.00σ(<i>I</i>))	0.0375	0.0442
<i>wR</i> ₂ (all reflections)	0.1382	0.1333
GOF	1.031	1.052
CCDC number	1211266	1957600

As shown in Figure 2-1(a) and (b), the crystal of **1** is composed of 2D sheet structures, in which the imidazolium cations (Im) and succinate anions (Suc) are connected with H-bonds.¹⁾ Two N–H moieties of the Im molecule are connected to oxygen atoms of the carboxylate group in Suc molecule with d_{NO} of 2.72 Å (red dashed lines) and 2.87 Å (brown dashed lines), and also form short contacts with the adjacent oxygen atoms of the Suc molecule with d_{NO} = 3.05, 3.15 Å (blue dashed lines). In addition, it has a C–H···O short contact (gray dashed lines, d_{CO} = 3.08 Å) between the Im and Suc molecules. Furthermore, there is an O–H···O H-bond between the Suc molecules (green dashed lines, d_{OO} = 2.49 Å). On the other hand, although the shortest C···C distance (3.39 Å, black arrows) between the 2D networks is less than the sum of van der Waals (vdW) radii (3.40 Å), no effective H-bonds are found between these 2D networks [Figure 2-1(c)]. The shortest N···O distances between the networks are 3.50 and 3.56 Å (blue and red arrows) which are much longer than the sum of vdW radii of N and O atoms (3.07 Å).⁵⁾

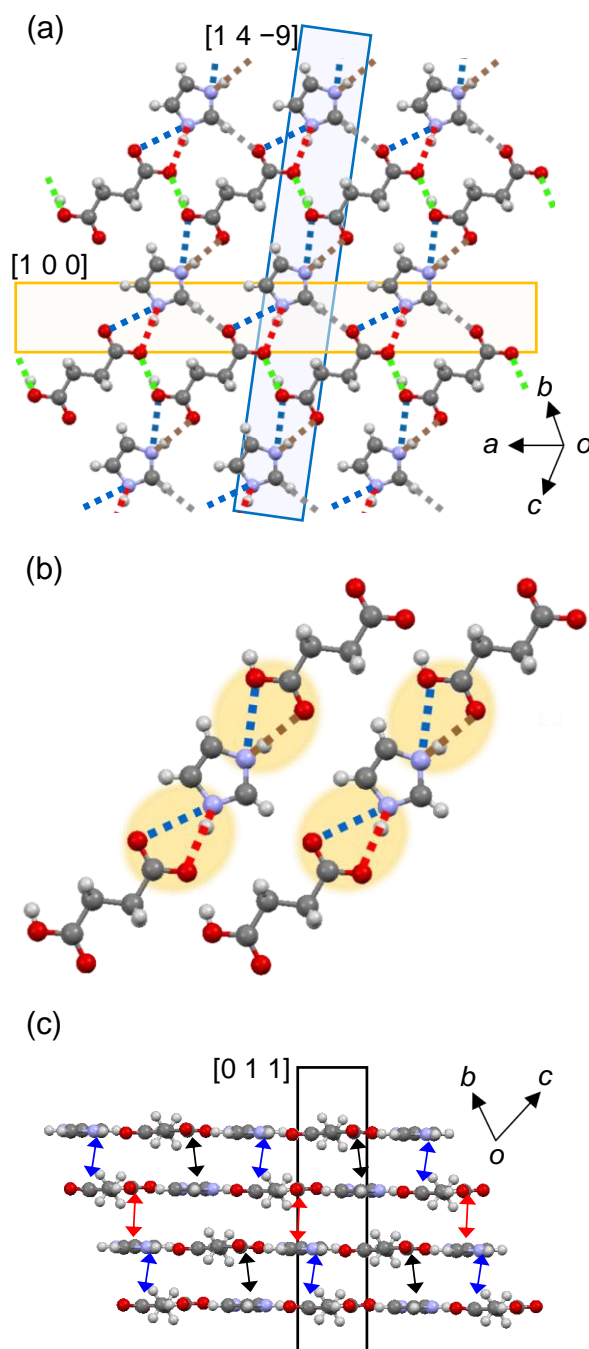


Figure 2-1. Crystal structure of **1**.²⁾ (a) 2D H-bond network structure (red, blue, light blue, and brown dashed lines: N–H···O H-bonds, green dashed lines: O–H···O H-bonds, gray dashed lines: C–H···O contacts), (b) N–H···O H-bonds around imidazolium cations, and (c) stacking arrangement of the 2D H-bond networks. In (c), black arrows represent short C···O contacts, and blue and red arrows represent shortest N···O distances, respectively. Proton conductivity measurements of **1** were carried out in the [1 0 0], [1 4 –9], and [0 1 1] directions [shown in (a) and (c)].

Prior to the proton conductivity measurements using a single crystal of **1**, thermal stability was investigated. The single crystals of **1** showed an endothermic process starting from 116 °C in the DSC measurements (Figure 2-2). The peak temperature of this process (142 °C) is coincident with the reported melting point (141 – 144 °C).²⁾ Thus, these endothermic processes correspond to the melting of the crystals. Therefore, the proton conductivity measurements of **1** were operated below 116 °C.

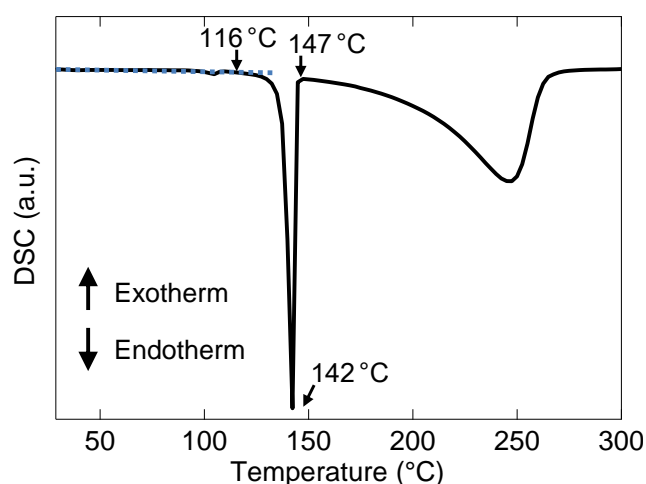


Figure 2-2. The DSC curve of the single crystals of **1** in the heating process.

2.3.2. Single crystal proton conductivity of imidazolium hydrogen succinate

Figure 2-3 shows the relationship between the crystal shape and crystallographic axes determined by X-ray diffraction measurements, where the [1 0 0] and [1 4 -9] directions are within the 2D network [Figure 2-1(a)] and the [0 1 1] is perpendicular to the 2D network [Figure 2-1(c)]. To investigate the effects of the H-bond interactions and molecular arrangements on the proton conduction, the single-crystal proton conductivity measurements were performed in these three directions. Figure 2-4 shows the results of single-crystal impedance measurements of **1** in the [1 0 0] direction at several temperatures. The Cole–Cole plots [Figure 2-4(a)] showed almost perfect semicircle profiles at each temperature, meaning that a single Debye-type

relaxation occurs in the single-crystal measurements. In contrast, distorted semicircles were observed in the measurements of pellet samples in the literature³⁾ and also in this research [Figure 2-4(b)]. The results indicate that the obtained conductivity is the intrinsic proton conductivity without contributions from the grain boundaries. The semicircles contract with increasing temperature [Figure 2-4(a)], which corresponds to increase of the proton conductivity.

The ac conductivity σ_{ac} was estimated from the obtained ac impedances (see Section 2.2 for the detail). Figure 2-4(c) shows the frequency dependence of σ_{ac} at each temperature. In the low frequency region (below 10 Hz), the values of σ_{ac} above 103 °C showed frequency-independent behavior, at which the value of σ_{ac} corresponds to the dc conductivity. Therefore, the author defined the σ_{ac} at 1 Hz as the proton conductivity σ of **1**.

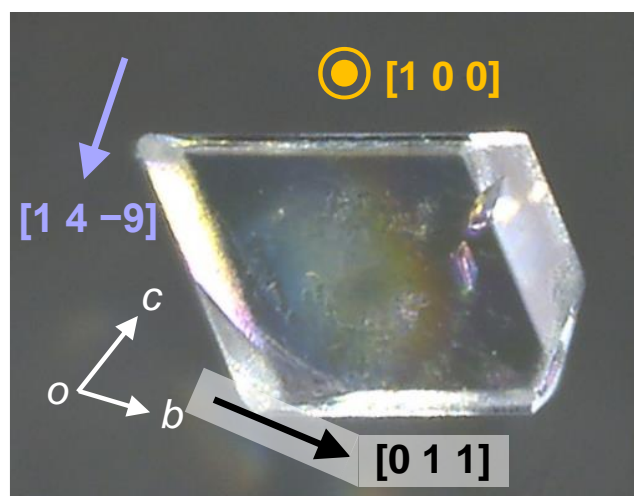


Figure 2-3. A photograph of a single crystal of **1** showing the relationship between the crystal shape and crystallographic axes. $[1\ 0\ 0]$, $[1\ 4\ -9]$, and $[0\ 1\ 1]$ directions indicated in the photograph are adopted in the proton conductivity measurements.

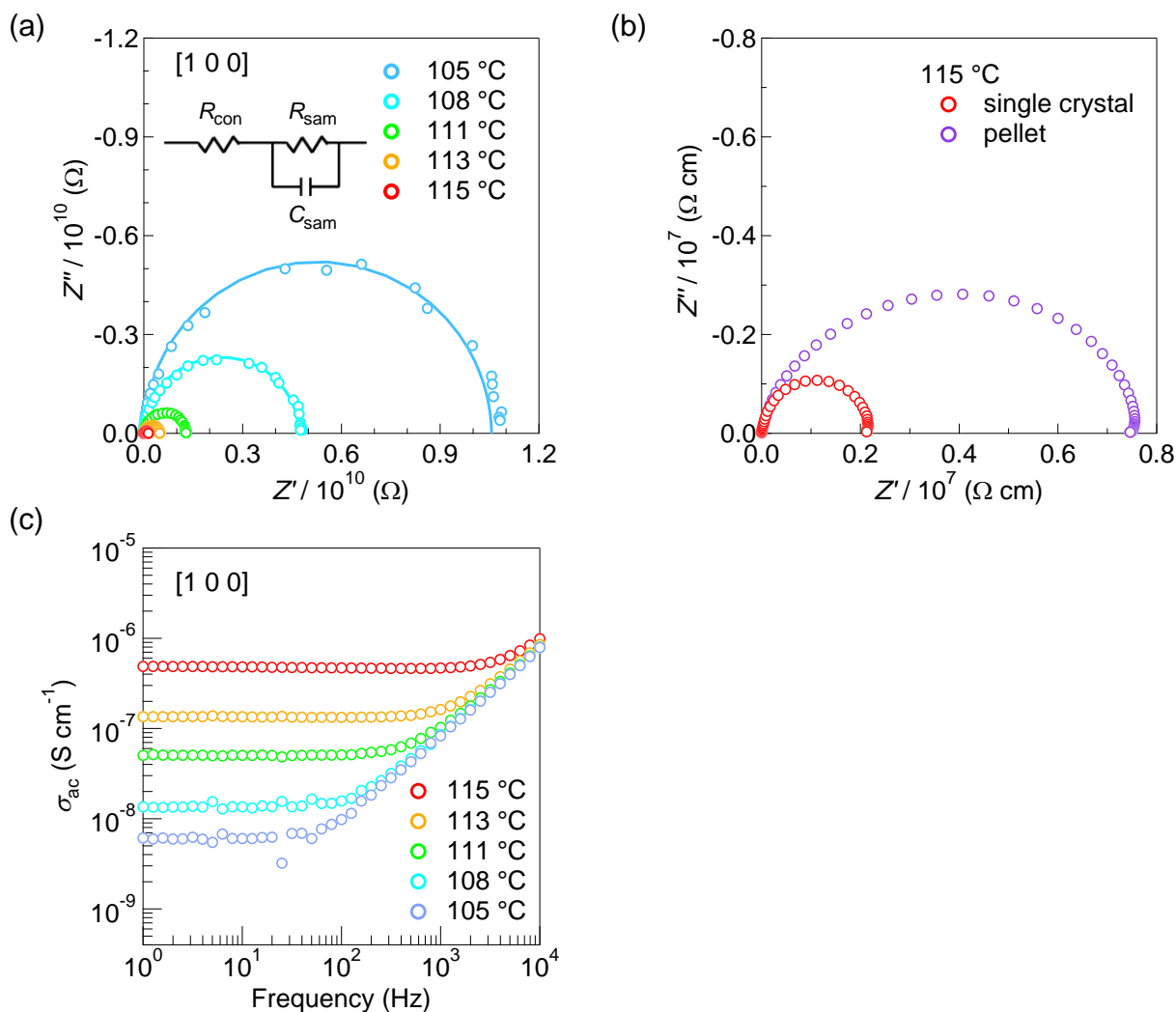


Figure 2-4. Results of the ac impedance measurements of **1**: Cole-Cole plots measured for (a) a single crystal of **1** along the $[1\ 0\ 0]$ direction at several temperatures below 116 °C at which the melting starts, and for (b) the single crystal and a pellet at 115 °C. (c) Frequency dependence of σ_{ac} measured for the single crystal of **1** along the $[1\ 0\ 0]$ direction at several temperatures below 116 °C. Open circles represent the experimental data, and solid curves represent the fitting curves obtained by using the equivalent circuit model shown in the inset of (a).

Almost perfect semicircles were also observed in the measurements along the $[1\ 4\ -9]$ and $[0\ 1\ 1]$ directions (Figure 2-5), which proves that the intrinsic proton conductivity was successfully obtained in all the three directions of the single crystal of **1**.

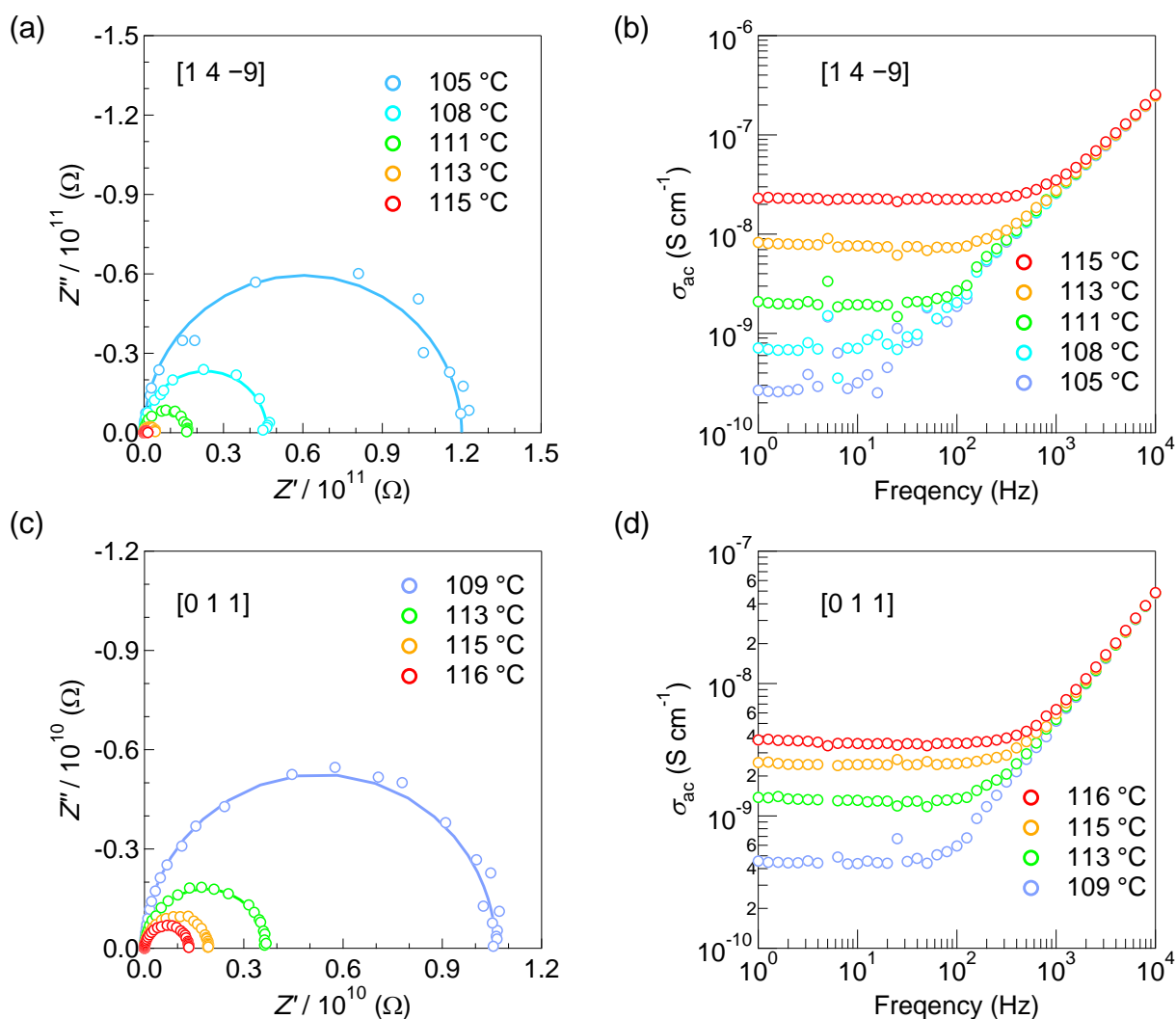


Figure 2-5. Results of the ac impedance measurements of **1**: (a, c) Cole-Cole plots measured for the single crystal of **1** along (a) the [1 4 -9] and (c) [0 1 1] directions at several temperatures below 116 °C at which the melting starts. (b, d) Frequency dependence of σ_{ac} measured for the single crystal of **1** along the (b) the [1 4 -9] and (d) [0 1 1] directions at several temperatures below 116 °C. Open circles represent the experimental data, and solid curves represent the fitting curves obtained by using the $R_{con}R_{sam}C_{sam}$ equivalent circuit model shown in the inset of Figure 2-4(a).

The σ values of the single crystal (*e.g.*, $4.7 \times 10^{-7} S cm^{-1}$ in the [1 0 0] direction at 115 °C) were lower than that of the pellet sample reported in the literature ($\sim 10^{-4} S cm^{-1}$ at ~ 115 °C).³⁾ On the other hand, the pellet prepared by crushing single crystals grown in this research showed

lower σ ($1.3 \times 10^{-7} \text{ S cm}^{-1}$ at 115°C) than the single crystal; as shown in Figure 2-4(b) (the impedance of the pellet at 1 Hz $7.5 \times 10^6 \Omega \text{ cm}$ is larger than that of the single crystal $2.1 \times 10^6 \Omega \text{ cm}$). The uncertain σ values of pellet samples inevitably include grain boundary effects, while single crystals do not include the effects. The grain boundaries have disordered structures composed of not only the constituent molecules (imidazole and succinic acid) but also interfused atmospheric molecules (*e.g.*, water molecules) which make proton conductivity non-intrinsic and uncertain.^{4c,h)} On the other hand, the σ of the single crystal is considered to include little of the extrinsic effects of atmospheric water molecules judging from the preparation condition using the solution of dehydrated solvent (see Section 2.2) and the high quality of the crystal supported by the X-ray structural analysis ($R_1 = 0.04$). These results indicate that the intrinsic proton conductivity of **1** was successfully determined for the first time.

2.3.3. Anisotropy of proton conductivity between directions parallel and perpendicular to the hydrogen-bond networks in imidazolium hydrogen succinate

Figure 2-6 shows the comparison among the σ values within the three directions parallel and perpendicular to the H-bond network in the single crystal (see also Table 2-2). As summarized in Table 2-2, at around 115°C , the two directions parallel to the H-bond network ($\sigma_{[1\ 0\ 0]} = 4.94 \times 10^{-7} \text{ S cm}^{-1}$ and $\sigma_{[1\ 4\ -9]} = 1.27 \times 10^{-7} \text{ S cm}^{-1}$) provide almost 2 orders higher conductivity than that perpendicular to the H-bond network ($\sigma_{[0\ 1\ 1]} = 3.55 \times 10^{-9} \text{ S cm}^{-1}$). This large difference is maintained in the present temperature range ($103 - 115^\circ\text{C}$), indicating that the proton conduction occurs more readily in the H-bond network than in its perpendicular direction. Note that $\sigma_{[0\ 1\ 1]}$ below 108°C was not estimated because of the large noise resulting from the large impedance.

Although these σ values are low compared to that of hydrous materials, such as Nafion[®] and some kinds of metal–organic frameworks (MOFs) ($\geq 10^{-2} \text{ S cm}^{-1}$),^{6,7)} the present σ values (up to $5 \times 10^{-7} \text{ S cm}^{-1}$) are ranked as a top-class σ in anhydrous organic single crystals.⁸⁾ In addition,

interestingly, this high σ was realized by its rapid increase (2 orders of magnitude) above 108 °C (orange and blue circles in Figure 2-6). Although the σ values of this material at further high temperatures were not evaluated because of the start of melting, the results suggest that further high σ , comparable to that of Nafion[®] and MOFs ($\sim 10^{-3}$ S cm⁻¹), can be obtained in these anhydrous organic materials by enhancing the thermal stability of the material.

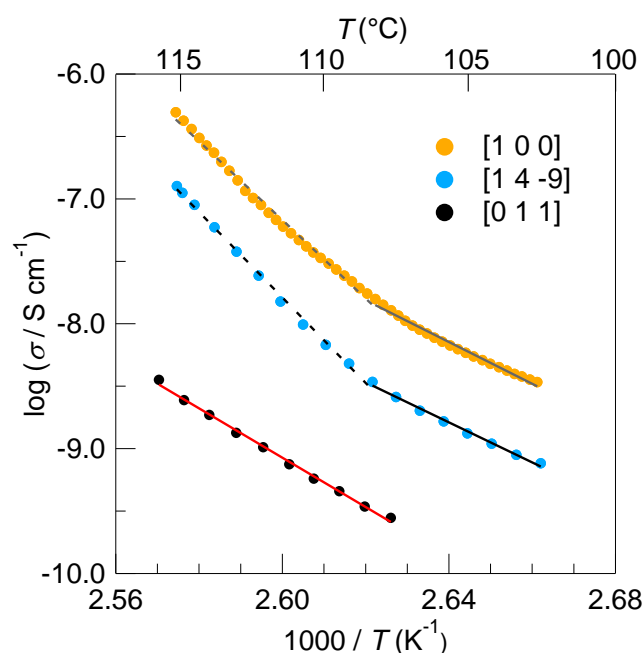


Figure 2-6. Arrhenius plots of the proton conductivity (σ) for the single crystal of **1** measured along the $[1\ 0\ 0]$ (orange circles), $[1\ 4\ -9]$ (blue circles), and $[0\ 1\ 1]$ (black circles) directions. The fitting lines for the $\sigma_{[1\ 0\ 0]}$, $\sigma_{[1\ 4\ -9]}$, and $\sigma_{[0\ 1\ 1]}$ are denoted in gray (solid line: 103 – 108 °C, dashed line: 108 – 115 °C), black (solid line: 102 – 108 °C, dashed line: 108 – 115 °C), and red (108 – 116 °C), respectively.

Table 2-2. Proton conductivities (σ) and activation energies (E_a) of the single crystal of **1** measured along the [1 0 0], [1 4 -9], and [0 1 1] directions.

Direction	Proton conductivity σ (S cm ⁻¹)	Activation energy E_a (eV)
[1 0 0] (parallel to H-bond network)	4.94×10^{-7} [115 °C]	3.32 [103 – 108 °C], 6.24 [108 – 115 °C]
[1 4 -9] (parallel to H-bond network)	1.27×10^{-7} [115 °C]	3.18 [102 – 108 °C], 6.79 [108 – 115 °C]
[0 1 1] (perpendicular to H-bond network)	3.55×10^{-9} [116 °C]	3.92 [108 – 116 °C]

The activation energies E_a within each direction were estimated by following Arrhenius equation

$$\sigma(T) = \sigma_0 \exp\left(-\frac{E_a}{kT}\right) \quad (2-1)$$

where σ is the proton conductivity, σ_0 is the pre-exponential factor, k is the Boltzmann constant, and T is the temperature. The estimated E_a values were summarized in Table 2-2. Although these values of E_a [e.g., 3.32 eV(103 – 108 °C) in the [1 0 0] direction] are quite high compared to that of hydrous systems such as Nafion[®] (0.11 eV),^{4d)} imidazole-based salts (1.6 – 2.5 eV)⁹⁾ and imidazole single crystal (1.9 eV)^{8a)} show similarly high E_a . Therefore, imidazolium cations are considered to play an important role for the anhydrous proton conductivity in **1**. On the other hand, while the E_a for the pellets of **1** reported in the literature (0.65 eV)³⁾ is close to those of the hydrous systems, the pellet prepared in this research showed the different E_a value (1.55 eV). This mismatch is, again, considered to reflect the extrinsic contribution in grain boundaries.

Here, σ in the former two directions parallel to the H-bond network were fitted with two lines (solid and dashed ones), because of their nonlinearity in the Arrhenius plots. On the other hand, the σ in the perpendicular direction ([0 1 1]) has a linear temperature dependence, fitted with a

single line. This behavior is also shown in Arrhenius plots of σT (Figure 2-7). These non-Arrhenius-type behaviors accompanying with the temperature dependent E_a are peculiar in the anhydrous proton conducting solids.

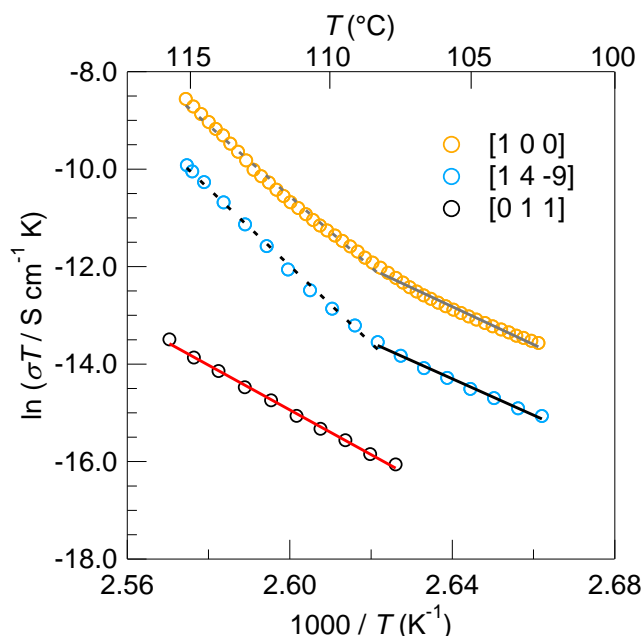


Figure 2-7. Arrhenius plots of $\ln(\sigma T)$ for the single crystal of **1** in the [1 0 0] (orange circles), [1 4 -9] (blue circles), and [0 1 1] (black circles) directions. The fitting lines for the [1 0 0], [1 4 -9], and [0 1 1] directions are denoted in gray (solid line: 103 – 108 °C, dashed line: 108 – 115 °C), black (solid line: 102 – 108 °C, dashed line: 108 – 115 °C), and red (108 – 116 °C), respectively.

About the proton conduction perpendicular to the H-bond networks, **1** has no H-bonds in this direction [see Figure 2-1(c)]; however, the single-crystal measurements reveal the proton conductivity of $3.55 \times 10^{-9} \text{ S cm}^{-1}$ at 116 °C (see Table 2-2). Interestingly, these values are comparable to that of imidazole single crystal measured along the H-bond chain ($\sigma = 10^{-9} \text{ S cm}^{-1}$ at 80 °C), where the 180°-flip motion of imidazole molecules are known to realize its proton conductivity.^{8a,10)} The crystal structure of **1** have the carboxy groups of succinate anions

above and below imidazolium cations [Figure 2-8(a)]. In addition, the imidazolium cations in **1** are expected to show a 180°-flip motion [Figure 2-8(b)] observed by the solid-state NMR study.¹¹⁾ Therefore, through this dynamic motion, the imidazole molecules is considered to relay protons from succinic acids in the upper plane to succinate anions in the lower plane [Figure 2-8(c)], leading to the observed proton conductivity.

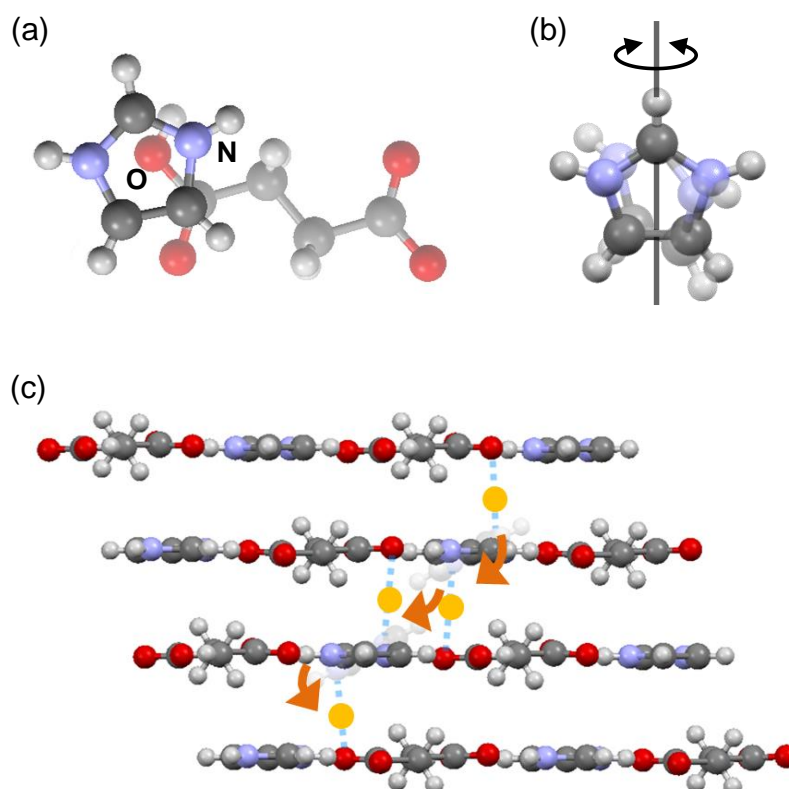


Figure 2-8. (a) Projection of an imidazolium cation overlapping a succinate anion in the neighboring 2D H-bond networks,²⁾ (b) 180°-flip motion around the pseudo two-fold axis of imidazolium cation,¹¹⁾ and (c) schematic image of a plausible proton conduction perpendicular to the H-bond networks of **1**. In (c), yellow circles represent protons, and blue dashed lines are drawn between the nitrogen atoms of imidazolium cations and the overlapped oxygen atoms of succinate anions.

2.3.4. Anisotropy of proton conductivity in the hydrogen-bond network of imidazolium hydrogen succinate

The anisotropy between directions parallel and perpendicular to the H-bond network demonstrated the importance of the network structure in the anhydrous proton conduction in **1**, as discussed in the previous section. In addition to the anisotropy between parallel and perpendicular directions to the H-bond network, the σ in the two directions parallel to the network ($\sigma_{[1\ 0\ 0]}$ and $\sigma_{[1\ 4\ -9]}$) also showed anisotropy. At 115 °C, the $[1\ 0\ 0]$ direction has about 4 times higher σ ($4.94 \times 10^{-7}\ \text{S cm}^{-1}$) than the $[1\ 4\ -9]$ direction ($1.27 \times 10^{-7}\ \text{S cm}^{-1}$) (see Table 2-2 in Section 2.3.3), and this trend is unchanged in this temperature region (see Figure 2-6 in Section 2.3.3). In fact, the previous theoretical calculation³⁾ points out that the potential barrier against proton conduction along the $[1\ 0\ 0]$ direction is lower than that along the $[1\ 4\ -9]$ direction, which is consistent with the observed anisotropy of σ in the H-bond network.

In the $[1\ 0\ 0]$ direction with the higher proton conductivity, the imidazolium cation (Im) and the succinate anion (Suc) are alternately arranged ($\cdots\text{Im}\text{--}\text{Suc}\text{--}\text{Im}\text{--}\text{Suc}\cdots$), as represented by the orange belt in Figure 2-9(a). On the other hand, in the $[1\ 4\ -9]$ direction with the lower conductivity, two succinate anions exist between the imidazolium cations ($\cdots\text{Im}\text{--}\text{Suc}\text{--}\text{Suc}\text{--}\text{Im}\cdots$), as represented by the light blue belt in Figure 2-9(b). In addition, the $[1\ 0\ 0]$ direction only has H-bonds between the acid (Suc) and base (Im) molecules, “acid–base H-bonds” [red dashed lines in Figure 2-9(a)], whereas the $[1\ 4\ -9]$ direction has not only the acid–base H-bonds but also H-bonds between the acid molecules [“acid–acid H-bonds”; black dashed lines in Figure 2-9(b)]. The previous quantum dynamics simulation study by Hori *et al.* suggested the faster proton transfer rates in the acid–base H-bond than that in the acid–acid H-bond,¹²⁾ which is consistent with the observed anisotropy of σ in the H-bond network. Therefore, the acid–base H-bonds is important to realize higher proton conductivity in **1**, and the structural differences in the H-bond manners and molecular arrangements caused the anisotropy of the proton conductivity between the $[1\ 0\ 0]$ and $[1\ 4\ -9]$ directions within the H-bond network of

1.

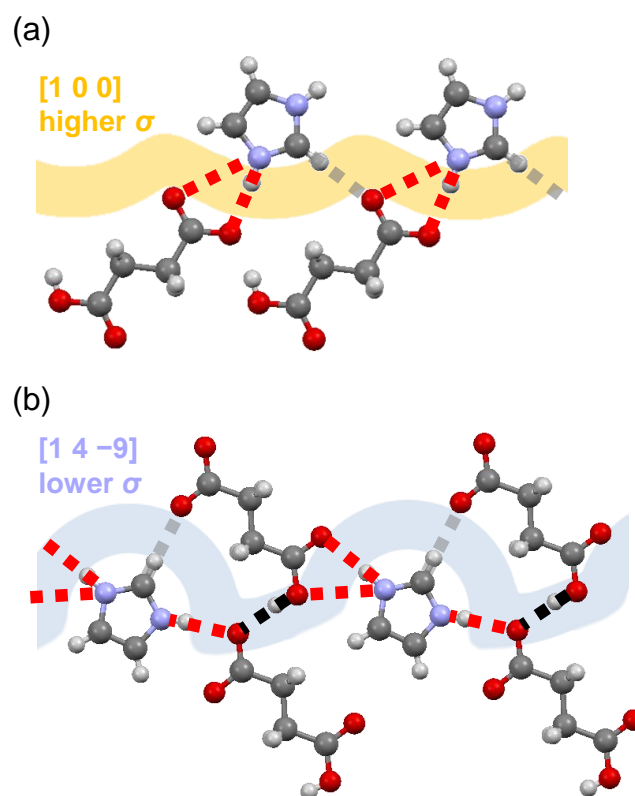


Figure 2-9. Molecular arrangements along (a) the $[1\ 0\ 0]$ and (b) the $[1\ 4\ -9]$ directions in the H-bond network of **1**. The orange and light blue belts schematically represent the possible proton conducting paths.

2.4. Conclusion

In this research, the author has revealed the intrinsic proton conductivity without grain boundary contributions in an acid–base type anhydrous organic crystal, imidazolium hydrogen succinate (**1**), which has a 2D H-bond network structure. The obtained conductivities are $1\text{--}5 \times 10^{-7} \text{ S cm}^{-1}$ within the network, which are much higher than that in the perpendicular direction to the network ($4 \times 10^{-9} \text{ S cm}^{-1}$). This result demonstrates that the H-bond network structure significantly promote proton conduction in this system. Furthermore, the anisotropy of proton conductivities along two directions within the 2D H-bond network indicates that this proton conduction is more significant in the H-bonds between the acid and base molecules than in

those between the acid molecules.

The single-crystal study for the anhydrous purely organic proton conductors revealed the detailed relationship of the proton conductivity with the molecular arrangements and H-bond manners for the first time. The novel findings about the effects of the “static” factors related to the crystal structure on the proton conductivity are essential for the elucidation of origins and mechanisms of anhydrous proton conduction in the purely organic crystals.

2.5. Reference

- 1) K. Pogorzelec-Glaser, J. Garbarczyk, Cz. Pawlaczyk, and E. Markiewicz, *Mater. Sci.-Pol.* **24**, 245 (2006).
- 2) J. C. MacDonald, P. C. Dorrestein, and M. M. Pilley, *Cryst. Growth Des.* **1**, 29 (2001).
- 3) K. Pogorzelec-Glaser, Cz. Pawlaczyk, A. Pietraszko, and E. Markiewicz, *J. Power Sources* **173**, 800 (2007).
- 4) (a) K. D. Kreuer, T. Dippel, Y. M. Baikov, and J. Maier, *Solid State Ionics* **86–88**, 613 (1996). (b) G. V. Lavrova, E. B. Burgina, A. A. Matvienko, and V. G. Ponomareva, *Solid State Ionics* **177**, 1117 (2006). (c) A. Düvel, M. Wilkening, R. Uecker, S. Wegner, V. Sepelak, and P. Heitjans, *Phys. Chem. Chem. Phys.* **12**, 11251 (2010). (d) M. Yoon, K. Suh, H. Kim, Y. Kim, N. Selvapalam, and K. Kim, *Angew. Chem. Int. Ed.*, **50**, 7870 (2011). (e) D. Umeyama, S. Horike, M. Inukai, T. Itakura, and S. Kitagawa, *J. Am. Chem. Soc.* **134**, 12780 (2012). (f) Song-Song Bao, K. Otsubo, J. M. Taylor, Z. Jiang, Li-Min Zheng, and H. Kitagawa, *J. Am. Chem. Soc.* **136**, 9292 (2014). (g) Q. Tang, Y. Liu, S. Liu, D. He, J. Miao, X. Wang, G. Yang, Z. Shi, and Z. Zheng, *J. Am. Chem. Soc.* **136**, 12444 (2014). (h) S. Tominaka and A. K. Cheetham, *RSC Adv.* **4**, 54382 (2014). (i) Song-Song Bao, Nan-Zhu Li, J. M. Taylor, Y. Shen, H. Kitagawa, and Li-Min Zheng, *Chem. Mater.* **27**, 8116 (2015). (j) R. Li, Shuai-Hua Wang, Xu-Xing Chen, J. Lu, Zhi-Hua Fu, Y. Li, G. Xu, Fa-Kun Zheng, and Guo-Cong Guo, *Chem. Mater.* **29**, 2321 (2017). (k) B. Joarder, Jian-Bin Lin, Z. Romero, and G. K. H. Shimizu, *J. Am. Chem. Soc.* **139**, 7 (2017). (l) M. Wang, Hong-Bin Luo, J. Zhang, Shao-Xian Liu, C. Xue, Y. Zou, and Xiao-Ming Ren, *Dalton Trans.* **46**, 7904 (2017). (m) X. Chen, Y. Zhang, P. Ribeiorinha, H. Li, X. Kong, and M. Boaventura, *RSC Adv.* **8**, 5225 (2018).
- 5) A. Bondi, *J. Phys. Chem.* **68**, 441 (1964).
- 6) (a) P. C. Rieke and N. E. Vanderborgh, *J. Membr. Sci.* **32**, 313 (1987). (b) Y. Sone, P. Ekdunge, and D. Simonsson, *J. Electrochem. Soc.* **143**, 1254 (1996). (c) S. Slade, S. A.

- Campbell, T. R. Ralph, and F. C. Walsh, *J. Electrochem. Soc.* **149**, A1556 (2002). (d) P. Dimitrova, K. A. Friedrich, U. Stimming, and B. Vogt, *Solid State Ionics* **150**, 115 (2002).
- 7) (a) M. Sadakiyo, T. Yamada, and H. Kitagawa, *J. Am. Chem. Soc.* **131**, 9906 (2009). (b) N. C. Jeong, B. Samanta, C. Y. Lee, O. K. Farha, and J. T. Hupp, *J. Am. Chem. Soc.* **134**, 51 (2012). (c) J. M. Taylor, S. Dekura, R. Ikeda, and H. Kitagawa, *Chem. Mater.* **27**, 2286 (2015).
- 8) (a) A. Kawada, A. R. McGhie, and M. M. Labes, *J. Chem. Phys.* **52**, 3121 (1970). (b) N. Yutronic, J. Merchan, P. Jara, V. Manriquez, O. Wittke, and G. Gonzalez, *Supramol. Chem.* **16**, 411 (2004). (c) D. Basak, C. Versek, D. T. Toscano, S. Christensen, M. T. Tuominen, and D. Venkataraman, *Chem. Commun.* **48**, 5922 (2012). (d) M. Pulst, J. Balko, Y. Golitsyn, D. Reichert, K. Busse, and J. Kressler, *Phys. Chem. Chem. Phys.* **18**, 6153 (2016).
- 9) (a) K. Pogorzelec-Glaser, A. Rachocki, P. Ławniczak, A. Pietraszko, Cz. Pawlaczyk, B. Hilczer, and M. Pugaczowa-Michalska, *CrystEngComm* **15**, 1950 (2013). (b) A. Rachocki, K. Pogorzelec-Glaser, P. Ławniczak, M. Pugaczowa-Michalska, A. Łapiński, B. Hilczer, M. Matczak, and A. Pietraszko, *Cryst. Growth Des.* **14**, 1211 (2014).
- 10) J. T. Daycock, G. P. Jones, J. R. N. Evans, and J. M. Thomas, *Nature* **218**, 672 (1968).
- 11) T. Umiyama, R. Ohashi, T. Ida, and M. Mizuno, *Chem. Lett.* **42**, 1323 (2013).
- 12) Y. Hori, T. Ida, and M. Mizuno, *Phys. Chem. Chem. Phys.* **19**, 16857 (2017).

Chapter 3.

Effects of Proton Donating Abilities (pK_a) of Constituent Molecules as “Static” Factor of Anhydrous Proton Conductivity

3.1. Introduction

As introduced in Chapter 1, the proton conductivities of a series of imidazolium hydrogen dicarboxylates have been investigated in the form of pellets, for some of which the crystal structures have also been reported.¹⁻³⁾ Among these salts, the chain structures of the dicarboxylates are different, which changes chemical property of the dicarboxylates, that is, the proton donating ability (pK_a), and thus will affect their anhydrous proton conductivities. For example, an analogue salt of **1**, imidazolium hydrogen glutarate (**2**)¹⁾ [see Figure 1-7(d) in Section 1.5] has just by one methylene group longer acid molecule than **1** [see Figure 1-7(b) in Section 1.5]. On the other hand, in imidazolium hydrogen fumarate (**3**)²⁾ [see Figure 1-7(c) in Section 1.5], acid molecule has almost the same structure but a C=C double bond compared with that in **1**. Both **2** and **3** have 2D H-bond networks like **1** (see Figure 3-3 and 3-4 in Section 3.3).^{1,2)} Therefore, comparison of the proton conductivities among the salts **1**, **2**, and **3** will provide a critical insight into the pK_a effect on the anhydrous proton conductivity of these systems. For **2**, the proton conductivity in the pellet sample was reported in the literature,¹⁾ and its value ($\sigma \sim 10^{-7} \text{ S cm}^{-1}$ at 17 °C) is close to that of **1**,³⁾ that is, relatively high among the imidazolium hydrogen dicarboxylates. However, as discussed in Section 2.3.2, the proton conductivity in the form of pellets is considered to include the extrinsic effects of grain boundaries and/or atmospheric water molecules, and that of single crystals of **2** has not been

investigated yet. On the other hand, conductivity σ of **3** has not been investigated in the form of neither pellets nor single crystals. Therefore, their intrinsic conductivity without grain boundary contributions and its relationship with crystal structures are still unclear.

In this research, in order to reveal the intrinsic proton conductivity of **2** and **3** and the effects of pK_a , the author investigated the proton conductivities and their anisotropy between the directions parallel and perpendicular to the 2D H-bond networks using high-quality single crystals of **2** and **3**, and compared the obtained proton conductivities among the salts **1**, **2**, and **3**.

3.2. Experiments

Preparation of single crystals

Single crystals of **2** and **3** were prepared (see Figure 3-1 and 3-2 in Section 3.3.1) by the following method based on that of **1** (see Section 2.2). All chemicals were commercially available and used as received. **2**: Imidazole [681 mg, 10 mmol, Wako Pure Chemical Industries (purity > 98%)] and glutaric acid [1321 mg, 10 mmol, Tokyo Chemical Industry (purity > 99%)] were suspended in a mixed solvent of dehydrated methanol [10 mL, Wako Pure Chemical Industries (purity > 99.8%)] and dehydrated acetonitrile [10 mL, Wako Pure Chemical Industries (purity > 99.8%)]. This suspension was stirred at 40 °C until all the materials were dissolved (about 10 min). The resultant solution was slowly evaporated for 3 days at room temperature, and then the precipitates were collected by filtration and washed with dehydrated ethyl acetate, to give the desired material as colorless crystals. **3**: Imidazole [340 mg, 5 mmol, Wako Pure Chemical Industries (purity > 98%)] and fumaric acid [580 mg, 5 mmol, Wako Pure Chemical Industries (purity > 98%)] were suspended in dehydrated methanol [40 mL, Wako Pure Chemical Industries (purity > 99.8%)]. This suspension was stirred at 40 °C until all the materials were dissolved (about 10 min). The resultant solution was slowly evaporated for 6 days at room temperature, and then the precipitates were collected by filtration and washed with

dehydrated ethyl acetate, to give the desired material as colorless crystals.

Single-crystal X-ray structure analyses

The crystal structures of **2** and **3** were identified by single-crystal X-ray diffraction (see Table 3-1 and 3-2 in Section 3.3.1).^{1,2)} Methods for identification of the crystal structures and determination of crystallographic orientations of the single crystals are same with the method for **1** described in Section 2.2.

Thermal analyses

Thermal stability of the crystals for **2** and **3** [see Figure 3-5(a) and (b) in Section 3.3.1] was evaluated by the same method using the same equipment with that for **1** (see Section 2.2). The single crystals [7.2 mg (**2**) or 4.0 mg (**3**)] were encapsulated in an Al pan and heated from 20 to 300 °C with a rate of 5 °C min⁻¹ with nitrogen gas flow.

Melting-point determinations

Melting points of **2** and **3** were determined by using an MPA-100 Automated Melting Point System (Stanford Research Systems, Inc.) and are uncorrected. The single crystal was loaded into a glass capillary. The capillary was inserted into a heating slot of the instrument and heated from room temperature to 140 °C with a rate of 2 °C min⁻¹ for **2**, and to 200 °C with 1 °C min⁻¹ for **3**.

Alternating-current impedance spectroscopy

Method and equipment of ac impedance spectroscopy measurements are same with those for **1** (see Section 2.2). As-grown single crystals of **2** and **3** were cut into blocks [typical size of 0.2 × 1.4 × 1.7 mm³ (**2**) and 1.2 × 1.2 × 0.8 mm³ (**3**)] to expose the desired faces for the anisotropic measurements. The complex impedance of the samples was measured from 1 Hz to 1 MHz in

the temperature range of room temperature – 95 °C for **2**, and room temperature – 133 °C for **3**. Temperature was controlled by using a home-built high-temperature oven.

The fitting for the obtained Cole–Cole plots was operated by using the equivalent circuit consisting of one series resistance R_{con} and one parallel combination of a single resistance R_{sam} and capacitance C_{sam} [see insets of Figure 3-6(a) and 3-8(a) in Section 3.3.1]. The σ_{ac} values were estimated from $\sigma_{\text{ac}} = |Z(\omega)|^{-1} (l / S)$, where $Z(\omega)$ is the complex impedance at frequency ω of the applied electric field, l and S are thickness and area of samples. The values of proton conductivity σ are defined from σ_{ac} at 1 Hz in the temperature region of 59 to 94 °C (**2**) or 104 to 133 °C (**2**), because frequency-independent σ_{ac} corresponding to the dc conductivity in the low frequency region below 10 Hz was observed above 59 °C (**2**) or 105 °C (**3**) [see Figure 3-6(b), (d) and 3-8(b), (d) in Section 3.3.1].

3.3. Results and discussion

3.3.1. Crystal structures and anisotropy of the proton conductivities of imidazolium hydrogen glutarate and fumarate

Large, high-quality single crystals of **2** and **3** were successfully grown with a typical size of $1.3 \times 1.4 \times 2.1 \text{ mm}^3$ (**2**) and $1.0 \times 1.1 \times 2.9 \text{ mm}^3$ (**3**) (Figure 3-1 and 3-2) based on the method for the salt **1**, which the author has already established (see Section 3.2). The crystal structures of the prepared single crystals of **2** and **3** were identified to the reported one in the literatures,^{1,2)} as shown in Table 3-1 and 3-2.

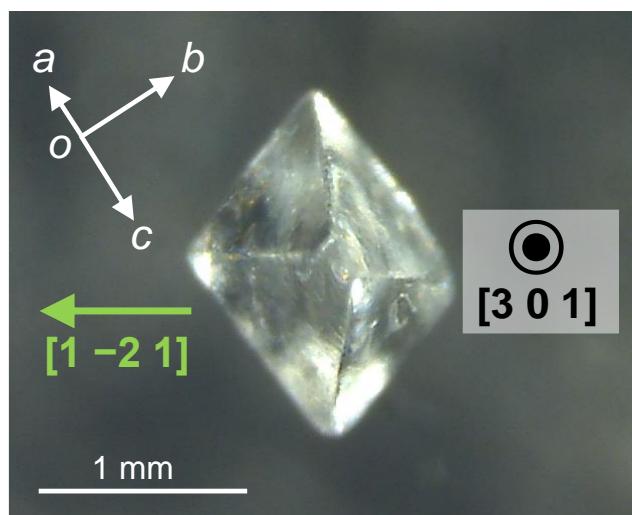


Figure 3-1. A photograph of a single crystal of **2** showing the relationship between the crystal shape and crystallographic axes. $[-1\ 2\ 1]$ and $[3\ 0\ 1]$ directions indicated in the photograph are adopted in the proton conductivity measurements.

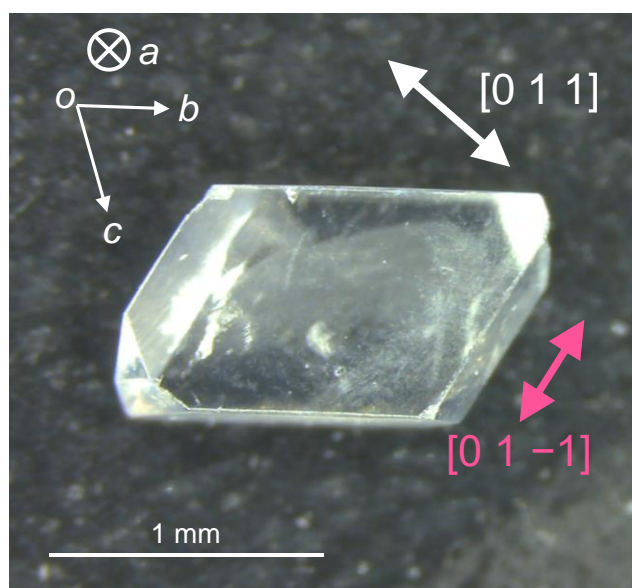


Figure 3-2. A photograph of a single crystal of **3** showing the relationship between the crystal shape and crystallographic axes. $[0\ 1\ -1]$ and $[0\ 1\ 1]$ directions indicated in the photograph are adopted in the proton conductivity measurements.

Table 3-1. Crystallographic data of **2**.

Sample	reported¹⁾	this research
Temperature (°C)	20	25
Crystal system	triclinic	triclinic
Space group	<i>P</i> −1	<i>P</i> −1
<i>a</i> (Å)	8.420(2)	8.4059(3)
<i>b</i> (Å)	13.685(3)	13.6438(5)
<i>c</i> (Å)	17.068(3)	17.0122(7)
α (°)	90.62(3)	90.413(3)
β (°)	103.45(3)	103.504(3)
γ (°)	91.03(3)	91.045(3)
Volume (Å ³)	1912.23	1896.71(13)
<i>Z</i>	8	8
<i>D</i> _{calc} (g cm ^{−3})	1.391	1.402
λ (Å)	0.71073	0.71073
<i>R</i> _{int}	—	0.0196
<i>R</i> ₁ (<i>I</i> > 2.00σ(<i>I</i>))	0.0668	0.0450
<i>wR</i> ₂ (all reflections)	—	0.1299
GOF	1.052	1.037
CCDC number	225442	—

Table 3-2. Crystallographic data of **3**.

Sample	reported ²⁾	this research
Temperature (°C)	24	20
Crystal system	triclinic	triclinic
Space group	<i>P</i> –1	<i>P</i> –1
<i>a</i> (Å)	7.478(2)	7.4791(18)
<i>b</i> (Å)	7.747(2)	7.7555(18)
<i>c</i> (Å)	8.416(2)	8.424(2)
α (°)	69.69(2)	69.702(10)
β (°)	81.42(2)	81.416(12)
γ (°)	66.18(2)	66.178(11)
Volume (Å ³)	418.272	419.22(19)
<i>Z</i>	2	2
<i>D</i> _{calc} (g cm ^{–3})	1.462	1.459
λ (Å)	0.71069	0.71073
<i>R</i> _{int}	0.0172	0.0145
<i>R</i> ₁ (<i>I</i> > 2.00σ(<i>I</i>))	0.0420	0.0384
<i>wR</i> ₂ (all reflections)	0.1213	0.1136
GOF	1.048	1.069
CCDC number	1211264	—

Figure 3-3 shows the crystal structure of **2**.¹⁾ Although **2** has a similar 2D H-bond network structure like **1**, the 2D H-bond network of **2** is formed by crystallographically independent four imidazolium (Im) and four glutarate (Glu) ions unlike that in **1**, which is formed by crystallographically independent one Im and one succinate ions. The H-bond manners around all the four Im cations in **2** are very similar to each other, as shown in Figure 3-3(a) and (b). One N–H moiety of the Im cations [light orange areas in Figure 3-3(b)] forms a H-bond connected to the carboxyl group of the Glu anions (brown dashed lines) in a bifurcated manner with a short contact with the adjacent oxygen atom (blue dashed lines), similar to the case of **1**. The other N–H moiety [light green areas in Figure 3-3(b)] forms a linear type H-bond with the other carboxyl group (red dashed lines). A C–H···O short contact (gray dashed lines) and an

O–H \cdots O H-bond (green dashed lines) are also found in **2** as observed in **1**. On the other hand, there are no effective H-bonds between the 2D networks [Figure 3-3(c)]. The atomic distances along the H-bonds and short contacts in the network and the shortest N \cdots O distances between the neighboring networks are summarized in Table 3-3. Like **1** (see Figure 2-9 in Section 2.3.4), possible conduction path in the H-bond network of **2** [the green belt in Figure 3-3(d)] is expected to include acid–base H-bonds (red lines) like **1**.

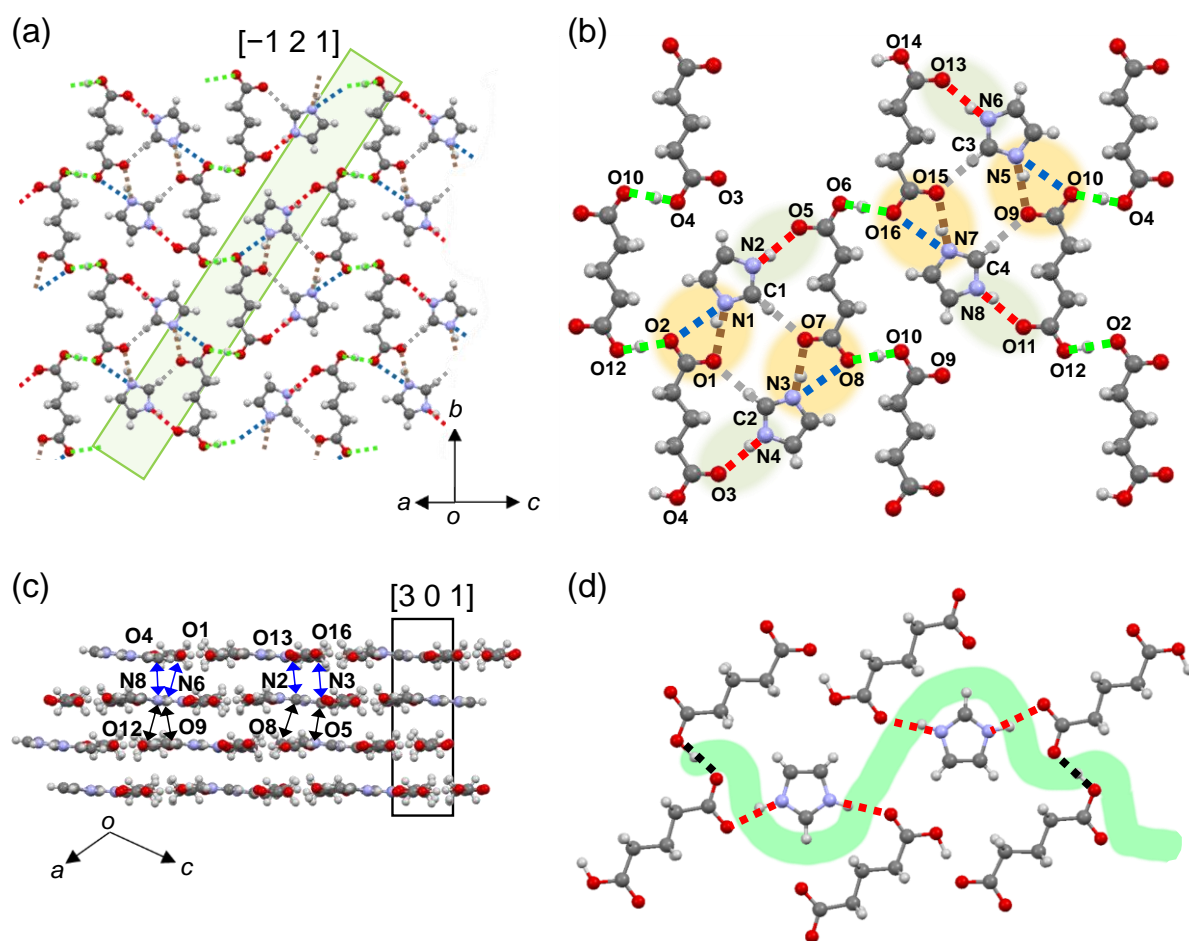


Figure 3-3. Crystal structure of **2**.¹⁾ (a) 2D H-bond network structure (red and brown dashed lines: N–H···O H-bonds, blue dashed lines: N···O short contacts, green dashed lines: O–H···O H-bonds, gray dashed lines: C–H···O contacts), (b) H-bond manners in the 2D H-bond network, and (c) stacking arrangement of the networks. (d) A possible proton conducting path in the 2D H-bond network of **2** (red dashed lines: acid–base H-bonds, black dashed lines: acid–acid H-bonds). Black and blue arrows in (c) represent shortest N···O distances from a network to one and to the other neighboring networks, respectively. Proton conductivity measurements of **2** were carried out in the $[-1\ 2\ 1]$ and $[3\ 0\ 1]$ directions as shown in (a) and (c). The green belt in (d) schematically represents the possible path of the proton conduction.

Table 3-3. Atomic distances between nitrogen and oxygen (d_{NO}), between oxygens (d_{OO}), and between carbon and oxygen atoms (d_{CO}) along N–H \cdots O, O–H \cdots O H-bonds, and C–H \cdots O contacts in the network, and N \cdots O distances between the neighboring networks.

	Distance (Å)			
d_{NO} [brown dashed lines in Figure 3-3(b)]	2.77 (N1 \cdots O1)	2.74 (N3 \cdots O7)	2.76 (N5 \cdots O9)	2.75 (N7 \cdots O15)
d_{NO} (Å) [blue dashed lines in Figure 3-3(b)]	3.10 (N1 \cdots O2)	3.11 (N3 \cdots O8)	3.13 (N5 \cdots O10)	3.14 (N7 \cdots O16)
d_{NO} (Å) [red dashed lines in Figure 3-3(b)]	2.80 (N2 \cdots O5)	2.83 (N4 \cdots O3)	2.78 (N6 \cdots O13)	2.82 (N8 \cdots O11)
d_{CO} (Å) [grey dashed lines in Figure 3-3(b)]	3.24 (C1 \cdots O7)	3.20 (C2 \cdots O1)	3.21 (C3 \cdots O15)	3.19 (C4 \cdots O9)
d_{OO} (Å) [green dashed lines in Figure 3-3(b)]	2.49 (O2 \cdots O12)	2.48 (O4 \cdots O10)	2.49 (O6 \cdots O16)	2.48 (O8 \cdots O10)
d_{NO} (Å) [blue arrows in Figure 3-3(c)]	3.44 (N2 \cdots O13)	3.47 (N3 \cdots O16)	3.49 (N6 \cdots O1)	3.45 (N8 \cdots O4)
d_{NO} (Å) [black arrows in Figure 3-3(c)]	3.54 (N2 \cdots O8)	3.39 (N3 \cdots O5)	3.39 (N6 \cdots O9)	3.42 (N8 \cdots O12)

As shown in Figure 3-4(a), **3** has also similar 2D H-bond network structure²⁾ to **1** and **2** (see Figure 2-1 in Section 2.3.1 and Figure 3-3). In this network, two N–H moieties of an Im cation are connected to carboxyl groups of fumarate (Fum) anions with N–H···O H-bonds ($d_{\text{NO}} = 2.66$ and 2.79 Å). The oxygen atom of Fum anion formed O–H···O H-bonds ($d_{\text{OO}} = 2.57$ Å) with a neighboring Fum anion. Unlike **1** and **2**, the five-membered rings of the Im cations are out of the H-bond networks (a dihedral angle between molecular plane of imidazolium cation and the H-bond network: 77°) [Figure 3-4(b)]. The relatively short C···O contact of 3.19 Å (blue and brown arrows) is formed between Im and Fum ions in neighboring networks. On the other hand, like **1** and **2** [see Figure 2-9 in Section 2.3.4, and Figure 3-3(d)], possible conduction path in the H-bond network of **3** [Figure 3-4(c)] is also expected to be within the 2D H-bond network and include acid–base H-bonds (red lines).

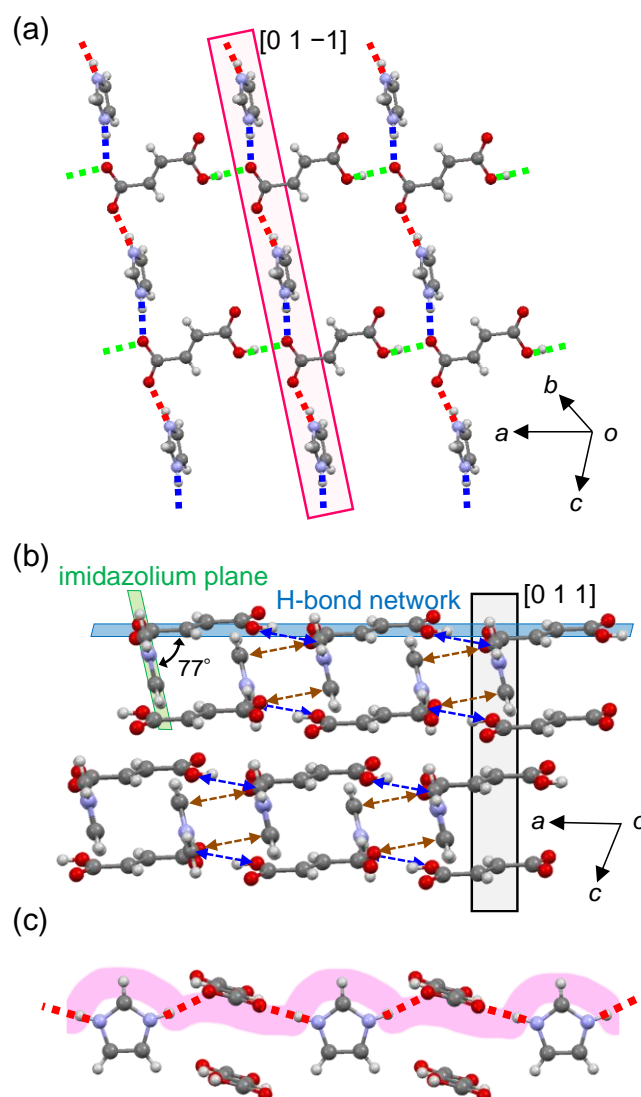


Figure 3-4. Crystal Structure of **3**.²⁾ (a) 2D H-bond network structure (red and blue dashed lines: N–H···O H-bonds, green dashed lines: O–H···O H-bonds) and (b) stacking arrangement of the 2D H-bond networks (blue and brown dashed arrows: C···O short contacts). (c) A possible proton conducting path in the 2D H-bond network of **3** (red dashed lines: acid–base H-bonds, black dashed lines: acid–acid H-bonds). Blue and green planes in (b) represent the planes parallel to the H-bond network and to the imidazolium five-membered ring, respectively. Proton conductivity measurements of **3** were carried out in the [0 1 -1] and [0 1 1] directions as shown in (a) and (b). The pink belt in (c) schematically represents the possible path.

Prior to the ac impedance measurements, thermal stabilities of the single crystals of **2** and **3** were investigated by DSC. The single crystals of **2** showed an endothermic process starting from 94 °C in the obtained DSC curve [Figure 3-5(a)]. The peak temperature of this process (122 °C) is coincident with the melting point (around 120 °C) confirmed by melting-point determinations. Above the melting point, an endothermic process with peak temperature of 292 °C appeared, which corresponds to decomposition of the compound. On the other hand, the single crystals of **3** showed an endothermic process starting from 133 °C and turned to an exothermic process from 160 °C [Figure 3-5(b)]. The peak temperature of this process is 176 °C. In this process, the colorless single crystals show solid-solid transition to non-crystalline opaque solids (confirmed by the melting-point determinations and the X-ray diffraction measurements). This reaction possibly corresponds to a chemical reaction or decomposition of the constituent molecules. After the reaction, an endothermic process with peak temperature of 235 °C appeared, corresponding to decomposition of the material. Therefore, the ac impedances of **2** and **3** were measured below 94 °C at which the melting starts (**2**) and below 133 °C at which the change to the non-crystalline state starts (**3**).

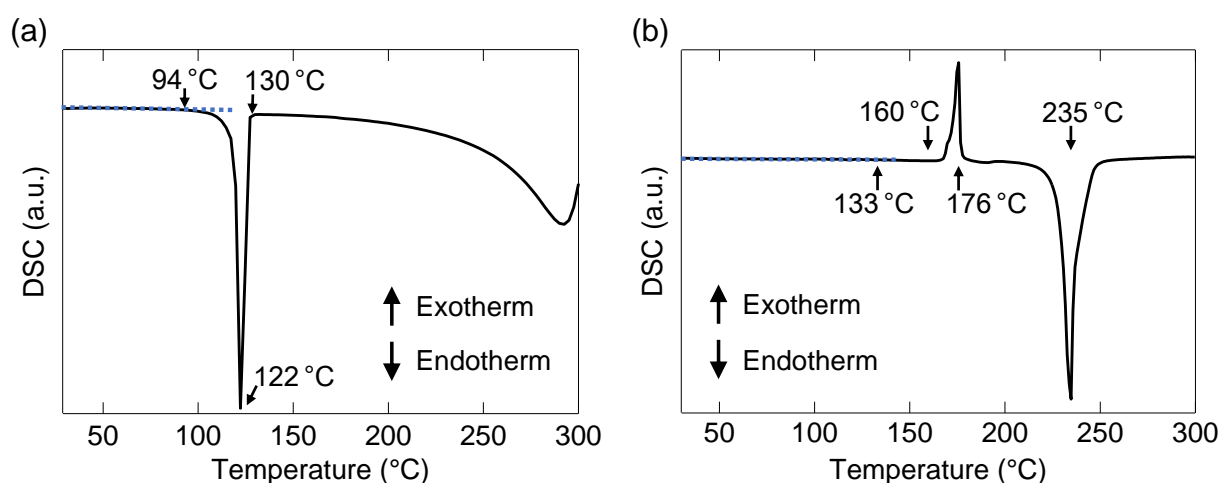


Figure 3-5. DSC curves for the single crystals of (a) **2** and (b) **3** in the heating process.

Based on the determined relationship between the crystal shape and crystallographic axes for **2** and **3** (see Figure 3-1 and 3-2), the single-crystal proton conductivity measurements were performed in the directions parallel and perpendicular to the 2D H-bond networks.

For **2**, proton conductivities were measured along the $[-1\ 2\ 1]$ direction, parallel to the H-bond network, and the $[3\ 0\ 1]$ direction, perpendicular to the network (Figure 3-3). The obtained Cole–Cole plots for a single crystal of **2** gave almost perfect semicircle profiles as shown in Figure 3-6(a) and (c), indicating that the single crystal of **2** provided the intrinsic proton conductivity originating from the bulk region of the crystal without contributions of grain boundaries. As shown in Figure 3-6(b) and (d), in the low frequency region below 10 Hz, the ac conductivity σ_{ac} above 59 °C showed frequency-independent value corresponding to the dc conductivity. Figure 3-7(a) shows Arrhenius plots of the proton conductivity σ (= the σ_{ac} at 1 Hz) for the $[-1\ 2\ 1]$ and $[3\ 0\ 1]$ directions, and Table 3-4 summarizes the results of the analysis (σ and E_a). The σ values of the single crystal (e.g., 2.59×10^{-9} S cm $^{-1}$ in the $[-1\ 2\ 1]$ direction at 59 °C) were lower than that of the pellet sample reported in the literature ($\sim 10^{-7}$ S cm $^{-1}$ at 17 °C),¹⁾ despite the higher temperature for the σ values of the single crystal than that of the pellet, which supports the indication that the σ values of single crystals reflect the intrinsic proton conductivity without contributions of grain boundaries. The σ in the parallel direction $[-1\ 2\ 1]$ at 94 °C is 2.40×10^{-6} S cm $^{-1}$, which is about 40 times higher than that in the perpendicular direction $[3\ 0\ 1]$ (5.92×10^{-8} S cm $^{-1}$ at 94 °C). This trend is similar to that in **1** (see Figure 2-6 and Table 2-2 in Section 2.3.3). The results demonstrate that the proton conduction in this system is also mediated by the H-bonds as is the case with **1**. The values of σ in both $[-1\ 2\ 1]$ and $[3\ 0\ 1]$ directions parallel and perpendicular to the H-bond network showed non-linear dependence on the reciprocal temperature like **1**. This behavior is also shown in Arrhenius plots of σT [Figure 3-7(b)]. Accordingly, the estimated activation energies E_a increase with elevating temperature (see Table 3-4).

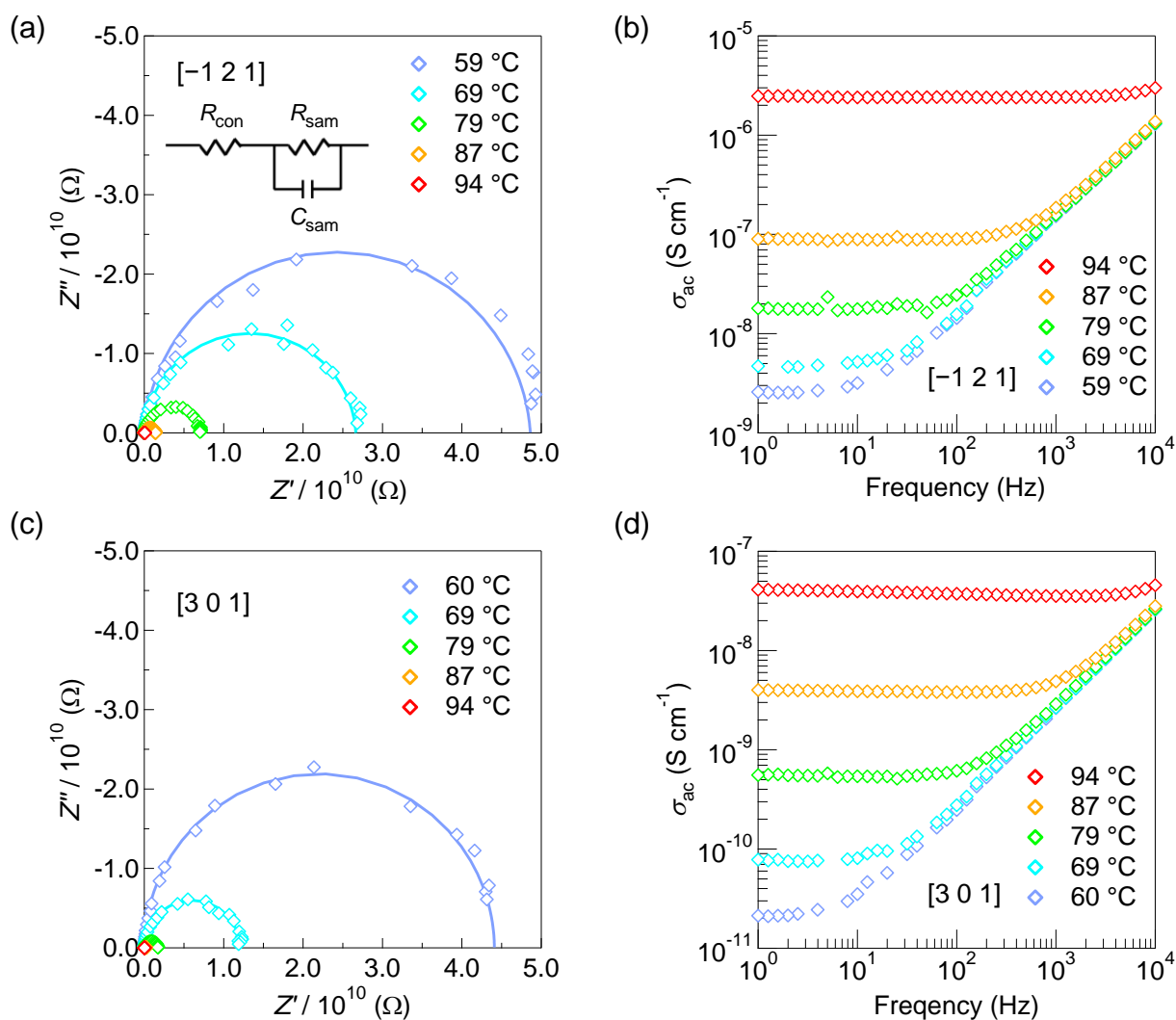


Figure 3-6. Results of the ac impedance measurements of **2**: (a, c) Cole–Cole plots measured for a single crystal of **2** along (a) the $[-1\ 2\ 1]$ and (c) $[3\ 0\ 1]$ directions at several temperatures below $94\ ^\circ\text{C}$ at which the melting starts. (b, d) Frequency dependence of σ_{ac} measured for the single crystal of **2** along the (b) the $[-1\ 2\ 1]$ and (d) $[3\ 0\ 1]$ directions at several temperatures below $94\ ^\circ\text{C}$. Open circles represent the experimental data, and solid curves represent the fitting curves obtained by using the $R_{\text{con}}R_{\text{sam}}C_{\text{sam}}$ equivalent circuit model shown in the inset of (a).

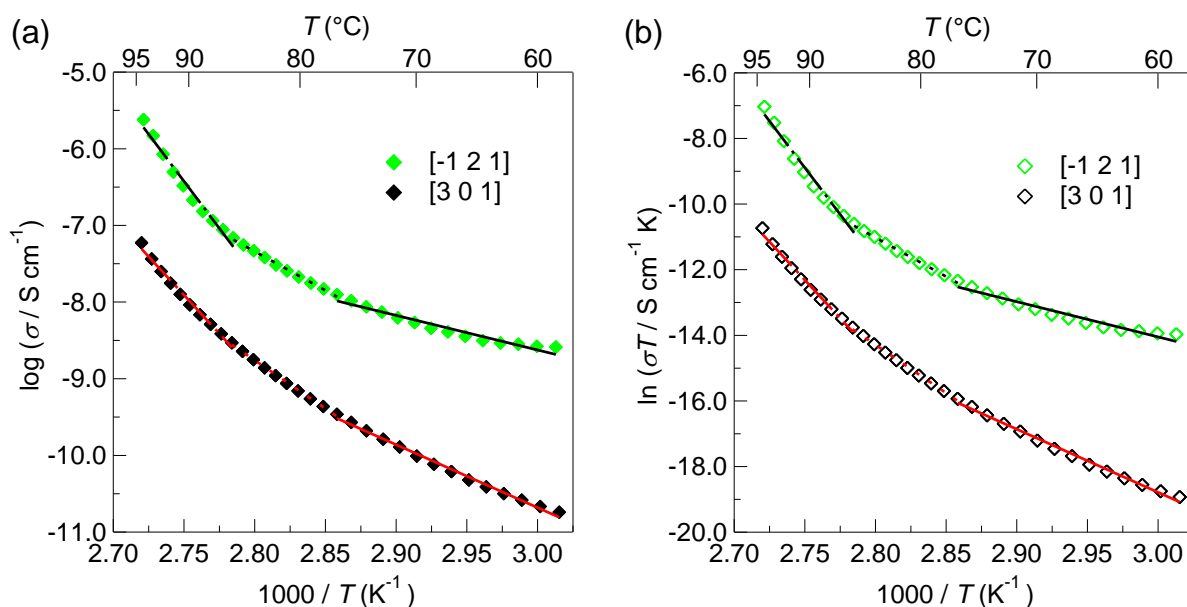


Figure 3-7. Arrhenius plots of the (a) $\log[\text{proton conductivity } (\sigma)]$ and (b) $\ln(\sigma T)$ for the single crystal of **2** measured along the $[-1\ 2\ 1]$ (green diamonds) and $[3\ 0\ 1]$ (black diamonds) directions. The fitting lines for the $[-1\ 2\ 1]$ and $[3\ 0\ 1]$ directions are denoted in black and red (solid line: 59 – 77 °C, dashed line: 77 – 86 °C, dashed-dotted line: 86 – 94 °C), respectively.

Table 3-4. Proton conductivities (σ) and activation energies (E_a) of the single crystal of **2** measured along the $[-1\ 2\ 1]$ and $[3\ 0\ 1]$ directions.

Direction	Proton conductivity σ (S cm ⁻¹)	Activation energy E_a (eV)
$[-1\ 2\ 1]$ (parallel to H-bond network)	2.40×10^{-6} [94 °C]	0.90 [59 – 77 °C], 2.02 [77 – 86 °C], 4.87 [86 – 94 °C]
$[3\ 0\ 1]$ (perpendicular to H-bond network)	5.92×10^{-8} [94 °C]	1.63 [59 – 77 °C], 2.50 [77 – 86 °C], 3.99 [86 – 94 °C]

For **3**, proton conductivities were measured along the $[0\ 1\ -1]$ and the $[0\ 1\ 1]$ directions corresponding to parallel and perpendicular to the H-bond network, respectively, as shown in Figure 3-4. As is the case with **1** and **2**, the single crystals of **3** also provided the intrinsic proton

conductivity originating from its bulk region of the crystal (Figure 3-8). The intrinsic anhydrous proton conductivities σ in the $[0\ 1\ -1]$ and $[0\ 1\ 1]$ directions, that is, parallel and perpendicular to the H-bond network, were shown in Figure 3-9. In the measurement temperature range, proton conductivity in the $[0\ 1\ -1]$ direction parallel to the H-bond network ($\sigma_{[0\ 1\ -1]} = 1.83 \times 10^{-8}\ \text{S cm}^{-1}$ at $133\ ^\circ\text{C}$) showed one order higher value than that in the $[0\ 1\ 1]$ direction perpendicular to the network ($\sigma_{[0\ 1\ 1]} = 1.60 \times 10^{-9}\ \text{S cm}^{-1}$ at $132\ ^\circ\text{C}$). This anisotropy of proton conductivity is consistent with the results of single-crystal measurements for **1** and **2** [see Figure 2-6 and Table 2-2 in Section 2.3.3 and Figure 3-7(a)]; that is, the proton conduction in **3** is mediated by the H-bonds. From these results of proton conductivity measurements on **2** and **3**, the author concluded that one of the key factors discussed for **1** in Chapter 2, the H-bonded molecular arrangements, plays an important role also in **2** and **3**.

On the other hand, the values of σ in both of the $[0\ 1\ -1]$ and $[0\ 1\ 1]$ directions showed linear dependence on the reciprocal temperature as shown in Figure 3-9(a). This behavior is also shown in Arrhenius plots of σT [Figure 3-9(b)]. The activation energies E_a in the $[0\ 1\ -1]$ and $[0\ 1\ 1]$ directions were estimated to be 2.08 (104 – 133 $^\circ\text{C}$) and 2.13 eV (104 – 132 $^\circ\text{C}$). The results are summarized in Table 3-5.

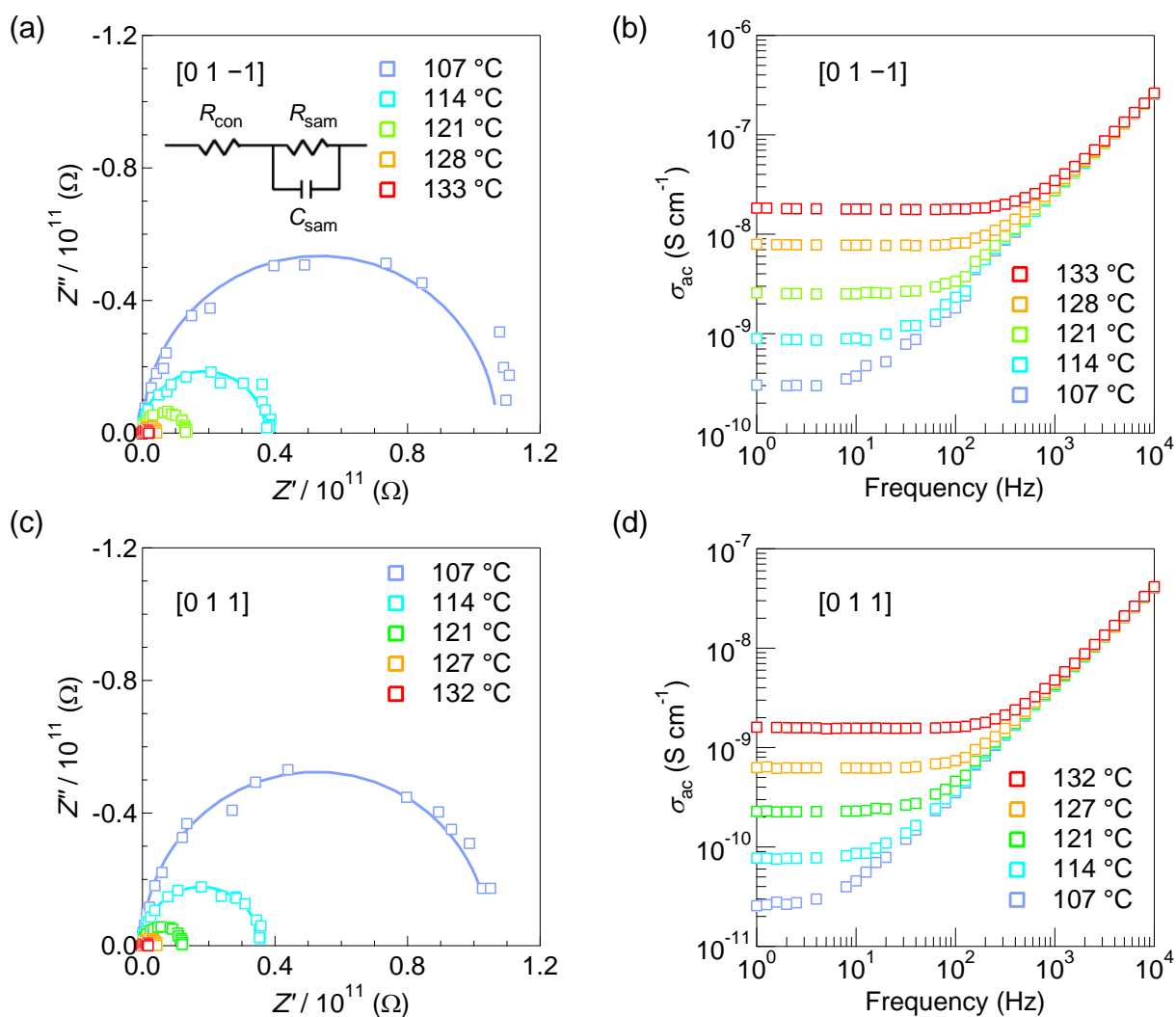


Figure 3-8. Results of the ac impedance measurements of **3**: (a, c) Cole–Cole plots measured for a single crystal of **3** along (a) the $[0\ 1\ -1]$ and (c) $[0\ 1\ 1]$ directions at several temperatures below 133 °C at which the change to the non-crystalline state starts. (b, d) Frequency dependence of σ_{ac} measured for the single crystal of **3** along the (b) the $[0\ 1\ -1]$ and (d) $[0\ 1\ 1]$ directions at several temperatures below 133 °C. Open circles represent the experimental data, and solid curves represent the fitting curves obtained by using the $R_{con}R_{sam}C_{sam}$ equivalent circuit model shown in the inset of (a).

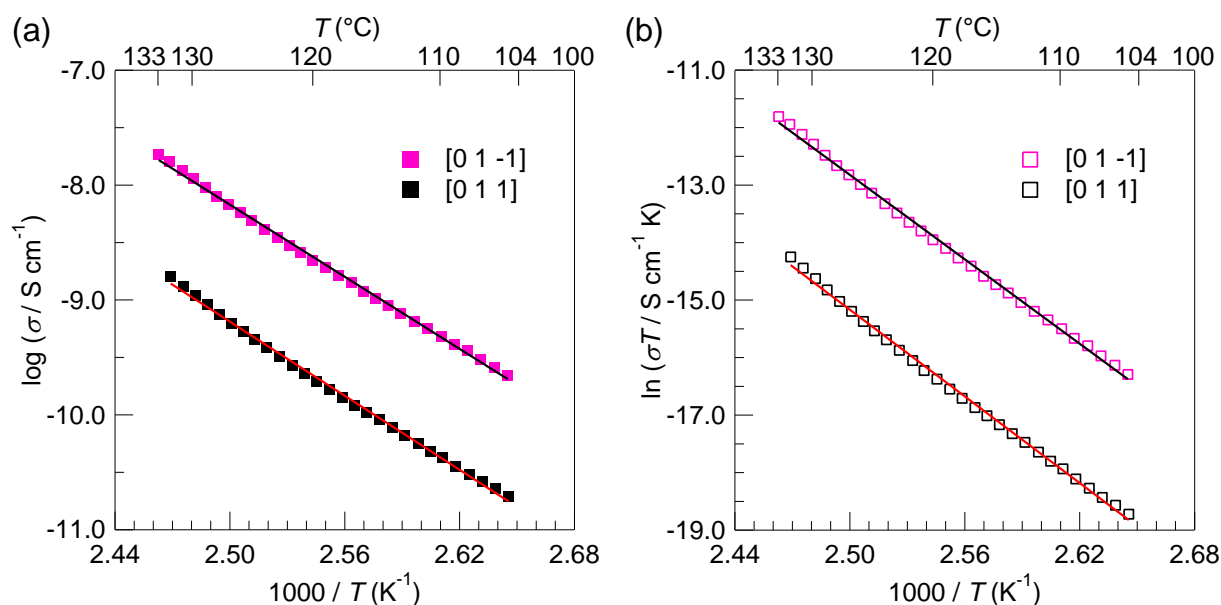


Figure 3-9. Arrhenius plots of the (a) $\log[\text{proton conductivity } (\sigma)]$ and (b) $\ln(\sigma T)$ for the single crystal of **3** measured along the $[0\ 1\ -1]$ (pink squares) and $[0\ 1\ 1]$ (black squares) directions. The fitting lines for the $[0\ 1\ -1]$ and $[0\ 1\ 1]$ directions are denoted in black and red solid lines (105 – 133 and 105 – 132 °C), respectively.

Table 3-5. Proton conductivities (σ) and activation energies (E_a) of the single crystal of **3** measured along the $[0\ 1\ -1]$ and $[0\ 1\ 1]$ directions.

Direction	Proton conductivity σ (S cm ⁻¹)	Activation energy E_a (eV)
$[0\ 1\ -1]$ (parallel to H-bond network)	1.83×10^{-8} [133 °C]	2.08 [105 – 133 °C]
$[0\ 1\ 1]$ (perpendicular to H-bond network)	1.60×10^{-9} [132 °C]	2.13 [105 – 132 °C]

3.3.2. The effect of the pK_a on the anhydrous proton conductivity

All the salts **1**, **2**, and **3** possess the 2D H-bond network structures, and the possible proton conduction pathways of them involve acid-base H-bonds. Therefore, comparison of the proton conductivity within the H-bond networks of **1**, **2**, and **3** will provide critical insights into the effect of the differences of alkyl chain structures on the conductivity in relation with the proton

donating ability pK_a . As shown in Figure 3-10, **1** (orange circles) shows more than one order higher σ than **3** (pink squares) at 105 °C (**1**: $5.85 \times 10^{-9} \text{ S cm}^{-1}$, **3**: $2.22 \times 10^{-10} \text{ S cm}^{-1}$). In addition, taking account of the difference of proton-conducting temperatures, **2** (green diamonds) shows 2 – 3 orders higher conductivity than **1** at the close temperature range [e.g., **1** (103 °C): $3.41 \times 10^{-9} \text{ S cm}^{-1}$, **2** (94 °C): $2.40 \times 10^{-6} \text{ S cm}^{-1}$].

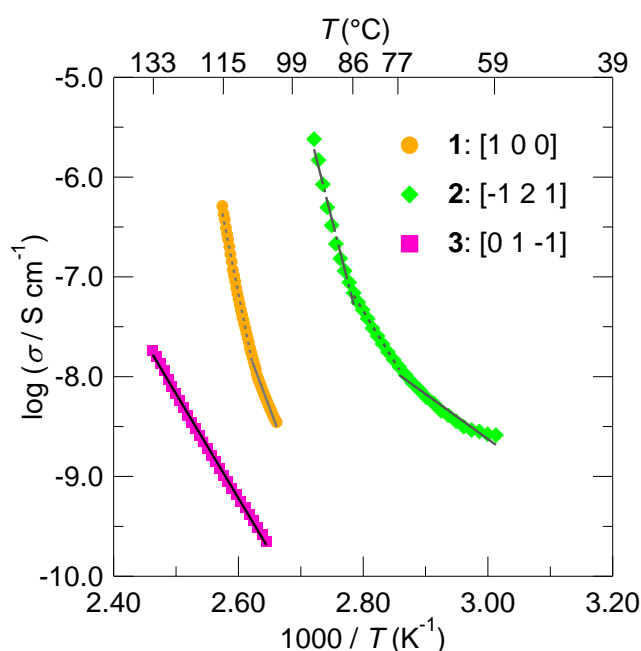


Figure 3-10. Arrhenius plots of the proton conductivity (σ) for the single crystals of **1** (orange circles), **2** (green diamonds), and **3** (pink squares) measured along the parallel directions to the H-bond networks (**1**: $[1\ 0\ 0]$, **2**: $[-1\ 2\ 1]$, **3**: $[0\ 1\ -1]$ directions). The fitting lines for the $[1\ 0\ 0]$ (**1**), $[-1\ 2\ 1]$ (**2**), and $[0\ 1\ -1]$ (**3**) directions are denoted in gray (solid line: 103 – 108 °C, dashed line: 108 – 115 °C), dark gray (solid line: 59 – 77 °C, dashed line: 77 – 86 °C, dashed-dotted line: 86 – 94 °C), and black (solid line: 105 – 133 °C), respectively.

In general, proton conduction following the Grotthuss mechanism involves proton relays between proton donor and acceptor sites (in other words, among acid and base molecules). Therefore, the author considers that the proton donating abilities, pK_{a1} [= $-\log_{10}$ (first acid

dissociation constant, K_{a1})] and pK_{aH} [$= -\log_{10} (K_a \text{ of conjugate acid of imidazole, } K_{aH})$], are one of the most important chemical parameters related to the proton conductivity. Here, ΔpK_a between the pK_{a1} values of succinic, glutaric, and fumarate acids (4.19, 4.34, and 3.03)⁴⁾ and the pK_{aH} value of imidazole (6.95)⁵⁾ are 2.76, 2.61, and 3.92 for **1**, **2**, and **3**, respectively. The order of the ΔpK_a of these salts, taking the order of their proton conductivities into account, indicates that the smaller ΔpK_a values contribute to the higher σ , which is supported by the σ – ΔpK_a trend.⁶⁾ The smaller ΔpK_a is considered to make the barrier of the proton transfer between the acid and base lower, promoting the proton relays. In conclusion, the proton donating ability of dicarboxylic acids is turned to be a key factor for tuning the proton conductivity of these salts, that is, small ΔpK_a between constituent acid and base molecules is one of the important factors to achieve the anhydrous proton conductivity.

Here, the one order higher σ of **1** than that of **3** is consistent with almost one order smaller K_{a1}/K_{aH} ($= 10^{\Delta pK_a}$) of **1**. On the other hand, the σ value of **2** is three orders higher than that of **1**, and the difference of the σ values is much large compared to the difference of K_{a1}/K_{aH} , which is less than one order difference. The much large σ difference is considered to be contributed by not only the ΔpK_a but also the differences of molecular arrangements and H-bond manners.

In addition, with elevating temperature, the σ difference between **1** and **3** increased to more than two orders at 115 °C due to difference of the temperature dependence. Interestingly, the activation energy of **3** is constant in the present temperature range, that is, **3** exhibits linear dependence on the reciprocal temperature in contrast to non-linear dependence in **1**, while **2** showed the non-linear dependence of σ like **1**. From the view point from the molecular arrangements, although all **1**, **2**, and **3** have the 2D H-bond networks, **3** has a different imidazolium orientations to the 2D H-bond network in contrast to those in **1** and **2**. The five-membered ring plane of the imidazolium cation in **3** is out of the H-bond networks.²⁾ On the other hand, the imidazolium planes in **1** and **2** are almost parallel to the networks [a dihedral angles: 2.8° (**1**)²⁾ and 3.2° – 6.6° (**2**)¹⁾]. This difference of molecular orientations of imidazolium

cations may contribute to the difference of the conductivity and also E_a . In terms of structure–property relationship, the imidazolium cation parallel to the H-bond network presumably contributes to the non-linear dependence on the reciprocal temperature because of the facts that (1) the E_a showed quite high values similar to the other imidazolium-based salts,^{1,7)} and (2) the molecular orientation of imidazolium cation is different between **1** and **3**.

3.4. Conclusion

The proton conductivities σ of single crystals of imidazolium hydrogen glutarate (**2**) and imidazolium hydrogen fumarate (**3**) and their anisotropy were determined for the first time. The obtained conductivities within the H-bond networks are much higher than those in the perpendicular directions to the networks, which is consistent with the result of **1** discussed in Chapter 2. These results demonstrate that proton conduction in the three salts occurs more readily in the H-bond network structures than along the perpendicular directions. On the other hand, comparing the σ within the H-bond networks of **1**, **2**, and **3**, **2** showed highest σ , while **3** showed lowest σ . The difference of the conductivity among the salts can be explained by proton donating ability ΔpK_a and H-bonded molecular arrangements. The salt with the smaller ΔpK_a values showed the higher σ , which is supported by the σ – ΔpK_a trend reported in the literatures.⁴⁾ Small ΔpK_a between constituent acid and base molecules is one of the important “static” factors to achieve the anhydrous proton conductivity. On the other hand, the obtained σ of **1** and **2** showed the non-linear dependence of the reciprocal temperature in contrast to the linear dependences in **3**, which is considered to be contributed by the arrangements of imidazolium cations in the H-bond network.

In conclusion, in addition to the molecular arrangements, ΔpK_a plays a crucial role to realize anhydrous proton conductivity in this system. The effects of ΔpK_a between constituent acid and base molecules in the anhydrous molecular crystals had never been unraveled, and thus the author believes that the finding about the ΔpK_a effects is one of important insights into

contributions of the “static” factor related to properties of constituent molecules to anhydrous proton conduction.

3.5. Reference

- 1) K. Pogorzelec-Glaser, J. Garbarczyk, Cz. Pawlaczyk, and E. Markiewicz, *Mater. Sci.-Pol.* **24**, 245 (2006).
- 2) J. C. MacDonald, P. C. Dorrestein, and M. M. Pilley, *Cryst. Growth Des.* **1**, 29 (2001).
- 3) K. Pogorzelec-Glaser, Cz. Pawlaczyk, A. Pietraszko, and E. Markiewicz, *J. Power Sources* **173**, 800 (2007).
- 4) (a) H. C. Brown, D. H. McDaniel, and O. Häflinger: *In Determination of Organic Structures by Physical Methods*, Academic Press, New York, U.S.A., 1955, pp 567–662. (b) R. M. C. Dawson, D. C. W. H. Elliott, and K. M. Jones: *Data for Biochemical Research*, Clarendon Press, Oxford, U.K., 1959.
- 5) T. C. Bruice, and G. L. Schmir, *J. Am. Chem. Soc.* **80**, 148 (1958).
- 6) (a) S. R. Narayanan, Shiao-Pin Yen, L. Liu, and S. G. Greenbaum, *J. Phys. Chem. B* **110**, 3942 (2006). (b) K. Pogorzelec-Glaser, A. Rachocki, P. Ławniczak, A. Pietraszko, Cz. Pawlaczyk, B. Hilczer, and M. Pugaczowa-Michalska, *CrystEngComm* **15**, 1950 (2013). (c) A. Rachocki, K. Pogorzelec-Glaser, P. Ławniczak, M. Pugaczowa-Michalska, A. Łapiński, B. Hilczer, M. Matczak, and A. Pietraszko, *Cryst. Growth Des.* **14**, 1211 (2014).
- 7) A. Kawada, A. R. McGhie, and M. M. Labes, *J. Chem. Phys.* **52**, 3121 (1970).

Chapter 4.

Effects of Molecular “Dynamics” on Anhydrous Proton Conductivity

4.1. Introduction

In Chapter 2 and 3, the “static” factors of the crystalline imidazole hydrogen dicarboxylates for the anhydrous proton conductivities were discussed. The comparison among a series of the salts **1** – **3** indicated that the H-bonded molecular arrangements and the proton donating abilities, ΔpK_a , are the important “static” factors to realize their anhydrous proton conductivities. The relationship suggests that both the existence of H-bond networks and small ΔpK_a values between imidazolium conjugated acid and dicarboxylic acids may enhance the conductivities. On the other hand, for such acid–base type anhydrous proton conductors like the imidazolium hydrogen dicarboxylates, proton conductivity is expected to be achieved based on the Grotthuss-type mechanism as mentioned in Chapter 1. Proton conduction based on the Grotthuss mechanism generally originates from the proton relay between H-bond sites involving the “dynamic” reorientations of the H-bonded molecules.¹⁾ This is often the case with the anhydrous solids, as was observed in single crystals of inorganic oxo-acid salts such as CsHSO_4 , CsH_2PO_4 , in which the orientational disorders of the oxo-acid anions increase the number of H-bond sites with the raise of the lattice symmetry (from monoclinic to cubic), resulting in the transitions to the superprotonic conducting phases ($\sigma > 10^{-3} \text{ S cm}^{-1}$).²⁾

However, the “dynamics” factors have not been discussed for the anhydrous proton conductivities of the imidazolium hydrogen dicarboxylates. The discussion on the dynamics effect may disclose the unclear observation shown in the previous chapter: a single crystal of

imidazolium hydrogen fumarate **3** exhibited the linear dependence on the reciprocal temperature in contrast to the non-linear dependence in imidazolium hydrogen succinate **1** and glutarate **2**. The preliminary solid-state ^2H NMR spectroscopy³⁾ of **1** using deuterated imidazole (imidazole- d_3) molecules (**1- d_3**) (Figure 4-1) suggested the relationship between the dynamics of imidazolium cation and its anhydrous proton conductivity. However, only insufficient temperatures were explored in the NMR study, and, in addition, it lacks the structural information in the high-temperature range, which is necessary to discuss the effect of molecular dynamics on the anhydrous proton conductivity. Besides, the imidazolium dynamics in **2** and **3** have never been investigated, which is also important to comprehensively discuss the conduction mechanism based on the comparison among a series of the salts **1** – **3**.

In this research, the author investigated the crystal structures at the proton-conducting temperatures and effects of the dynamics of the constituent molecules, especially of imidazolium cations, based on high-temperature structure analysis and the solid-state NMR measurements. The effects of the “static” factors related to the molecular arrangements, and the molecular “dynamics” on the anhydrous proton conductivity are comprehensively discussed on the basis of comparisons between these factors in each salt. The studies disclose the effects of “dynamics” of the constituent molecules to understand the mechanisms of the anhydrous proton conduction in the imidazolium hydrogen dicarboxylates.

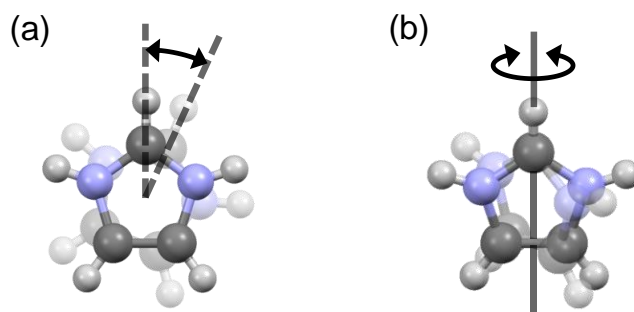


Figure 4-1. Molecular motions of imidazolium- d_3 cation proposed by the solid-state ^2H NMR study for imidazolium- d_3 hydrogen succinate ($\mathbf{1-d_3}$):³⁾ (a) The libration motion around the pseudo five-fold axis and (b) 180° -flip motion around the pseudo two-fold axis of imidazolium cation.

4.2. Experiments

Preparation of single crystals for solid-state ^2H NMR measurements

Single crystals of **2** and **3** using imidazole- d_3 molecules ($\mathbf{2-d_3}$ and $\mathbf{3-d_3}$) for solid-state ^2H NMR measurements were prepared by the following method based on that of **2** and **3** (see Section 3.2). Imidazole- d_3 was prepared by partial H/D exchange through four-times recrystallization of imidazole- d_4 [144 mg, 2 mmol, Cambridge Isotope Laboratories, Inc. (purity > 98%)] in dehydrated ethanol [3 mL, Wako Pure Chemical Industries (purity > 99.8%)]. The other chemicals were commercially available and used as received.

2- d_3 : Imidazole- d_3 [72 mg, 1 mmol] and glutaric acid [132 mg, 1 mmol, Tokyo Chemical Industry (purity > 99%)] were suspended in dehydrated methanol [3 mL, Wako Pure Chemical Industries (purity > 99.8%)]. This suspension was stirred at 40°C until all the materials were dissolved (about 10 min). The resulting solution was slowly evaporated for 3 days at room temperature, and then the precipitates were collected by filtration and washed with dehydrated ethyl acetate, to give the desired material as colorless crystals. **3- d_3** : Colorless crystals of **3- d_3** were obtained by the same method as **3**, by using Imidazole- d_3 [72 mg, 1 mmol] and fumaric acid [116 mg, 1 mmol, Wako Pure Chemical Industries (purity > 98%)].

Variable-temperature single-crystal X-ray structure analyses

Crystal structures of **1** at 103 °C and temperature dependences of the lattice constants of **1**, **2**, and **3** (**1**: 50 – 103, and 110 °C, **2**: 50 – 90 °C, **3**: 30 – 130 °C) were determined by X-ray diffraction analyses using a Rigaku Mercury II diffractometer with Mo $K\alpha$ radiation ($\lambda = 0.71073$ Å) equipped with a heated nitrogen gas flow-type temperature-control system. The crystal structures of **2-*d*₃** and **3-*d*₃** were identified to those of **2** and **3** using imidazole molecules^{4,5}) by X-ray diffraction analyses using a Rigaku Mercury II diffractometer with Mo $K\alpha$ radiation ($\lambda = 0.71073$ Å) at room temperature. The crystal structures were solved by direct methods using the SIR2008 program for **1** and **3-*d*₃** and using the SIR2004 program for **2-*d*₃**. Refinements were carried out by a full-matrix least-squares method using Crystal Structure 4.3.2 (Rigaku Corporation), in which the anisotropic temperature factors are refined for all the atoms except for disorder atoms of orientationally disordering imidazolium cation in **1** at 103 °C and hydrogen atoms in all the samples. In the crystal structure of **1** at 103 °C, hydrogen atoms of an orientationally ordering imidazolium cation were refined and the other hydrogen atoms were generated geometrically (major component of orientationally disordering imidazolium cation: C–H = 0.930 Å, N–H = 0.860 Å, succinate anions: C–H = 0.970 Å, O–H = 0.820 Å). In the structure analyses of **2-*d*₃** and **3-*d*₃**, all hydrogen atoms were refined.

Infrared spectroscopy

Infrared (IR) absorption spectra were recorded from 4000 to 800 cm⁻¹ using a Horiba FT-730 infrared spectrometer and a S100R vacuum heating microscope stage (S. T. Japan Inc.) under vacuum at room temperature. The single crystals of **2**, **2-*d*₃**, **3**, and **3-*d*₃** were crushed into powder. The powder of each material (about 0.1 – 0.3 mg) was mixed with KBr powder [100 mg, Merck KGaA], and the mixed powder was compressed to make pellet samples.

Thermal analyses

DSC curves of **1** were measured by using a Netzsch DSC 200 F3-T21 Maia calorimeter with an Al as a reference. The single crystals (6.2 mg) was encapsulated in an Al pan and heated from 20 to 110 °C with a rate of 2 °C min⁻¹ under nitrogen gas flow.

The long-term thermal stability of the crystals of **1** was evaluated by means of thermogravimeter/differential thermal analysis (TG/DTA) using a SII TG/DTA 7300 analyzer. Single crystals (6.6 or 5.5 mg) were put in an Al pan, and held at 60 °C for 30 hours or at 90 °C for 30 hours under nitrogen gas flow.

Low-frequency alternating-current impedance spectroscopy

The ac impedance measurements were performed with lower-frequency range of 10 mHz-10 kHz in the temperature range from room temperature to 92 °C. Equipment of the ac impedance spectroscopy measurements is same to that for **1**, **2**, and **3** (see Section 2.2 and 3.2). As-grown single crystals of **1** were cut into blocks (typical size of 0.4 × 0.4 × 0.5 mm³) to expose the desired faces for measurements along the [1 0 0] direction (reason of the choice of the direction is explained in Section 4.3.1). The temperature range was determined based on the result of the long-term TG/DTA measurement (see Figure 4-5 in Section 4.3.1).

The fitting for the obtained frequency dependence of σ_{ac} was operated by using the equivalent circuit consisting of one series resistance R_{con} and one parallel combination of a single resistance R_{sam} and capacitance C_{sam} [see insets of Figure 4-6(a) in Section 4.3.1]. The values of proton conductivity σ were estimated from $\sigma = |R_{sam}|^{-1} (l / S)$ in the temperature region of 68 to 92 °C because frequency-independent σ_{ac} corresponding to the dc conductivity in the low frequency region below 1 Hz was observed above 68 °C [see Figure 4-6(a) in Section 4.3.1]. The parameters l and S are thickness and area of samples.

Solid-state ^2H NMR measurements and spectral simulations

Solid-state ^2H NMR spectra were measured using a JEOL ECA-300 spectrometer with ^2H resonance frequency of 45.282 MHz. The powder samples of **2**- d_3 and **3**- d_3 [66 mg (**2**- d_3) and 140 mg (**3**- d_3)] were prepared by crushing the corresponding single crystals. The wide-line ^2H NMR spectra were measured by a quadrupole echo sequence $(90^\circ)_x - \tau - (90^\circ)_y - \tau - t_{\text{acq}}$, where τ and t_{acq} are the interval of echo and acquisition time, respectively. The 90° pulse width, τ , and t_{acq} were 2.5 μs , 20 μs , and 2.0 ms for **2**- d_3 , and 3.0 μs , 20 μs , and 2.0 ms for **3**- d_3 , respectively. The QCPMG spectra were measured by a sequence $(90^\circ)_x - \tau - (90^\circ)_y - \tau - t_{\text{acq}}/2 - (\tau - (90^\circ)_y - \tau - t_{\text{acq}})_n$, where the value of n was 64. The 90° pulse width, τ , and t_{acq} were 2.5, 20, and 50 μs for **2**- d_3 , and 3.0, 20, and 50 μs for **3**- d_3 , respectively. The temperature was controlled by heated nitrogen gas flow. In order to apodize the experimental data, the exponential window functions with the line broadening parameter 2000 Hz were applied to all the experimental and simulation data.

Simulations of the wide-line ^2H NMR spectra were performed by homemade Fortran programs using double precision.⁶⁾ The spectral simulation was performed assuming the two-site jump model of deuterons corresponding to the libration motion of the imidazolium- d_3 molecules. In this model, the imidazolium- d_3 molecules jump between two sites, the orientation of which are different from each other by θ_{lib} (degrees), with a rate of k_{lib} (Hz) [Figure 4-2(a)]. Time evolution of the NMR signal was simulated by the following equations,^{3,7)}

$$G(t, \theta, \phi) = \mathbf{W} \cdot \hat{B}_{90}^3 \exp[\hat{\mathbf{A}} t] \exp[\hat{\mathbf{A}} (\tau + t_{90})] \exp[\hat{\mathbf{A}}^* (\tau + t_{90})] \cdot \mathbf{I} \quad (4-1)$$

$$\hat{\mathbf{A}} = i \hat{\mathbf{\Omega}} + \hat{\mathbf{K}} \quad (4-2)$$

$$\hat{\mathbf{K}} = \begin{pmatrix} -k & k \\ k & -k \end{pmatrix} \quad (4-3)$$

Here, $G(t, \theta, \phi)$ is the quadrupole echo signal which is transformed to the wide-line spectrum by space averaging (*i.e.*, averaging over θ and ϕ) and Fourier transformation. W is a vector of site populations and its components are assumed as $W_1 = W_2 = 1/2$. \widehat{B}_{90} is the effect of the finite pulse width on the spectrum. \widehat{A} is an eigen value of the kinetic matrix \widehat{K} for the reversible process (libration) with the exchange rate k . τ and t_{90} are the interval of echo and the width of 90° pulse. I is the unit vector. $\widehat{\Omega}$ is the diagonal matrix with the ^2H NMR frequency ω_{qi} at site i represented by

$$\omega_{qi} = \sqrt{\frac{3}{2}} \sum_{n,m}^2 D_{0n}^{(2)*}(\psi, \theta, \phi) D_{n,m}^{(2)*}(\alpha_i, \beta_i, \gamma_i) T_m^{(2)} \quad (4-4)$$

$$T_0^{(2)} = \sqrt{\frac{3}{8}} \frac{e^2 q Q}{h}, \quad T_{\pm 2}^{(2)} = \frac{\eta}{4} \frac{e^2 q Q}{h}, \quad (4-5)$$

where D is the second-order Wigner rotation matrix.⁸⁾ $(\alpha_i, \beta_i, \gamma_i)$ is Euler angle for the transformation from the molecular axes to the principal axes of the electric field gradient tensor, and (ψ, θ, ϕ) is that from the laboratory axes to the molecular axes, respectively. $e^2 q Q/h$ and η are the quadrupole coupling parameter and anisotropy parameter. The exchange rate k corresponds to the libration rate k_{lib} , and the angle β_i corresponds to the libration angle θ_{lib} .

The examples of wide-line spectra simulated based on the two-site jump model [Figure 4-2(a)] with several values of the k_{lib} and θ_{lib} are shown in Figure 4-2(b). The spectrum with $k_{\text{lib}} = 10^0$ Hz and $\theta_{\text{lib}} = 0^\circ$ (corresponding to no libration motion) shows a typical shape in solid-state ^2H NMR for powder sample, so-called Pake doublet⁹⁾ [lower spectrum in Figure 4-2(b)]. With increasing the values of k_{lib} and θ_{lib} , the peaks in these spectra become closer to each other. This reflects that the nuclear quadrupole interactions of deuterons in the C–D bonds of imidazolium- d_3 cation are averaged by the libration motion with the angle θ_{lib} ; the nuclear

quadrupole interactions are averaged more with increasing the k_{lib} and θ_{lib} , corresponding to the closer peak position to the center.

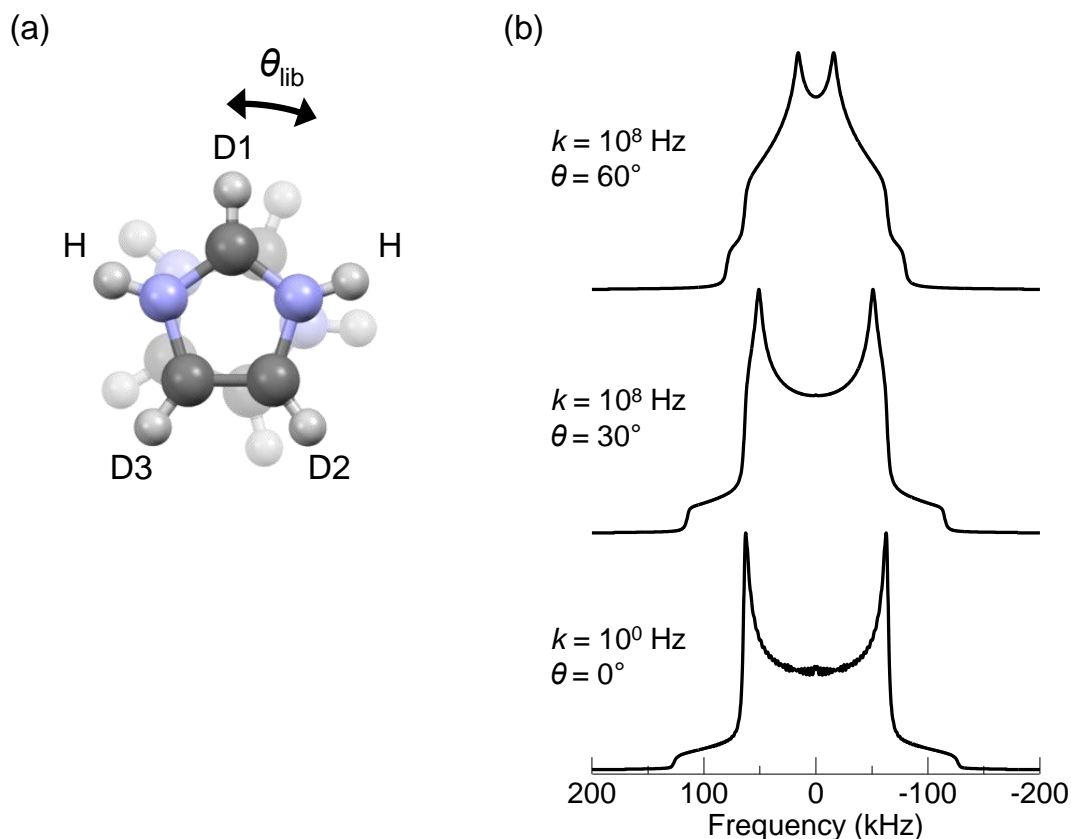


Figure 4-2. (a) Schematic image of the two-site jump model adopted for the spectral simulations, corresponding to the libration of imidazolium- d_3 molecule.³⁾ (b) Single-component simulations of wide-line ^2H NMR spectra using (upper) libration rate $k_{\text{lib}} = 10^8$ Hz and angle $\theta_{\text{lib}} = 60^\circ$, (middle) 10^8 Hz and 30° , and (lower) 10^0 Hz and 0° . Fixed values of $e^2qQ/\hbar = 170$ kHz and $\eta = 0.00$ were used for the simulation in (b).

In the analyses of the wide-line ^2H NMR spectra, each spectrum was analyzed by a single component changing the parameters e^2qQ/\hbar , η , k_{lib} , and θ_{lib} , on the assumption that all imidazolium cations in **2- d_3** show the same two-site jump with the same k_{lib} and θ_{lib} . All the parameters were determined by adjusting the simulated spectrum to the corresponding experimental spectrum. At first, the analysis on the spectrum at room temperature was

performed to determine the values of e^2qQ/\hbar and η . In the determination of the values of e^2qQ/\hbar and η at room temperature, the k_{lib} and θ_{lib} were set to zero in the analyses of **2**- d_3 , whereas those were set to finite values of k_{lib} , and θ_{lib} in the analyses of **3**- d_3 because the experimental spectra could not be reproduced with the values $k_{\text{lib}} = 10^0$ Hz and $\theta_{\text{lib}} = 0^\circ$. For the analyses on the spectra at higher temperatures, fixed values of e^2qQ/\hbar and η determined by the simulations at room temperature were used, and the k_{lib} and θ_{lib} were adjusted.

4.3. Results and discussion

4.3.1. Activation of molecular motion of imidazolium cations and its effects on proton conduction in imidazolium hydrogen succinate

In order to obtain the structural information of **1** in the range of proton-conducting temperature, temperature dependence of the lattice constants of **1** was investigated on the heating process by high-temperature (high- T) X-ray crystal structure analysis. As shown in Figure 4-3, the b -axis length and the cell volume doubled around 80 °C, which is accompanied by an endothermic process observed in DSC (lower graph in Figure 4-3). The endothermic process was started from 75 °C and finished at 80 °C with the peak temperature of 77 °C. The enthalpy change ΔH was estimated to be 0.32 kJ mol⁻¹ ($= 0.33 \times 10^{-2}$ eV), and the entropy change ΔS at 77 °C was 0.91 J mol⁻¹ K⁻¹. The observed sudden changes in the b -axis length and cell volume together with the peak in DSC curve indicate the structural phase transition around 80 °C.

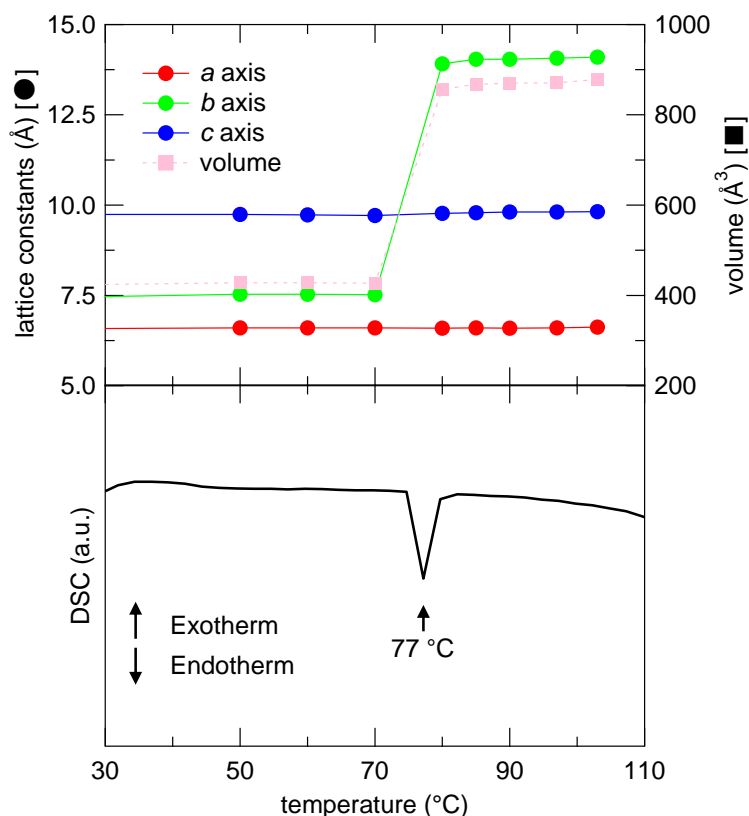


Figure 4-3. (upper) The temperature-dependence of the lattice constants and volume of **1** obtained by the single-crystal X-ray diffraction experiments, and (lower) the DSC curve of single crystals of **1** in the heating process from 20 °C to 110 °C with a rate of 2 °C min⁻¹.

Crystal structure above 80 °C was successfully solved at 103 °C (Table 4-1). It is revealed that half of imidazolium cations are disordered above 80 °C. In the high-*T* structure, the number of crystallographically independent layers with the H-bond networks become two [Figure 4-4(a)], while the number is only one at room temperature [Figure 4-4(b)] (23 °C). In one layer of the high-*T* structure, imidazolium cations show an orientational disorder within the five-membered ring plane [Figure 4-4(c)], while those in the other layer maintain the ordered orientation from the room-temperature structure [Figure 4-4(d)], resulting in the doubled *b*-axis length. In the disordered layer, the occupancy ratio of the normal to disordered imidazolium cations is 0.74 : 0.26 at 103 °C. The disordered atoms in the minor component are observed as averaged nitrogen/carbon atoms switched with the in-plane molecular motion [*e.g.*, a libration

motion proposed by the solid-state ^2H NMR study:³⁾ see Figure 4-1(a) in Section 4.1]. The position of the disordered layer relative to the neighboring layers [Figure 4-4(e)] shifts from that of a layer at room temperature [Figure 4-4(f)]. The displacement is more than 6 Å (*i.e.*, more than the length of the succinate anion). On the other hand, the entropy change ΔS at 77 °C 0.91 J mol⁻¹ K⁻¹ observed in the DSC is much smaller than the configurational entropy ΔS_{conf} 3.57 J mol⁻¹ K⁻¹ estimated on the basis of the following equation assuming random 3-site jump (*i.e.*, the libration motion) of the disordered atoms in imidazolium cation,

$$\Delta S_{\text{conf}} = R \ln W = R \ln \left(\frac{1}{2} C_{\frac{26}{100 \times 2}} \times 3^{\frac{26}{100 \times 2}} \right) \quad (4-6)$$

where R is gas constant. W is the number of possible configurations of the disordered atoms. The small value of ΔS compared to ΔS_{conf} indicates that the observed phase transition is not an order-disorder transition but a structural transition, which coincides with activation of imidazolium libration motion. Therefore, the high- T structure analyses revealed that **1** shows the structural phase transition accompanied by the change of stacking arrangement of the layers with the H-bond networks at 80 °C, and that imidazolium cations in the half of the layers show the orientational disorder at 103 °C, that is, the activation of the libration motion in high- T region around the transition temperature.

Table 4-1. Crystallographic data of **1** at 20 and 103 °C.

Temperature (°C)	20	103
Crystal system	triclinic	triclinic
Space group	<i>P</i> −1	<i>P</i> −1
<i>a</i> (Å)	6.595(3)	6.601(18)
<i>b</i> (Å)	7.431(3)	14.02(4)
<i>c</i> (Å)	9.672(3)	9.81(3)
α (°)	67.859(10)	102.46(4)
β (°)	73.984(12)	99.31(4)
γ (°)	81.429(13)	94.80(4)
Volume (Å ³)	421.5(3)	868(4)
<i>Z</i>	2	4
<i>D</i> _{calc} (g cm ^{−3})	1.467	1.424
λ (Å)	0.71073	0.71073
<i>R</i> _{int}	0.0172	0.1070
<i>R</i> ₁ (<i>I</i> > 2.00σ(<i>I</i>))	0.0442	0.0979
<i>wR</i> ₂ (all reflections)	0.1333	0.2504
GOF	1.052	0.922
CCDC number	1957600	1957481

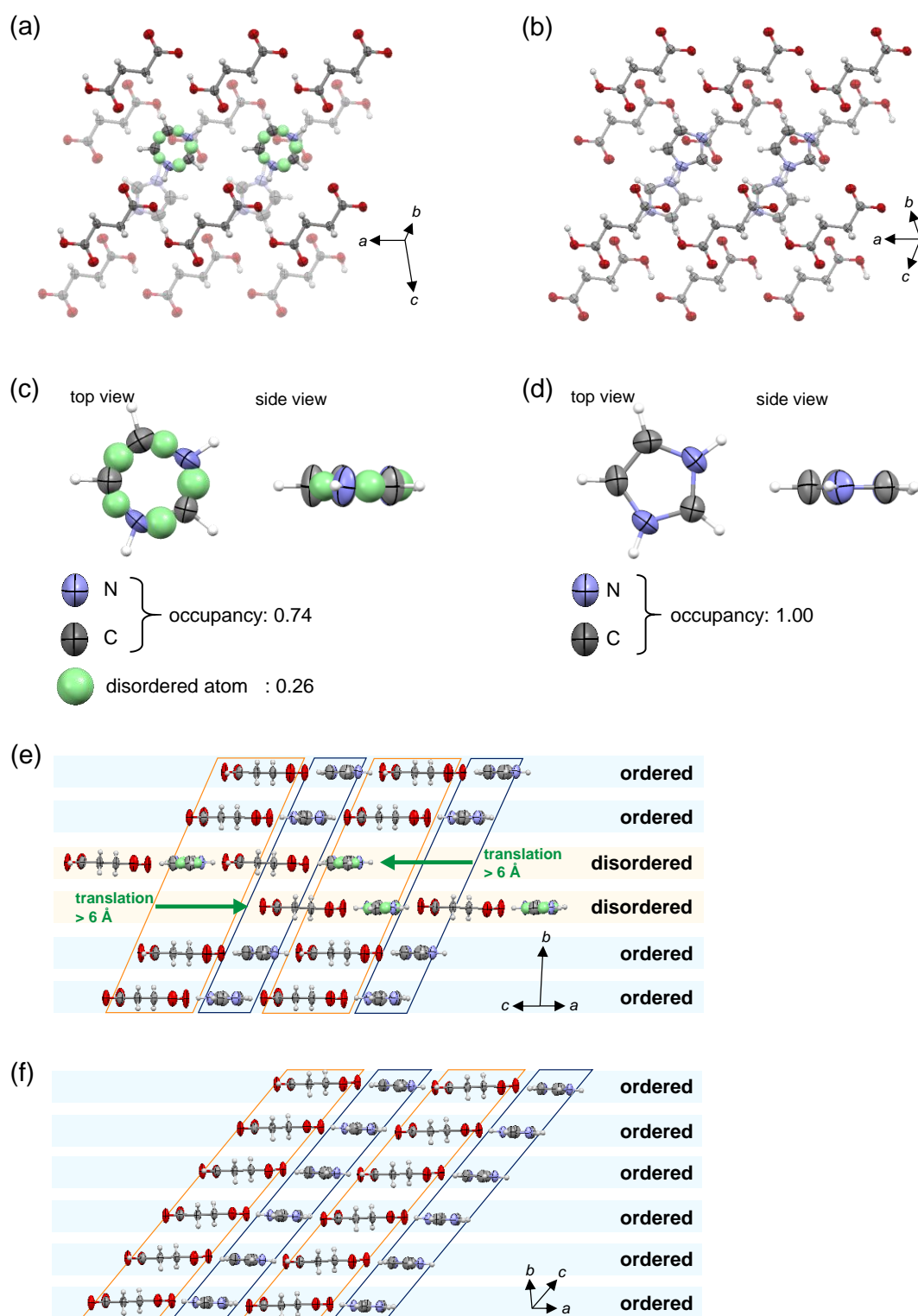


Figure 4-4. Crystal structure of 1. (a, b) A top view of stacking arrangements of 2D H-bond networks at (a) 103 °C and (b) 23 °C. (c, d) Orientations of imidazolium molecule at (c) 103 °C and (d) 23 °C. (e, f) A side view of the networks at (e) 103 °C and (f) 23 °C. In (e) and (f), orange and dark blue boxes represent columns of imidazolium and succinate ions, respectively.

Although the proton conductivity of **1** had been observed above 103 °C (see Figure 2-4 – 2-7 in Section 2.3.2 and 2.3.3), the molecular dynamics of imidazolium cations is considered to be activated above ca. 80 °C. To investigate the relationship between the observed molecular dynamics and proton conductivity, proton conductivity σ in the temperature range lower than 103 °C was measured by an impedance spectroscopy in a lower frequency range, 10 mHz – 10 kHz. Prior to the low-frequency impedance measurements, the long-term thermal stability of **1** in the high- T phase was investigated by means of the TG/DTA experiments because the low-frequency measurements take long time. As shown in Figure 4-5, a significant mass loss (> 1.0 %) of the single crystals was observed after keeping at 90 °C for 12.5 hours (= 750 min) [Figure 4-5(a)], while the mass loss was not significant after keeping at 60 °C for 30 hours [Figure 4-5(b)]. The significant mass loss is thought to occur after keeping at a temperature above 80 °C, that is, above the phase transition temperature, for a long time of about 12.5 hours.

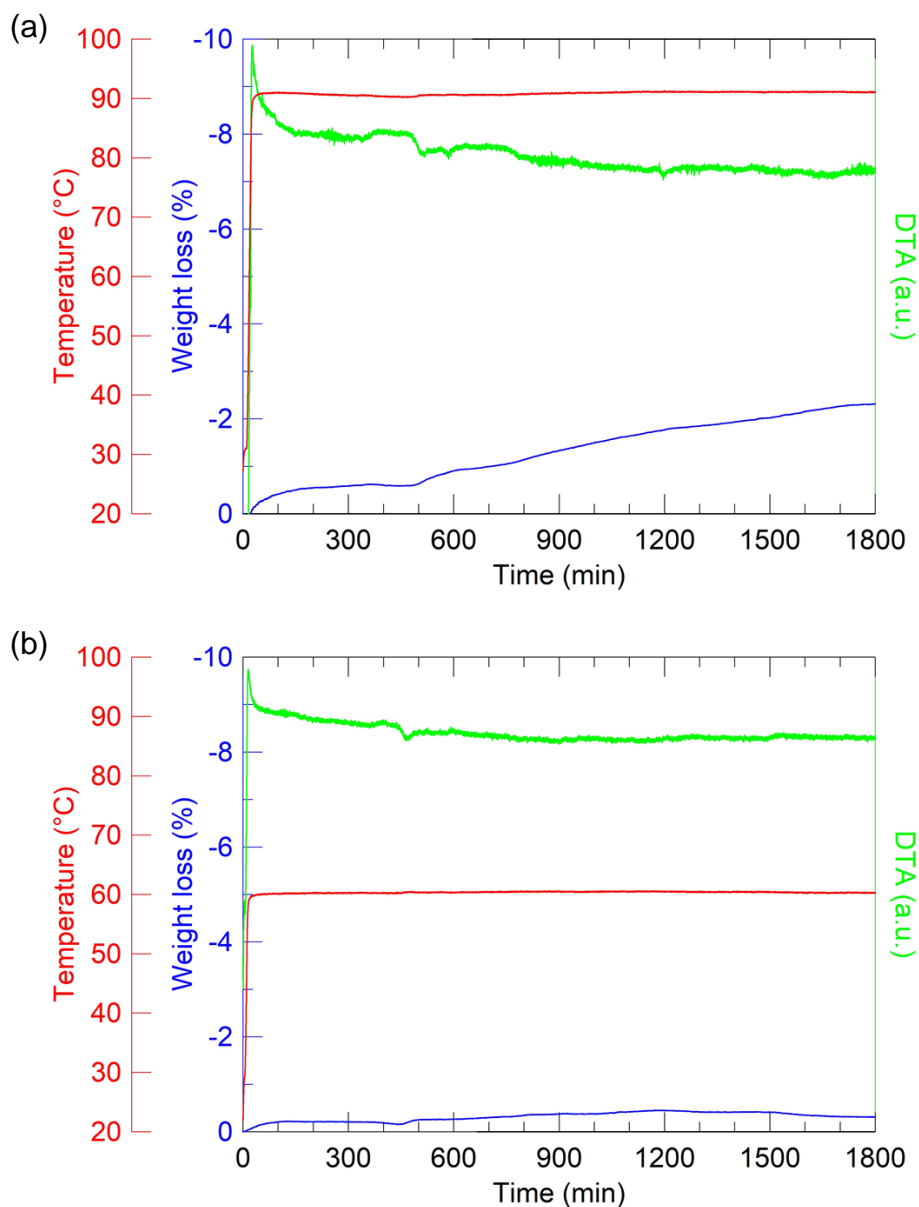


Figure 4-5. Time dependence of temperature, weight loss, and DTA of single crystals of **1** at (a) 90 °C or at (b) 60 °C.

Based on the result of the long-term TG/DTA measurements, the proton conductivity σ of **1** in the temperature range of room temperature $< T < 92$ °C was measured in the lower frequency range of 10 mHz – 10 kHz. The low-frequency measurements of **1** were operated for the [1 0 0] direction because proton conduction in this direction is considered to be more easily affected by the libration motion of imidazolium cation [see Figure 2-9(a) in Section 2.3.4].^{3,10)} As shown in Figure 4-6(a), the dielectric relaxation corresponding to proton migration was observed also

below 92 °C (*e.g.*, the dielectric relaxation around 10 Hz at 92 °C). The obtained frequency-dependent impedances were analyzed by fitting (solid lines) using the $R_{\text{con}}R_{\text{sam}}C_{\text{sam}}$ equivalent circuit (inset) for 0.19 Hz – 10 kHz. The ac conductivity σ_{ac} at 0 Hz, that is, the dc conductivity σ_{dc} was estimated by extrapolations (dash lines) of the fitting profiles calculated using the R_{con} , R_{sam} , and C_{sam} values, and were defined as the values of proton conductivity σ as shown in Figure 4-6(b) (pink circles). The obtained σ showed a significant increase as non-linear dependence on the reciprocal temperature. The activation energy E_a 2.90 eV above 80 °C coincides with the value of E_a above 103 °C (3.32 eV) obtained by the ac impedance measurements in the range of 1 Hz – 1 MHz (Table 4-2, see also Section 2.3.3), and is similarly high as those of the imidazole-based salts (1.6 – 2.5 eV)¹¹⁾ and the imidazole single crystal (1.9 eV).¹²⁾ These results indicate that the libration motion of imidazolium cation promotes proton conduction in **1**. The results of the analysis are summarized in Table 4-2.

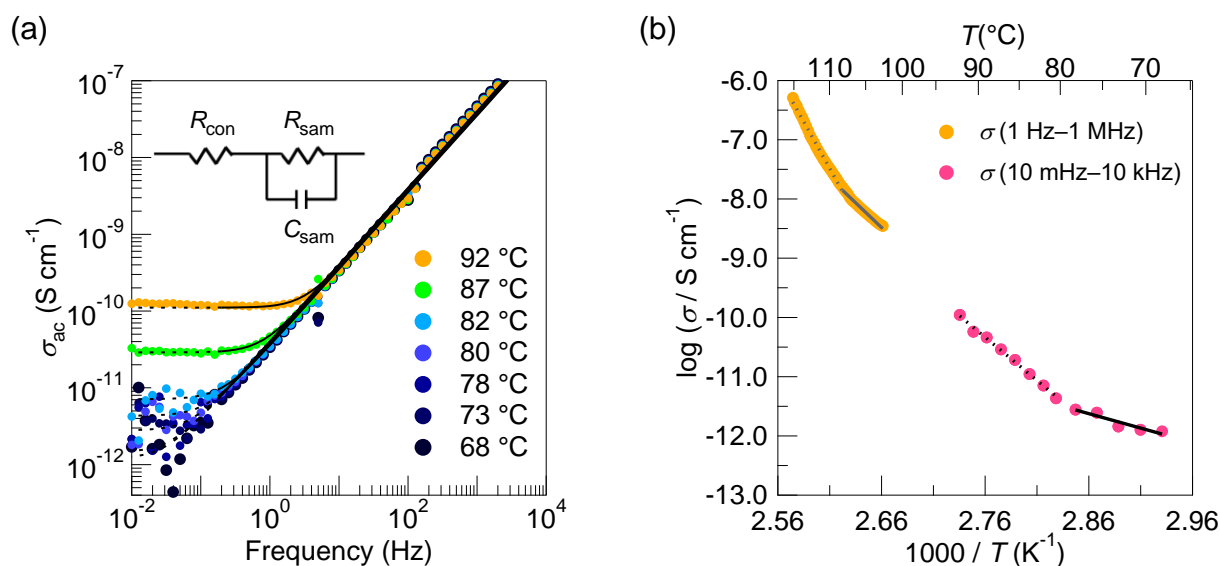


Figure 4-6. Results of the low-frequency measurements of ac conductivities (σ_{ac}) for **1**: (a) Frequency dependence of σ_{ac} measured for 10 mHz – 10 kHz using a single crystal of **1** along the [1 0 0] direction at several temperatures. (b) Arrhenius plots of the proton conductivity (σ) for the single crystals of **1** measured along the [1 0 0] direction for 1 Hz – 1 MHz (orange circles) and 10 mHz – 10 kHz (pink circles), respectively. In (a), the circles represent the experimental data. The black solid curves represent the fitting curves using the $R_{con}R_{sam}C_{sam}$ equivalent circuit shown in the inset, and black dash curves represent the extrapolations of the fitting profiles calculated using the R_{con} , R_{sam} , and C_{sam} values. In (b), the fitting lines for the plots are denoted in gray lines (solid line, 103 – 108 °C; dashed line, 108 – 115 °C) and black lines (solid line, 68 – 78 °C; dashed line, 80 – 92 °C), respectively. The σ values of the experiments for 10 mHz – 10 kHz were estimated from the extrapolation of the fitting curves to 0 Hz. The σ for 1 Hz – 1 MHz was taken experimentally from the values at 1 Hz (see Section 2.3.2).

Table 4-2. Proton conductivities (σ) and activation energies (E_a) of the single crystals of **1** measured along the [1 0 0] direction for 10 mHz – 10 kHz and 1 Hz – 1 MHz.

Frequency range	Proton conductivity σ (S cm ⁻¹)	Activation energy E_a (eV)
10 mHz – 10 kHz	1.11×10^{-10} [92 °C]	0.97 [68 – 78 °C], 2.90 [80 – 92 °C]
1 Hz – 1 MHz	3.41×10^{-9} [103 °C]	3.32 [103 – 108 °C], 6.24 [108 – 115 °C]

In contrast to **1**, although the proton conductivity of **2** and **3** was also expected to be contributed by the dynamics of constituent molecules as is the case with **1**, no significant changes in molecular arrangements and orientations but only slight changes of relative positions of the stacking networks were observed at proton-conducting temperatures in the high- T X-ray structure analyses for **2** and **3** (Table 4-3 and 4-4). In **2**, the a -axis length along the network-stacking direction slightly increased from 8.43 Å at 22 °C to 8.50 Å at 90 °C, and the β angle slightly decreased from 103.49° at 22 °C to 102.85° at 90 °C. These lattice constant changes originate from an increase of the distance between the H-bond network layers; for example, the distance between imidazolium nitrogen and glutarate oxygen atoms in neighboring networks increased from 3.41 to 3.46 Å. In **3**, similar changes were observed like **2**. The lengths of the b -axis and the c -axis corresponding to the network-stacking direction slightly increased from 7.76 (the b -axis) and 8.41 (the c -axis) Å at 22 °C to 7.84 (the b -axis) and 8.46 (the c -axis) Å at 130 °C, respectively. The α and β angles decreased from 69.72° (α) and 81.35° (β) to 69.16° (α) and 80.94° (β). The distance between the layers increased, resulting in an increase of an N \cdots O distance between neighboring networks (from 3.77 to 3.79 Å).

Table 4-3. Crystallographic data of **2** in the heating process.

Temperature (°C)	25	50	60	70	80	90
Crystal system	triclinic	triclinic	triclinic	triclinic	triclinic	triclinic
Space group	<i>P</i> −1	<i>P</i> −1	<i>P</i> −1	<i>P</i> −1	<i>P</i> −1	<i>P</i> −1
<i>a</i> (Å)	8.43	8.43	8.44	8.45	8.46	8.5
<i>b</i> (Å)	13.66	13.64	13.64	13.64	13.65	13.67
<i>c</i> (Å)	17.02	17.01	17.02	17.03	17.04	17.06
α (°)	90.39	90.42	90.4	90.37	90.38	90.36
β (°)	103.49	103.17	103.09	103.03	102.94	102.85
γ (°)	91.21	91.03	91.06	91.07	91.07	91.05
Volume (Å ³)	1906	1912	1912	1923	1919	1931

Table 4-4. Crystallographic data of **3** in the heating process.

Temperature (°C)	30	50	70	90
Crystal system	triclinic	triclinic	triclinic	triclinic
Space group	<i>P</i> −1	<i>P</i> −1	<i>P</i> −1	<i>P</i> −1
<i>a</i> (Å)	7.48	7.48	7.5	7.5
<i>b</i> (Å)	7.76	7.78	7.8	7.82
<i>c</i> (Å)	8.41	8.42	8.45	8.46
α (°)	69.72	69.57	69.45	69.34
β (°)	81.35	81.17	81.15	81.08
γ (°)	66.15	66.04	66.1	66.01
Volume (Å ³)	420	419	423	424

Temperature (°C)	100	110	120	130
Crystal system	triclinic	triclinic	triclinic	triclinic
Space group	<i>P</i> −1	<i>P</i> −1	<i>P</i> −1	<i>P</i> −1
<i>a</i> (Å)	7.49	7.49	7.49	7.48
<i>b</i> (Å)	7.82	7.83	7.83	7.84
<i>c</i> (Å)	8.46	8.47	8.46	8.46
α (°)	69.27	69.19	69.16	69.16
β (°)	81.02	80.94	80.95	80.94
γ (°)	66.02	65.97	65.99	65.95
Volume (Å ³)	423	424	423	424

4.3.2. Local libration motion of imidazolium cations and its effect on the anhydrous proton conduction in the three analogue salts

Although the proton conductivity of **2** and **3** was expected to be contributed by the dynamics of constituent molecules, no significant changes in the crystal structures, molecular arrangements or orientations, were observed at proton-conducting temperatures in the X-ray structure analyses. While X-ray crystallography can investigate the averaged structural information, solid-state ^2H NMR spectroscopy enables us to investigate the local environment of the components such as local structure or molecular dynamics.^{3,7)} Therefore, the author performed the solid-state ^2H NMR experiments for **2** and **3** in order to investigate the local dynamics of imidazolium cations.

Single crystals of **2-*d*₃** and **3-*d*₃** were prepared by using deuterated imidazole (imidazole-*d*₃), and their structures were identified to those of **2** and **3** using imidazole molecules^{4,5)} (Table 4-5 and 4-6).

Table. 4-5. Crystallographic data of **2**⁴⁾ and **2-d**₃.

Material	2 ⁴⁾	2-d ₃
Temperature (°C)	20	25
Crystal system	triclinic	triclinic
Space group	<i>P</i> −1	<i>P</i> −1
<i>a</i> (Å)	8.420(2)	8.417(0)
<i>b</i> (Å)	13.685(3)	13.651(1)
<i>c</i> (Å)	17.068(3)	16.992(1)
<i>α</i> (°)	90.62(3)	90.43(1)
<i>β</i> (°)	103.45(3)	103.44(1)
<i>γ</i> (°)	91.03(3)	91.02(0)
Volume (Å ³)	1912.23	1898.57
<i>Z</i>	8	8
<i>D</i> _{calc} (g cm ^{−3})	1.391	1.401
<i>λ</i> (Å)	0.71073	0.71073
<i>R</i> _{int}	—	0.0349
<i>R</i> ₁ (<i>I</i> > 2.00σ(<i>I</i>))	0.0668	0.0670
<i>wR</i> ₂ (all reflections)	—	0.2172
GOF	1.052	1.065
CCDC number	225442	—

Table. 4-6. Crystallographic data of **3**⁵⁾ and **3-*d*₃**.

Material	3 ⁵⁾	3-<i>d</i>₃
Temperature (°C)	24	25
Crystal system	triclinic	triclinic
Space group	<i>P</i> –1	<i>P</i> –1
<i>a</i> (Å)	7.478(2)	7.435(1)
<i>b</i> (Å)	7.747(2)	7.692(1)
<i>c</i> (Å)	8.416(2)	8.363(1)
<i>α</i> (°)	69.69(2)	69.83(1)
<i>β</i> (°)	81.42(2)	81.39(1)
<i>γ</i> (°)	66.18(2)	66.17(1)
Volume (Å ³)	418.272	410.64
<i>Z</i>	2	2
<i>D</i> _{calc} (g cm ^{–3})	1.462	1.489
<i>λ</i> (Å)	0.71069	0.71073
<i>R</i> _{int}	0.0172	0.0297
<i>R</i> ₁ (<i>I</i> > 2.00σ(<i>I</i>))	0.0420	0.0501
<i>wR</i> ₂ (all reflections)	0.1213	0.1483
GOF	1.048	1.072
CCDC number	1211264	—

The partial H/D exchange from imidazole-*d*₄ to imidazole-*d*₃ molecules was confirmed by changes in the infrared absorbance peaks of C–H(D) and N–H(D) vibration modes, as shown in Figure 4-7.¹³⁾ For **2-*d*₃** [blue line in Figure 4-7(a)], the prepared crystal was thought to include almost no imidazolium-*d*₄ molecules, because of no appearances of the N–D stretching modes of imidazole-*d*₄ molecule in the band from 2320 to 1860 cm^{–1} in contrast to appearances of the N–H stretching modes of imidazole molecule-*d*₃ in 3020–2580 cm^{–1}. The C–D stretching mode of imidazole-*d*₃ molecule appeared at 2383 cm^{–1}, while the C–H stretching mode of imidazole molecule appeared at 3128 cm^{–1} in the spectrum of **2** (green line). The C–H bending modes appearing at 1097 cm^{–1} for **2** were changed to the C–D bending modes at 955 cm^{–1} for **2-*d*₃**.

As shown in Figure 4-7(b), in the spectrum of **3-*d*₃** (blue line), the N–D stretching modes of

imidazole- d_4 molecule did not appear in the band from 2320 to 1860 cm^{-1} . On the other hand, the N–H stretching modes of imidazole molecule- d_3 appeared in the band from 3020 to 2580 cm^{-1} for both of **3** (pink line) and **3- d_3** . For **3- d_3** , The C–D stretching mode of imidazole- d_3 molecule appeared at 2387 cm^{-1} , while the C–H stretching mode of imidazole molecule appeared at 3154 cm^{-1} in the spectrum of **3**. The C–H bending mode appearing at 1109 cm^{-1} for **3** were changed to the C–D bending mode at 943 cm^{-1} for **3- d_3** . Therefore, the prepared crystal of **3- d_3** was thought to include almost no imidazolium- d_4 but imidazolium- d_3 molecules.

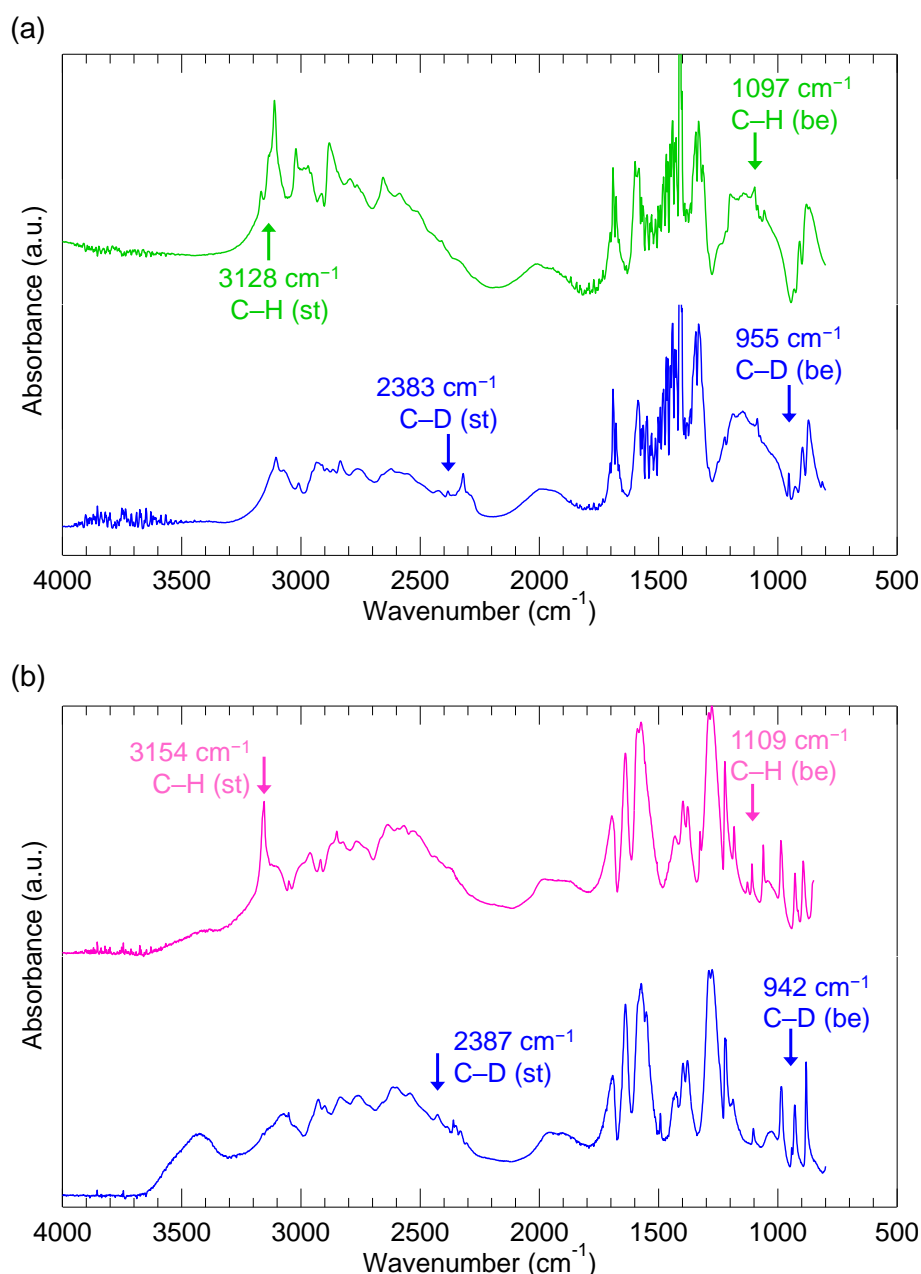


Figure 4-7. The infrared spectra of (a) **2** (green line) and **2- d_3** (blue line) and of (b) **3** (pink line) and **3- d_3** (blue line) (st: the stretching modes, be: the bending modes).

The prepared single crystals were crushed into powder samples for the ^2H NMR measurements. The ^2H NMR measurements using the powder samples can be operated more easily than that using single crystals. In addition, the obtained results for **2- d_3** and **3- d_3** can be compared with those for **1- d_3** reported in the literature,³⁾ permitting a systematic discussion about the effects of dynamics of imidazolium cations. This time, both wide-line spectra and

quadrupole Carr-Purcell-Meiboom-Gill (QCPMG) spectra were measured. Both techniques are sensitive to detect dynamics with the rate of kHz–MHz order, but QCPMG spectra are more sensitive to slower motions than the wide-line spectra.¹⁴⁾

The wide-line ^2H spectra for **2**- d_3 from 23 to 50 °C are shown in Figure 4-8. These spectra showed the Pake doublet shape,⁹⁾ as shown by the spectra at 23 °C [Figure 4-8(a)]. Although the spectrum change is not easily realized due to the broad peaks by relatively low S/N ratio attributed to the small amount of the powder sample (66 mg: see Section 4.2), two peaks of the doublet move towards 0 Hz and become closer to each other from 40 °C to 50 °C [Figure 4-8(b), (c)], in contrast to no significant change from 23 to 40 °C [Figure 4-8(d)]. The change of the peak positions from 40 °C to 50 °C is considered to be caused by the activation of the libration motion or the increase of the libration angle of imidazolium- d_3 cation (see Section 4.2). On the assumption that all imidazolium cations in **2**- d_3 show the same libration motion, the analysis of the imidazolium dynamics was performed by a single-component simulation spectrum based on the two-site jump model (Figure 4-9), which describes the libration motion suggested in the literatures^{3,7)} (see Section 4.2). The results of spectral analyses [green lines in Figure 4-9(a) and (b)] indicate that imidazolium cations exhibit the libration motion with significantly fast rates $k_{\text{lib}} \geq 10^9$ Hz above 50 °C (Table 4-7). On the other hand, at 23 and 40 °C, the rates were not significantly fast ($k_{\text{lib}} \leq 10^0$ Hz), indicating the magnitude of the libration is very small. Therefore, the libration motion is considered to be activated above 50 °C which is close to the proton-conducting temperature (59 – 94 °C). In addition, the θ_{lib} increased from 13° at 50 °C to 16° at 90 °C (Table 4-7). This indicates that the proton conduction in **2** is promoted by the libration motion of imidazolium cation above 50 °C.

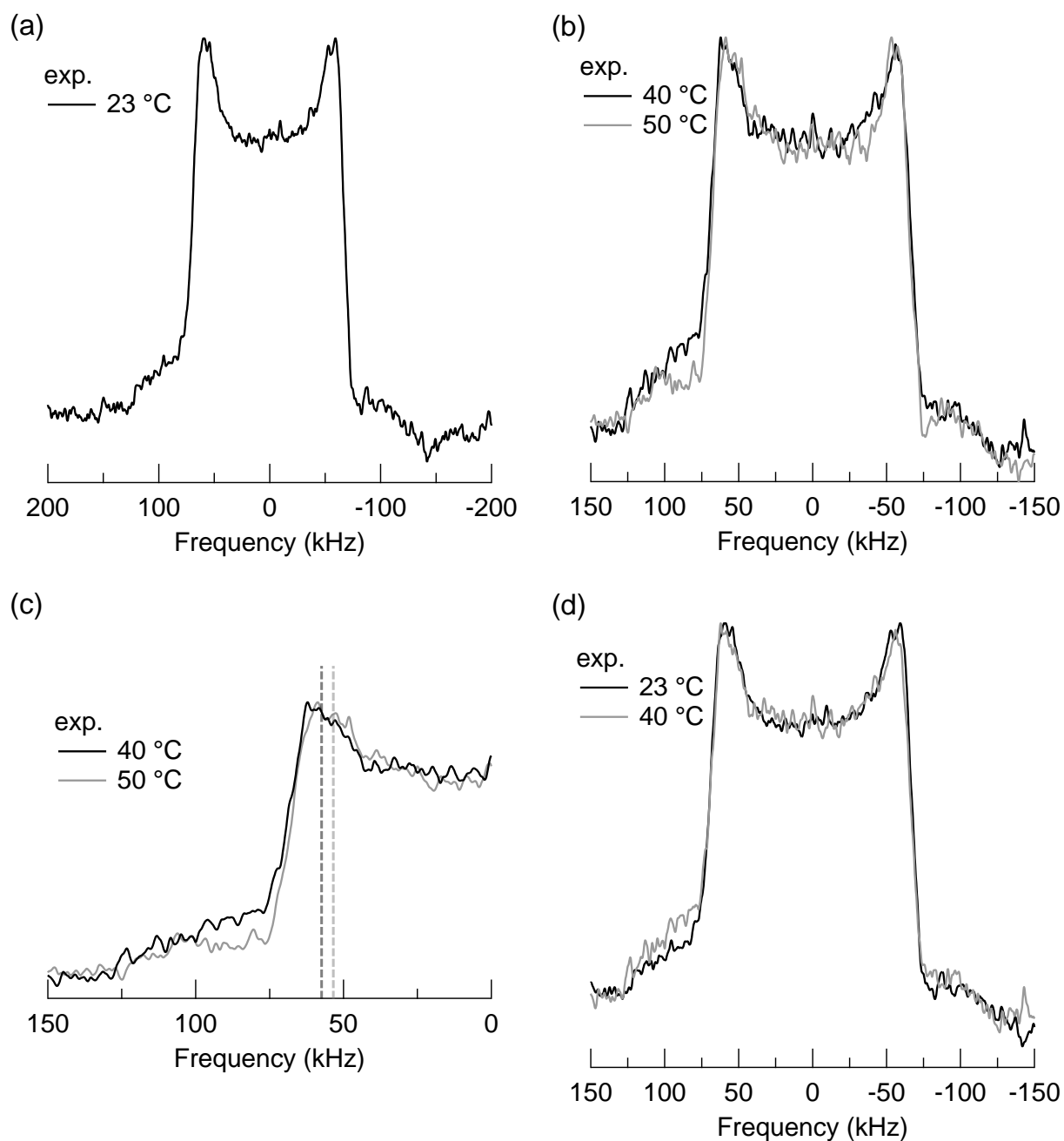


Figure 4-8. Temperature dependence of ^2H NMR wide-line spectra for $2\text{-}d_3$. (a) Whole spectra at 23 °C. (b) The spectra at 40 °C (black line) overlapped by that at 50 °C (gray lines). (c) Enlarged spectra at 40 (black line) and 50 °C (gray line). (d) Whole spectra at 23 °C (black line) overlapped by that at 40 °C (gray lines). Dark and light gray dashed lines in (c) show the peak positions at 40 and 50 °C, respectively.

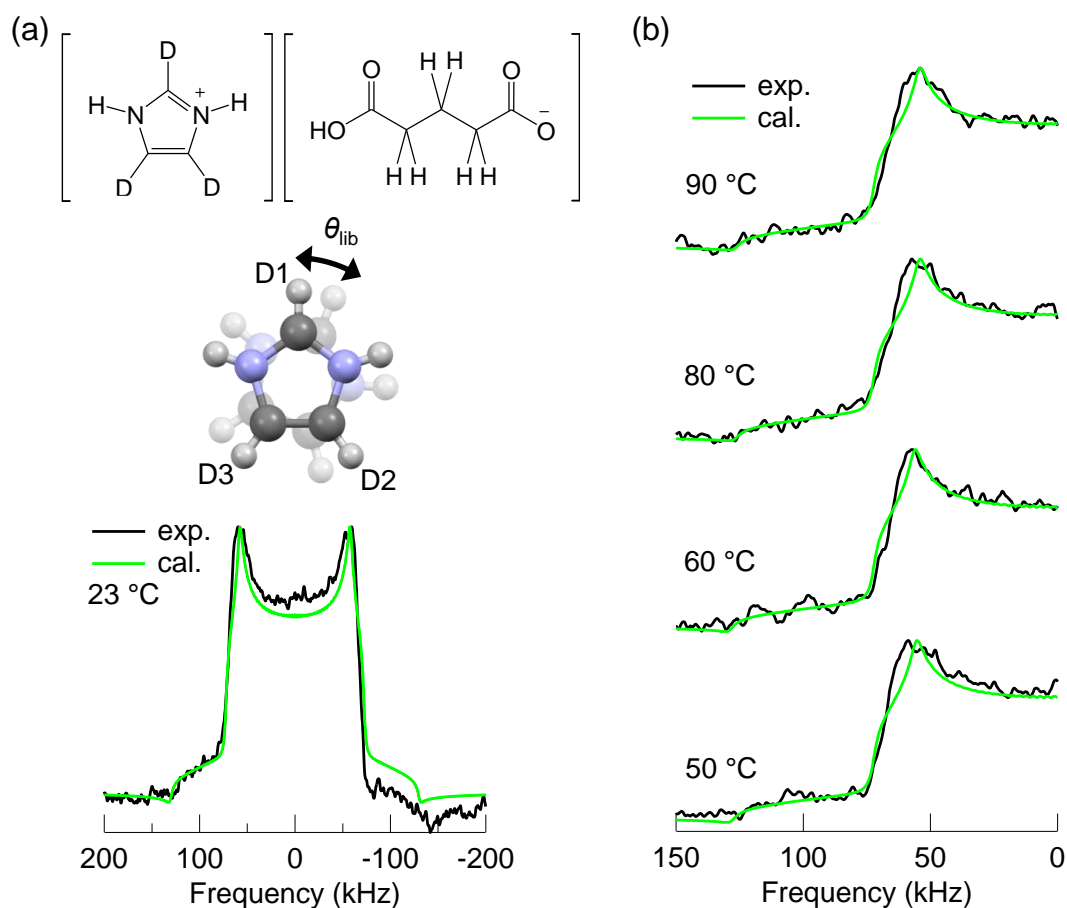


Figure 4-9. Results of the analyses of 2H NMR wide-line spectra for **2- d_3** . (a) (upper) The chemical structure of the imidazolium- d_3 hydrogen glutarate, (middle) schematic image of two-site jump model assuming the libration of imidazolium- d_3 molecule,³⁾ and (lower) whole spectra at 23 °C. (b) Enlarged spectra at several temperatures. Green lines show the simulation of single-component wide-line spectra using the two-site jump model with several values of libration rates k_{lib} and angles θ_{lib} (Table 4-7). Fixed values of $e^2qQ/\hbar = 174$ kHz and $\eta = 0.11$ determined by the simulation for the spectrum at 23 °C were used for the simulation at higher temperatures.

Table 4-7. The angles θ_{lib} and rates k_{lib} of the libration of imidazolium- d_3 cations in **2- d_3** at several temperatures.

Temperature (°C)	25	40	50	60	70	80	85	90
k_{lib} (Hz)	$\leq 10^0$	$\leq 10^0$	$\geq 10^9$	$\geq 10^9$	$\geq 10^9$	$\geq 10^9$	$\geq 10^9$	$\geq 10^9$
θ_{lib} (°)	0	0	13	11	15	16	15	16

The ^2H QCPMG spectra for **2**- d_3 are shown in Figure 4-10. Unlike **1**- d_3 ,³⁾ the spectra showed no significant changes in the operation temperature, indicating the 180° -flip motion [see Figure 4-1(b) in Section 4.1] is not significantly activated within the measurement temperature range. One of the reasons for the no activation of the 180° -flip motion is presumably the short distances between the neighboring H-bond network layers in **2**. In the crystal structure of **2**, the shortest $\text{N}\cdots\text{O}$ distance between the networks is 3.41 Å at 25 °C increasing to 3.46 Å at 90 °C. This inter-network $\text{N}\cdots\text{O}$ distance is shorter than that of **1** (3.51 Å at 23 and 103 °C), in which 180° -flip motion was observed in the proton-conducting temperature.³⁾

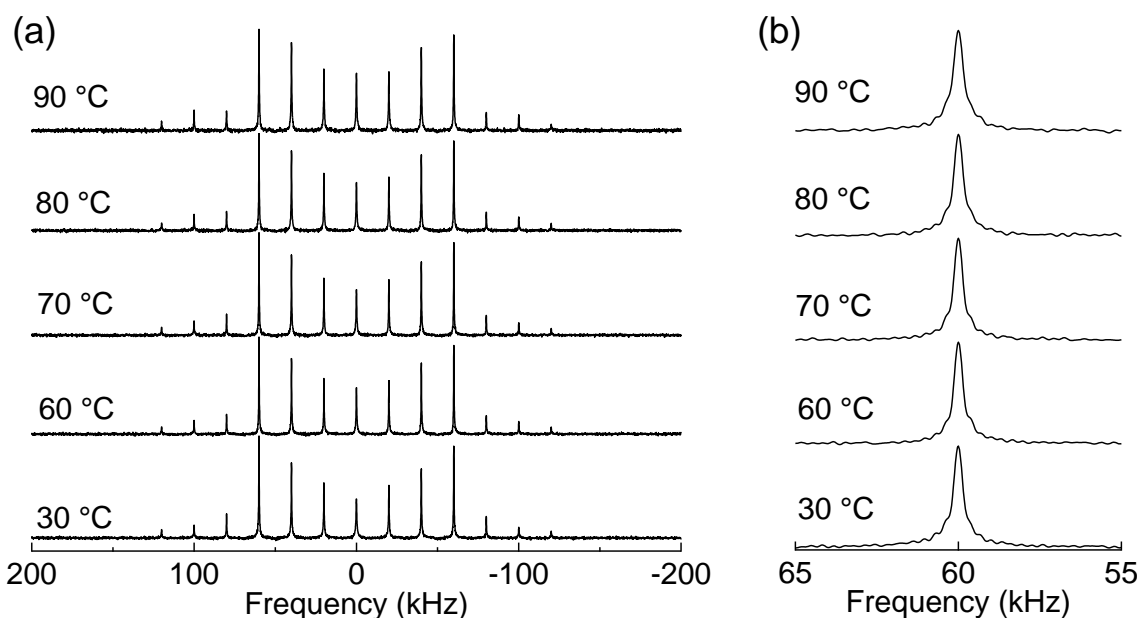


Figure 4-10. Temperature dependence of the ^2H NMR QCPMG spectra for **2**- d_3 at several temperatures. (a) Whole spectra and (b) enlarged spectra of (a).

The obtained wide-line ^2H spectra for **3**- d_3 showed the Pake doublet shape⁹⁾ [*e.g.*, Figure 4-11(a)], like **2**- d_3 . With elevating temperature from 26 °C to 130 °C, two peaks of the doublet become closer to each other [Figure 4-11(b) – (d)], which indicates the activation or increase of the libration motion between 26 and 130 °C (see Section 4.2). The analyses for the wide-line spectra [pink lines in Figure 4-12(a) and (b)] indicated that imidazolium cation exhibits the

libration with a significant magnitude ($k_{\text{lib}} = 10^4$ Hz, $\theta_{\text{lib}} = 5^\circ$) even at 26 °C (Table 4-8). The values of k_{lib} and θ_{lib} increase to 10^6 Hz and 8° at 90 °C even below the proton-conducting temperature (104 – 133 °C). In the proton-conducting temperature, $k_{\text{lib}} = 10^6$ Hz and $\theta_{\text{lib}} = 11^\circ$ at 110 °C further increase to 10^7 Hz and 13° at 130 °C.

On the other hand, the 180° -flip motion is not significantly activated in the proton-conducting temperature, indicated by no significant changes in the measured QCPMG spectra (Figure 4-13). The molecular orientation sticking out from the 2D H-bond network and the relatively short C \cdots O contacts 3.19 Å between the networks [see Figure 3-4(b) in Section 3.3.1] are likely to prevent the activation of the 180° -flip motion.

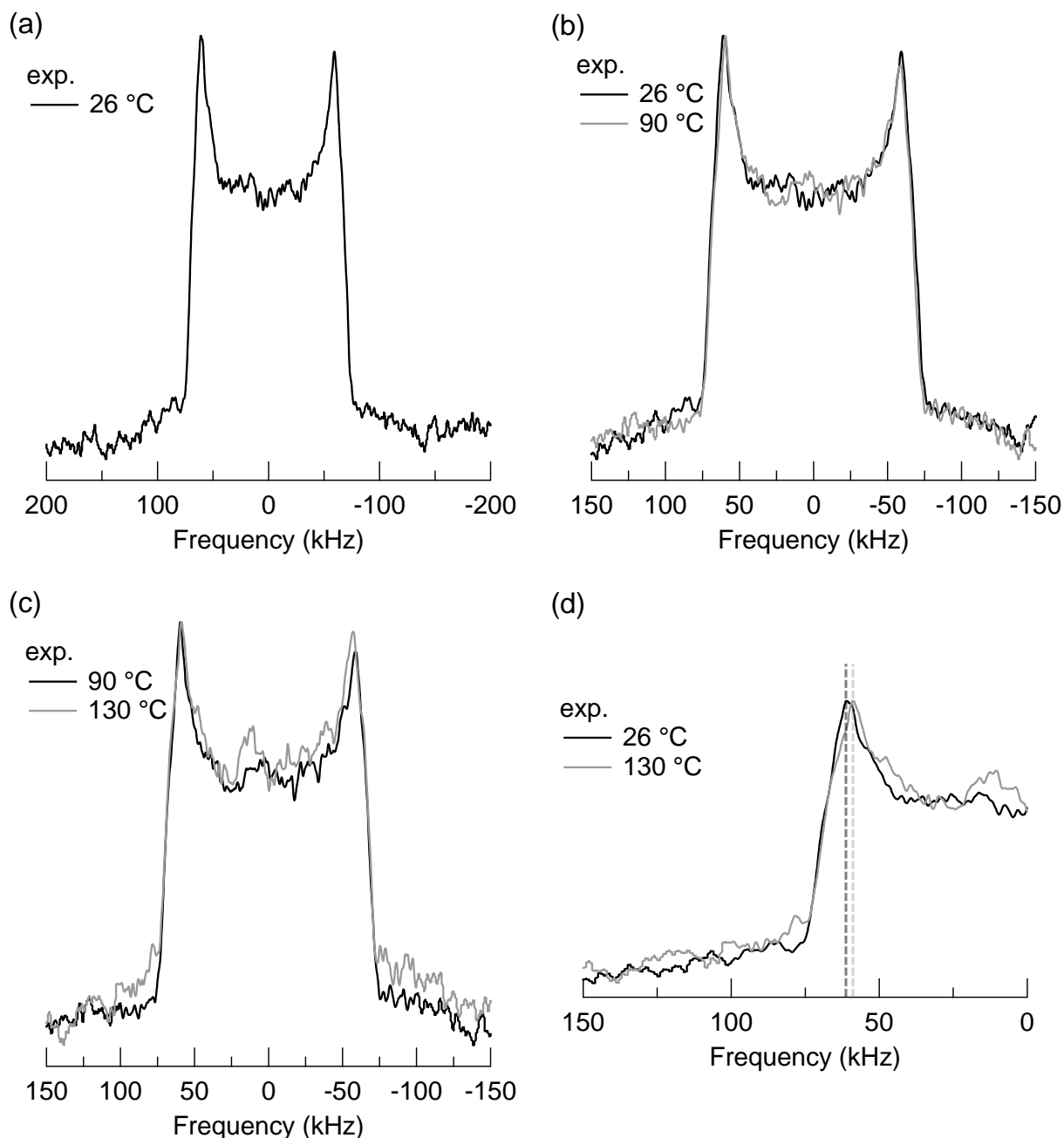


Figure 4-11. Temperature dependence of ^2H NMR wide-line spectra for $3\text{-}d_3$. (a) Whole spectra at 26 °C. (b, c) The spectra at (b) 26 °C or (c) 90 °C (black lines) overlapped by that at (b) 90 °C or (c) 130 °C (gray lines), respectively. (d) Enlarged spectra at 26 (black line) overlapped by that at 130 °C (gray line). Dark and light gray dashed lines in (d) show the peak positions at 26 and 130 °C, respectively. The change of the peak position, corresponding to the change of the magnitude of libration motion, for $3\text{-}d_3$ is smaller than that for $2\text{-}d_3$ [see Figure 4-8(c)].

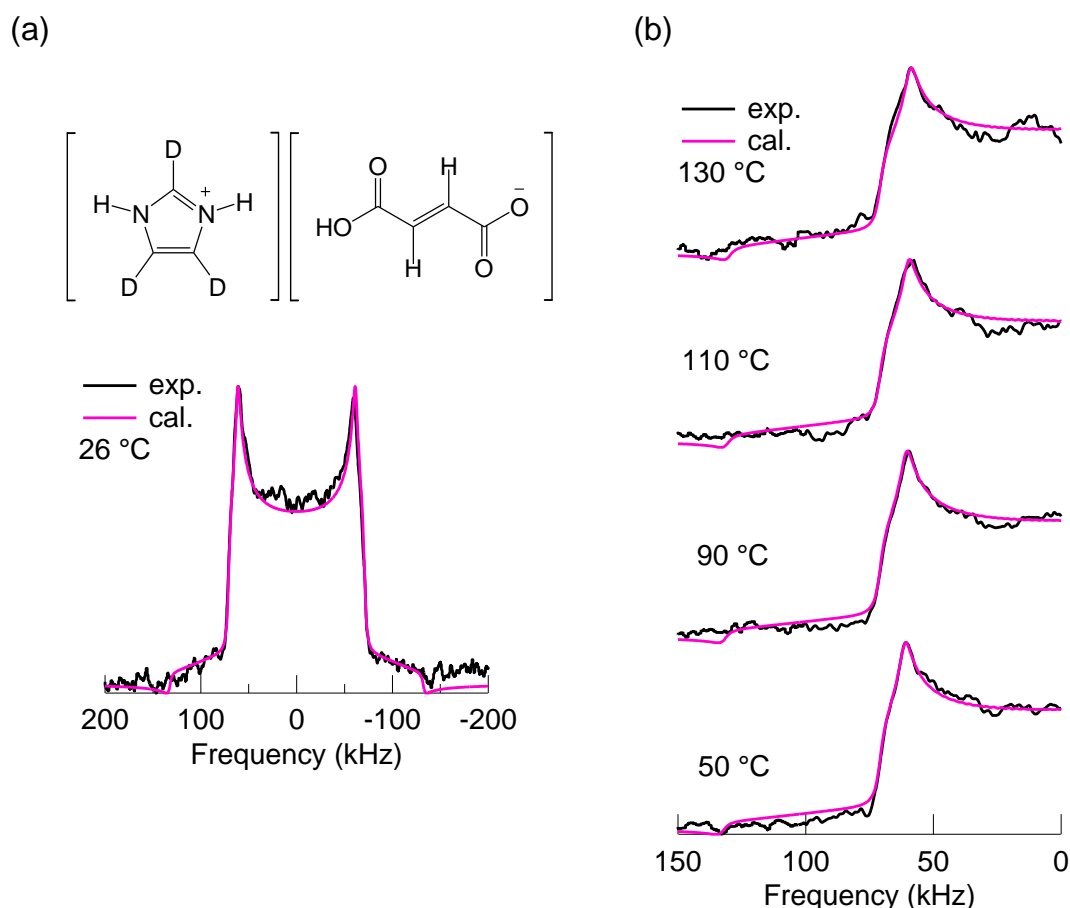


Figure 4-12. Results of the analyses of ^2H NMR wide-line spectra for **3- d_3** . (a) (upper) The chemical structure of the imidazolium- d_3 hydrogen fumarate and (lower) whole spectra at 26 °C. (b) Enlarged spectra at several temperatures. Pink lines show the simulation of single-component wide-line spectra using the two-site jump model with several values of libration rates k_{lib} and angles θ_{lib} (Table 4-8). Fixed values of $e^2qQ/\hbar = 177$ kHz and $\eta = 0.07$ determined in the simulation for the spectrum at 26 °C were used for the simulation at higher temperatures.

Table 4-8. Angles θ_{lib} and rates k_{lib} of the libration of imidazolium cations in **3- d_3** at several temperatures.

Temperature (°C)	26	50	70	90	110	120	130
k_{lib} (Hz)	10^4	10^6	10^6	10^6	10^7	10^7	10^7
θ_{lib} (°)	5	5	7	8	11	13	13

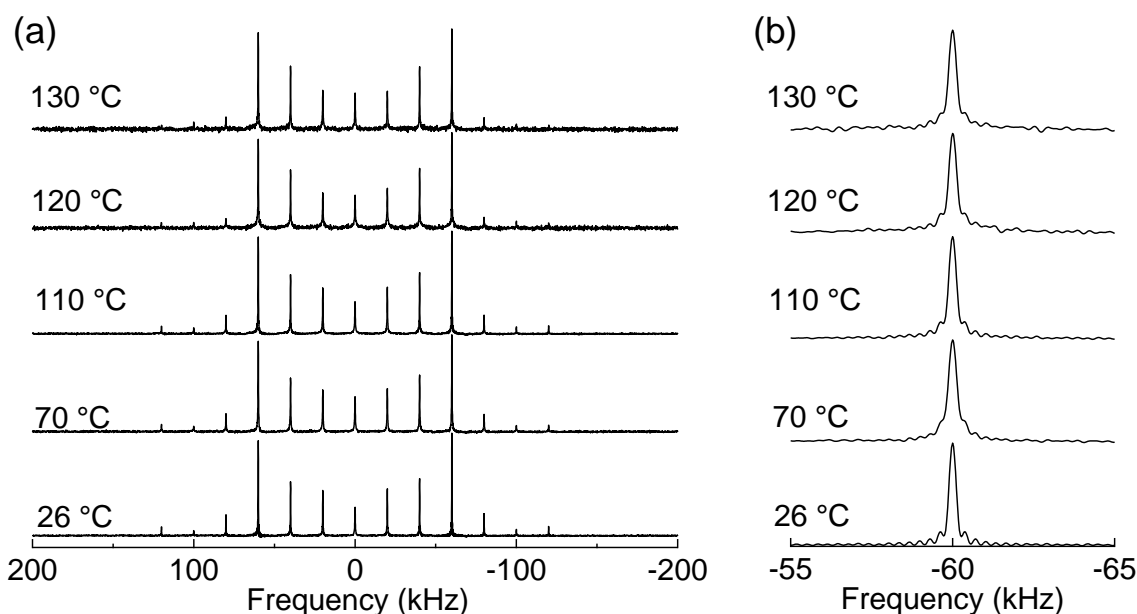


Figure 4-13. Temperature dependence of the ^2H NMR QCPMG spectra for $3\text{-}d_3$ at several temperatures. (a) Whole spectra and (b) enlarged spectra of (a).

For **1**, **2**, and **3**, the temperature dependence of libration angles θ_{lib} and proton conductivities σ are compared as shown in Figure 4-14. Magnitude of θ_{lib} is **2** (green diamonds in lower graph) $>$ **1** (orange circles)³⁾ $>$ **3** (pink squares), in consistent with the same relationship of σ [orange circles (**1**), green diamonds (**2**), and pink squares (**3**) in upper graph]. The similarity of these relationships suggests that the larger θ_{lib} , that is, the larger libration motion of imidazolium cations make σ higher in the salts. Therefore, the author concludes that the libration motion of the imidazolium cations promotes proton conduction in these imidazolium hydrogen dicarboxylates.

However, the temperature dependence of θ_{lib} cannot provide a convincing explanation for that of σ . In fact, θ_{lib} in **2** showed only a small increase in the proton-conducting temperature in contrast to the strong increase in **1**, although σ of **2** showed the non-linear dependence on the reciprocal temperature like **1**. From these correlations between anhydrous proton conductivities and the θ_{lib} , the author considers that the promotions of proton conduction with elevated temperature are not realized just by the libration motion of imidazolium cations.

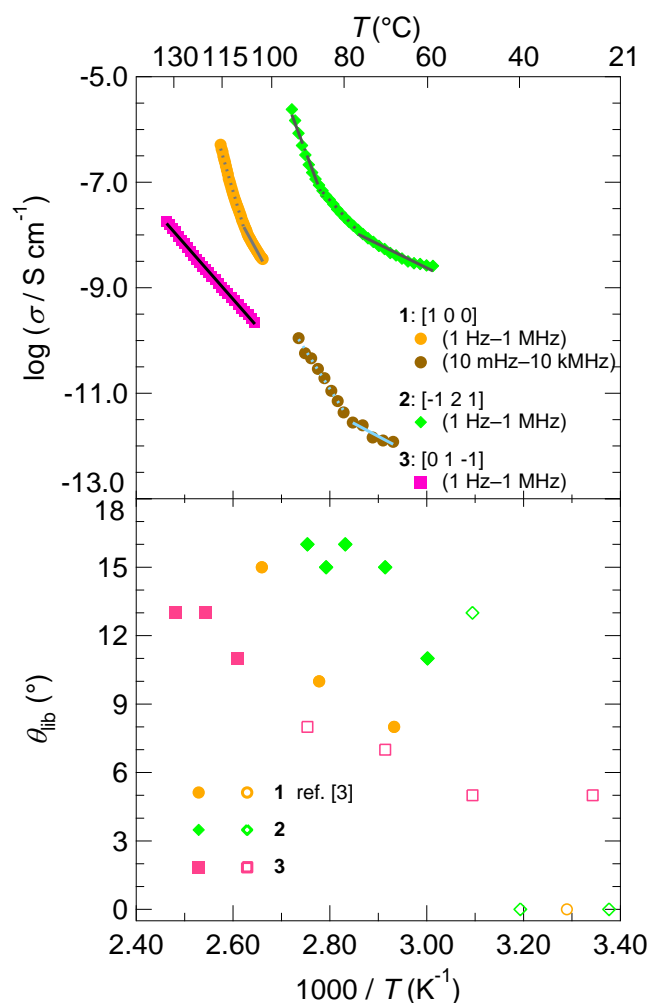


Figure 4-14. (upper) The single-crystal proton conductivity (σ) and (lower) libration angle θ_{lib} vs. $1000/T$ plots for **1** [orange (1 Hz – 1 MHz) and dark orange (1 Hz – 1 MHz) circles], **2** [green diamonds (1 Hz – 1 MHz)], and **3** [pink squares (1 Hz – 1 MHz)]. In upper graph, the fitting lines for σ along the $[1\ 0\ 0]$ directions in **1** are denoted in gray (1 Hz – 1 MHz) (solid line, 103 – 108 $^{\circ}\text{C}$; dashed line, 108 – 115 $^{\circ}\text{C}$), light blue lines (10 mHz – 10 kHz) (solid line, 68 – 78 $^{\circ}\text{C}$; dashed line, 80 – 92 $^{\circ}\text{C}$), respectively. The fitting lines for σ along the $[-1\ 2\ 1]$ directions in **2**, and the $[0\ 1\ -1]$ directions in **3** are denoted in dark gray and black lines (**2**: solid line, 59 – 77 $^{\circ}\text{C}$; dashed line, 77 – 86 $^{\circ}\text{C}$; dashed-dotted line, 86 – 94 $^{\circ}\text{C}$; **3**: solid lines, 105 – 133 $^{\circ}\text{C}$), respectively. In lower graph, the filled circles, diamonds, and squares denote libration angles in the proton-conducting temperature ranges of **1** (orange), **2** (green), and **3** (pink). The open circles, diamonds, and squares denote libration angles below the proton-conducting temperature ranges.

4.3.3. Effects of molecular dynamics on proton conduction from viewpoint of molecular arrangements

Finally, the author discusses how the libration of imidazolium cations contributes to the proton conduction in the materials, by considering the structural changes in H-bond manners accompanied with the libration. As mentioned above, in **1**, the orientational disorder corresponding to the libration of imidazolium cation was observed at the proton-conducting temperature [Figure 4-4(c) in Section 4.3.1]. Because the molecular orientation of imidazolium cation is parallel to the network [dihedral angle of 2.6° : Figure 4-15(a)], the direction of the libration motion [blue arrows in Figure 4-15(b)] is along the H-bond network, that is, along the possible proton conducting path for the $[1\ 0\ 0]$ direction (orange belt). Thus, it is indicated that the libration motion promotes the proton transfer in the H-bond network, especially in the $[1\ 0\ 0]$ direction.

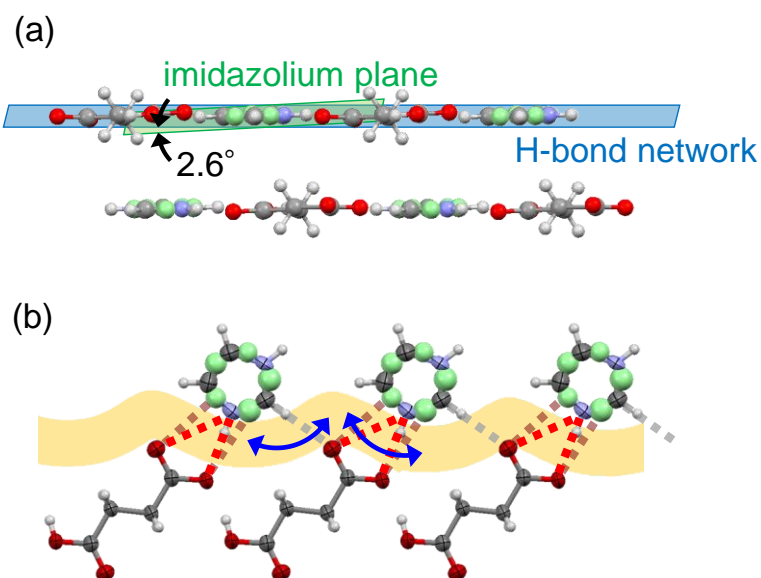


Figure 4-15. (a) Stacking arrangement of the 2D H-bond networks and dihedral angle between the 2D H-bond network and imidazolium plane in the high- T structure of **1** (blue and green planes: plane orientations of the H-bond network and the imidazolium five-membered ring). (b) Molecular arrangements along the $[1\ 0\ 0]$ direction in the high- T structure of **1**. In (b), the orange belt represents the possible proton conducting path. Red dashed lines, brown dashed lines, gray dashed lines, and blue arrows denote N-H \cdots O H-bonds, disordered atom \cdots O contacts, C-H \cdots O contacts, and direction of the libration motion.

In **2**, the libration with the angle $\theta_{\text{lib}} = 16^\circ$ has the potential to form additional N-H \cdots O H-bonds with $d_{\text{NO}} \sim 3.0$ Å calculated geometrically [brown dashed lines in Figure 4-16(a)]. As the case of **1**, the motional direction of the libration (blue arrows) overlaps the possible proton conducting path along the $[1\ 2\ 1]$ direction (green belt), owing to the molecular orientation of imidazolium cation parallel to the network [dihedral angle of $3.2 - 6.6^\circ$: Figure 4-16(b)]. Therefore, libration motion, accompanying the increase of the number of possible H-bonds, presumably contributes to promotion of the proton transfer in the $[1\ 2\ 1]$ direction. On the other hand, the small temperature variation of θ_{lib} in **3** and the imidazolium orientation sticking out from the H-bond network plane [dihedral angle of 77° : Figure 4-17(a)] make the promotion of proton conduction by the libration small. Furthermore, the values of θ_{lib} in **3** (pink squares in

lower graph of Figure 4-14) were relatively small compared to those in **2** (green diamonds), which makes the formation of additional H-bonds difficult. The distances between nitrogen atoms shifted by the libration with $\theta_{\text{lib}} = 13^\circ$ and oxygen atoms of neighboring fumarate anions were calculated geometrically; the calculated d_{NO} are about 3.5 and 3.6 Å [black and orange arrows in Figure 4-17(b)] which are much longer than the sum of van der Waals radii of N and O atoms (3.07 Å).¹⁵⁾ Thus, the imidazolium plane out of the H-bond network and the relatively small θ_{lib} suggest that the libration motion in **3** is less likely to promote the proton conduction, which is consistent with the linear behavior of the conductivity.

Based on the comparison between σ , θ_{lib} , and crystal structures, the molecular arrangements in the H-bond networks are considered to affect the degrees of contributions from molecular dynamics as discussed above. Therefore, the author concludes that, although the molecular dynamics is considered to be one of the key factors, only the presence of molecular dynamics is not enough for promotion of the proton conduction; both of the “static” factors, H-bond network structures and molecular arrangements, and the “dynamics” of constituent molecules synergistically contribute to the anhydrous proton conductivity.

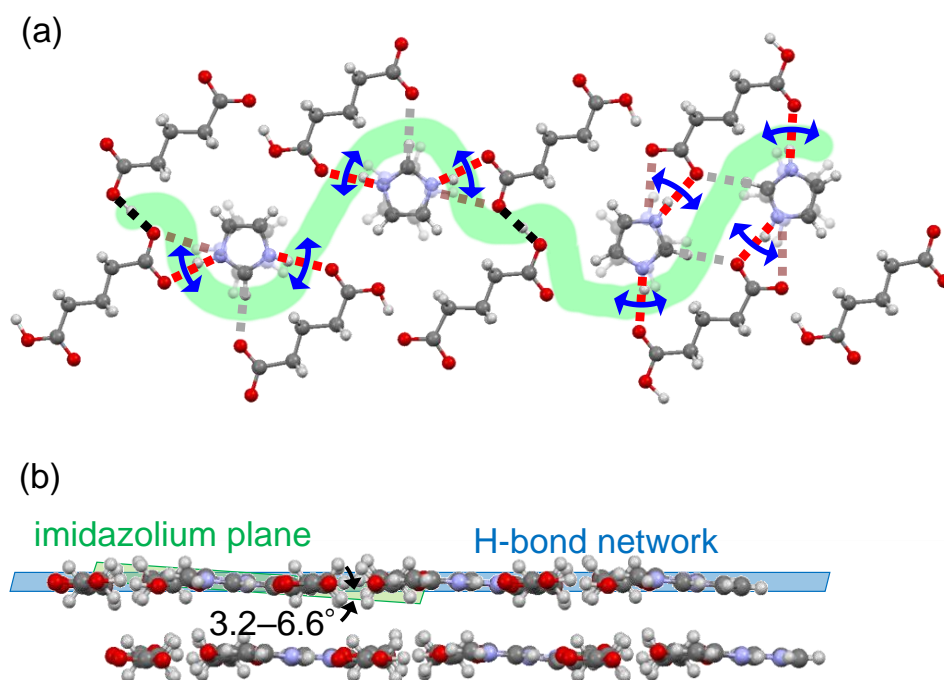


Figure 4-16. (a) Molecular arrangements along the $[-1\ 2\ 1]$ direction in **2** (green belt: the possible proton conducting path, red dashed lines: N-H \cdots O H-bonds, brown dashed lines: possible additional N-H \cdots O H-bonds, gray dashed lines: C-H \cdots O contacts black dashed lines: O-H \cdots O H-bonds, blue arrows: direction of the libration motion with $\theta_{\text{lib}} = 16^\circ$). (b) Stacking arrangement of the 2D H-bond networks and dihedral angle between the 2D H-bond network and imidazolium plane in **2**. Blue and green planes in (b) represent plane orientations of the H-bond network and the imidazolium five-membered ring.

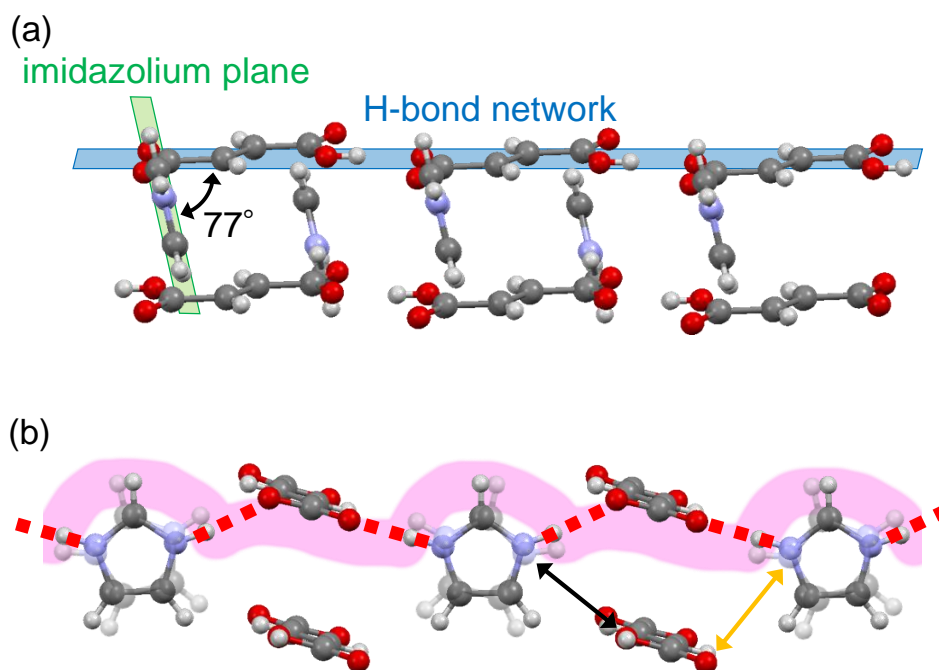


Figure 4-17. (a) Stacking arrangement of the 2D H-bond networks and dihedral angle between the 2D H-bond network and imidazolium plane in **3**. (b) Molecular arrangements along the $[0\ 1\ -1]$ direction in **3** (pink belt: the possible proton conducting path, red dashed lines: $\text{N-H}\cdots\text{O}$ H-bonds, black and orange arrows: two types of $\text{N}\cdots\text{O}$ distances accompanied by the libration with $\theta_{\text{lib}} = 13^\circ$). Blue and green planes in (a) represent plane orientations of the H-bond network and the imidazolium five-membered ring.

For **1**, **2**, and **3**, however, only libration motion of imidazolium cations does not fully describe all conducting processes in the proton conduction paths, in addition to the temperature dependences of proton conductivity. One example of the undescribed processes is the portions of the green belt not overlapped by the blue arrows in Figure 4-16(a). The author considers that such proton transfer processes occur involving much slower dynamics which could not be detected by neither X-ray diffraction nor solid-state NMR. The difference in H-bond network structure and/or such slower molecular dynamics have the potential to contribute the significant increases of proton conductivity with elevated temperature. Investigations of dynamics of acid molecules and/or slow dynamics ($k < 10^3$ Hz) are required to get further understanding of the

anhydrous proton conduction.

4.4. Conclusion

The molecular dynamics of the imidazolium cations and its effects were investigated by the high- T single-crystal X-ray structure analyses and the solid-state ^2H NMR spectroscopies. **1** showed the structural phase transition with the change of stacking arrangement of the 2D H-bond networks at 80 °C. In the crystal structure at 103 °C, imidazolium cations in **1** showed the orientational disorder, indicating the libration motion of imidazolium cations is activated above around 80 °C. Consistently, the σ obtained from the impedance measurements for 10 mHz – 10 kHz showed the significant increase and the high activation energy similar to imidazole single crystal¹²⁾ in the temperature region around 80 °C, which indicates the proton conduction is promoted with the activation of the libration. From the results of the solid-state ^2H NMR spectroscopies, the relationship of libration angle θ_{lib} is consistent with the same relationship of σ (both showed **2** > **1** > **3**), which suggests that the larger libration motion promotes more strongly the proton conduction in the salts. However, the temperature dependence of the θ_{lib} cannot fully explain that of the σ . In fact, the θ_{lib} in **2** showed only the small increase in the proton-conducting temperature in contrast to the strong increase in **1**, while the σ of **2** showed the non-linear dependence on the reciprocal temperature like **1**. The author considers that the promotions of proton conduction with elevated temperature are not realized just by the libration motion of imidazolium cations.

Based on the molecular orientations in the crystal structures, the motional planes of the libration in **1** and **2** are almost parallel to the H-bond network planes, while the libration plane in **3** is out of the network. Therefore, the libration motion in **1** and **2** is considered to promote the proton transfer more effectively than that in **3**. This indicates the enhancement of the libration motion parallel to the H-bond network potentially contributes to the promotion of anhydrous proton conduction in the imidazolium hydrogen dicarboxylates.

These results demonstrate that both of the H-bond network structures and the dynamics of organic molecules synergistically play important roles in the anhydrous proton conduction. This is thought as peculiar nature of the Grotthuss-type conduction in anhydrous solids, as believed also in the inorganic oxo-acid salts.²⁾ The present results offer crucial insights into conduction mechanism and novel material design of the anhydrous proton conductors.

On the other hand, in order to search for the causes of the unique temperature dependence of proton conductivity and trace the residual processes in the proton conduction paths in the three salts (**1** – **3**) to obtain full picture of the proton conduction, molecular motions of acid molecules and slow dynamics ($k < 10^3$ Hz) are currently under investigation, in terms of the structural and potential energy changes accompanied with the molecular dynamics studied by using infrared spectroscopies and theoretical calculations.

4.5. Reference

- 1) (a) C. J. D. van Grotthuss, Ann. Chim., **58**, 54 (1806). (b) N. Agmon, Chem. Phys. Lett. **244**, 456 (1995).
- 2) (a) A. I. Baranov, B. V. Merinov, A. V Tregubchenko, V. P. Khiznichenko, L. A. Shuvalov, and N. M. Schagina, Solid State Ionics **36**, 279 (1989). (b) W. Münch, K. D. Kreuer, U. Traub, and J. Maier, Solid State Ionics **77**, 10 (1995). (c) S. M. Haile, C. R. I. Chisholm, K. Sasaki, D. A. Boysen, and T. Uda, Faraday Discuss. **134**, 17 (2007). (d) G. Kim, F. Blanc, Yan-Yan Hu, and C. P. Grey, J. Phys. Chem. C **117**, 6504 (2013).
- 3) T. Umiyama, R. Ohashi, T. Ida, and M. Mizuno, Chem. Lett. **42**, 1323 (2013).
- 4) K. Pogorzelec-Glaser, J. Garbarczyk, Cz. Pawlaczyk, and E. Markiewicz, Mater. Sci.-Pol. **24**, 245 (2006).
- 5) J. C. MacDonald, P. C. Dorrestein, and M. M. Pilley, Cryst. Growth Des. **1**, 29 (2001).
- 6) F. H. Larsen, H. J. Jakobsen, P. D. Ellis, and N. C. Nielsen, Chem. Phys. Lett. **292**, 467 (1998).
- 7) (a) T. Araya, A. Niwa, M. Mizuno, and K. Endo, Chem. Phys. **344**, 291 (2008). (b) M. Mizuno, A. Iwasaki, T. Umiyama, R. Ohhashi, and T. Ida, Macromolecules **47**, 4769 (2014). (c) M. Mizuno, M. Chizuwa, T. Umiyama, Y. Kumagai, T. Miyatou, R. Ohashi, T. Ida, M. Tansho, and T. Shimizu, Hyperfine Interact. **230**, 95 (2015).
- 8) M. E. Rose: *Elementary Theory of Angular Momentum*, John Wiley & Sons, Ltd., New York, U.S.A., 1957.
- 9) (a) G. E. Pake, J. Chem. Phys. **16**, 327 (1948). (b) M. Mehring: *Principles of High Resolution NMR in Solids*, Springer-Verlag Berlin Heidelberg, New York, U.S.A., 1983. (c) B. Blümich, B. Blümmler, B. F. Chmelka, G. Fleischer, F. Fujara, A.-R. Grimmer, F. Lauprêtre, and D. Rftery: *Solid-State NMR I Methods*, Springer-Verlag Berlin Heidelberg, New York, U.S.A., 1994.
- 10) K. Pogorzelec-Glaser, Cz. Pawlaczyk, A. Pietraszko, and E. Markiewicz, J. Power Sources

- 173**, 800 (2007).
- 11) (a) K. Pogorzelec-Glaser, A. Rachocki, P. Ławniczak, A. Pietraszko, Cz. Pawlaczyk, B. Hilczer, and M. Pugaczowa-Michalska, *CrystEngComm* **15**, 1950 (2013). (b) A. Rachocki, K. Pogorzelec-Glaser, P. Ławniczak, M. Pugaczowa-Michalska, A. Łapiński, B. Hilczer, M. Matczak, and A. Pietraszko, *Cryst. Growth Des.* **14**, 1211 (2014).
- 12) A. Kawada, A. R. McGhie, and M. M. Labes, *J. Chem. Phys.* **52**, 3121 (1970).
- 13) (a) de N. D. Marcia Cordes, and J. L. Walter C. S. C., *Spectrochim. Acta A, Mol. Biomol. Spectrosc.* **24**, 237 (1968). (b) SDBSWeb: <https://sdb.sdb.aist.go.jp> (National Institute of Advanced Industrial Science and Technology, December 23, 2019).
- 14) F. H. Larsen, H. J. Jakobsen, P. D. Ellis, and N. C. Nielsen, *Chem. Phys. Lett.* **292**, 467 (1998).
- 15) A. Bondi, *J. Phys. Chem.* **68**, 441 (1964).

Chapter 5.

General Conclusion

In this thesis, the author systematically investigated anhydrous proton conductivities of purely organic proton conductors, imidazolium hydrogen dicarboxylates, by using high-quality single crystals to elucidate the origins and mechanisms of the anhydrous proton conductivity. The author succeeded in growing high-quality single crystals with sufficient size for the single-crystal impedance measurements. By using the obtained high-quality single crystals, the intrinsic proton conductivity and its relationship with “static” factors of the molecular arrangements and the proton donating abilities of the constituent molecules in imidazolium hydrogen succinate (**1**), glutarate (**2**), and fumarate (**3**) were revealed for the first time. In addition, the effects of “dynamics” of the constituent molecules on the anhydrous proton conductivity were revealed based on the relationship between the conductivity, molecular arrangements, and dynamics of the organic constituents. Here the author summarizes the obtained results into the following paragraphs discussed in the preceding chapters in this thesis.

In Chapter 2, the intrinsic proton conductivity without contributions of grain boundaries in **1** was revealed by the single-crystal ac impedance measurements. The comparison between the proton conductivity σ of the single-crystalline sample and that of the compressed powder (pellet) samples indicated that the σ of the single crystals shows the “intrinsic” conductivity while that of the pellets contains the extrinsic contributions from grain boundaries. In addition, the anisotropy of the proton conductivity demonstrated the importance of the “static” factors, that is, the 2D H-bond network structure and the H-bonds between the base (imidazole) and acid (succinate) molecules in the anhydrous proton conduction.

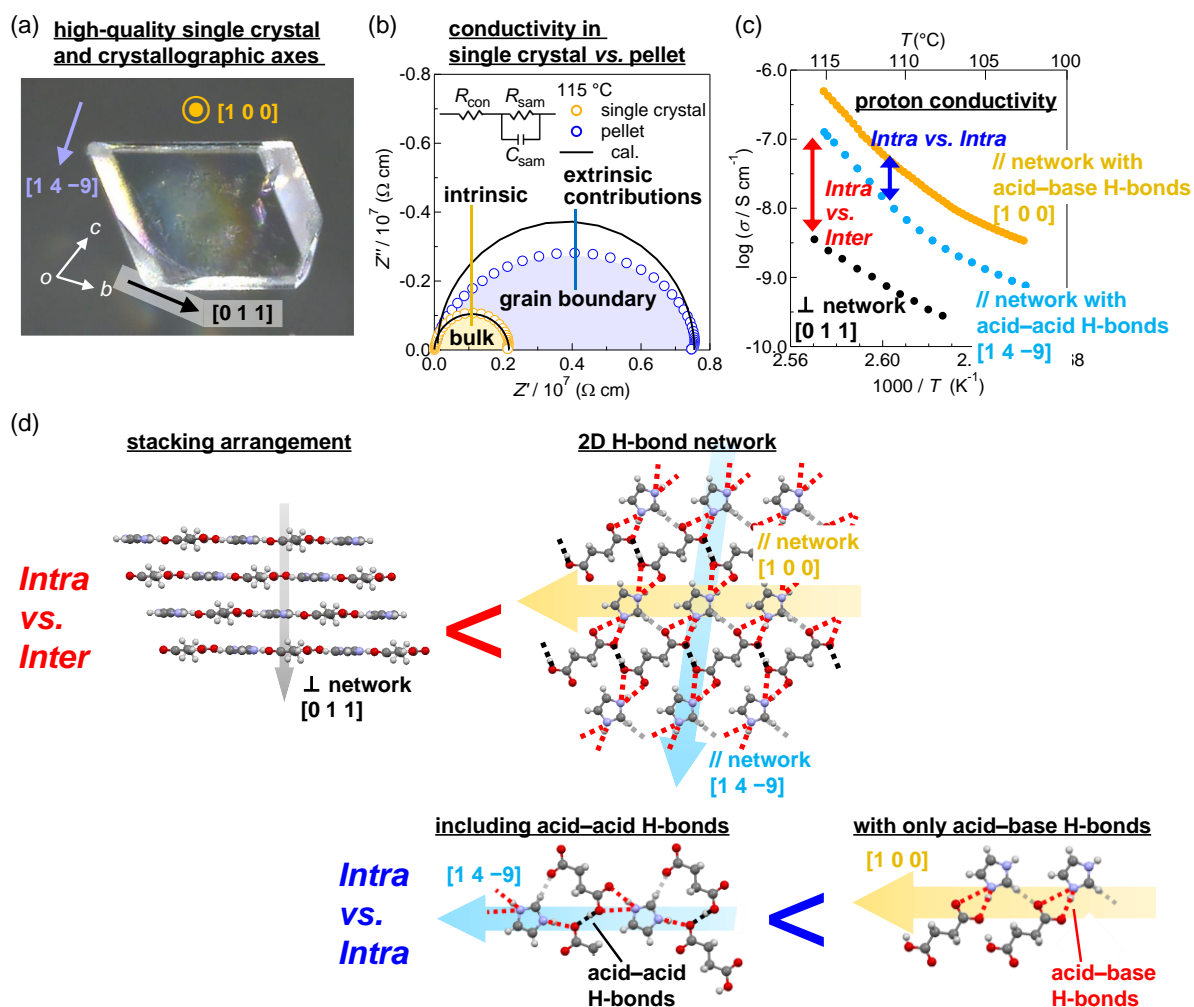


Figure 5-1. (a) A photograph of a high-quality single crystal of imidazolium hydrogen succinate (**1**). (b) Cole-Cole plots measured for a single crystal and a pellet of **1** at 115 °C. (c) Arrhenius plots of the proton conductivity (σ) for the single crystal of **1** measured along the parallel directions (orange and blue circles) and the perpendicular direction (black circles) to the H-bond network. (d) Schematic images of anisotropy of σ between (upper) parallel (orange and blue arrows) and perpendicular (black arrow) directions to the 2D H-bond network, and between (lower) parallel directions with only acid-base H-bonds (orange arrow) and with not only acid-base but also acid-acid H-bonds (blue arrow).

In Chapter 3, the effects of proton donating abilities (pK_a) of the constituent molecules as another “static” factor related to molecular properties were discussed based on the comparison of the σ within the H-bond network structures among **1**, **2**, and **3**. The author revealed that the

proton conductivity is higher when the difference of pK_a (ΔpK_a) between the dicarboxylic and imidazolium conjugate acids is smaller, which indicates that the smaller ΔpK_a makes the barrier of proton transfer between the acid and base lower. Therefore, small ΔpK_a between constituent acid and base molecules is turned to be one of the important “static” factors to achieve the anhydrous proton conductivity.

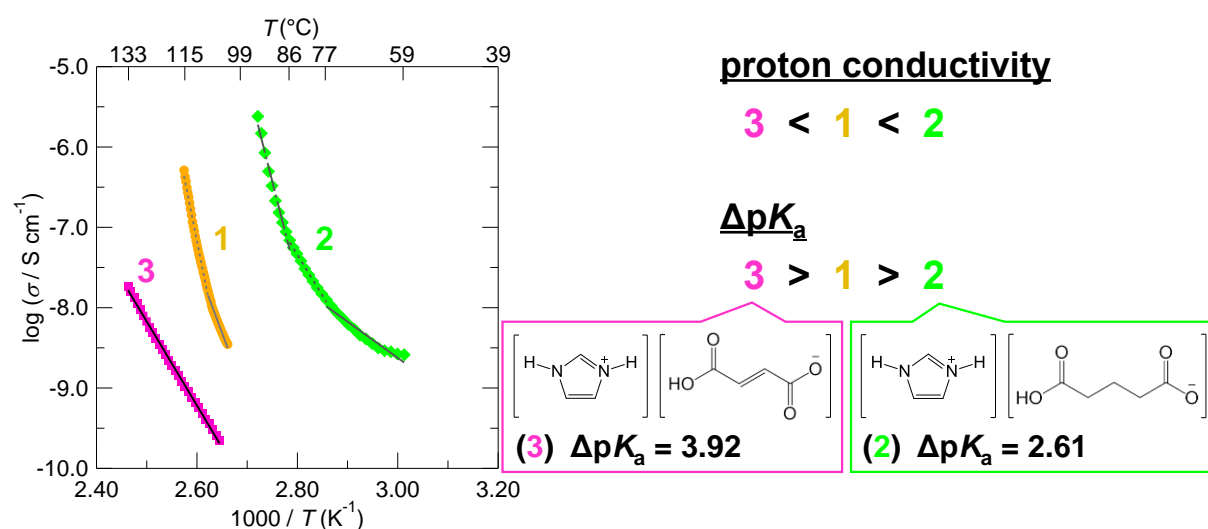


Figure 5-2. Arrhenius plots of the proton conductivity (σ) for single crystals of **1** (orange circles), imidazolium hydrogen glutarate (**2**) (green diamonds), and fumarate (**3**) (pink squares) measured within the 2D H-bond networks. The salt with the smaller ΔpK_a value showed the higher σ ; **2** with smallest ΔpK_a showed highest σ , while **3** with largest ΔpK_a showed lowest σ .

In Chapter 4, in addition to the “static” effects discussed in the preceding chapters, the effect of the molecular “dynamics” of imidazolium cations on the anhydrous proton conductivity were investigated by the high-temperature single-crystal X-ray structure analyses and the solid-state ^2H NMR spectroscopy. The high-temperature X-ray structure analysis revealed that **1** shows the structural phase transition at ca. 80 °C accompanied by the change of stacking arrangement of the H-bond network layers. In the crystal structure at 103 °C, the imidazolium cations show the orientational disorder in the molecular plane, which indicates that the promotion of the

proton conductivity around 80 °C observed by the low-frequency ac impedance measurements is related to the libration motion of imidazolium cations in **1**. Although the salts **2** and **3** did not show such structural transitions, solid-state ^2H NMR measurements by using the imidazolium- d_3 -substituted salts (**2- d_3** and **3- d_3**) revealed that they also show the libration motion in the proton-conducting temperatures like **1**. The order of libration angles (θ_{lib}) of imidazolium cations showed the same relationship with the σ within the 2D H-bond networks; the salt with the larger θ_{lib} shows the higher σ . In addition, the effects of the molecular motion on the proton conductivity are considered to be affected by the relationship between the motional direction and the molecular arrangements in the H-bond networks. These results demonstrate that the molecular dynamics of imidazolium cation promote the anhydrous proton conduction cooperatively with the H-bond network structures.

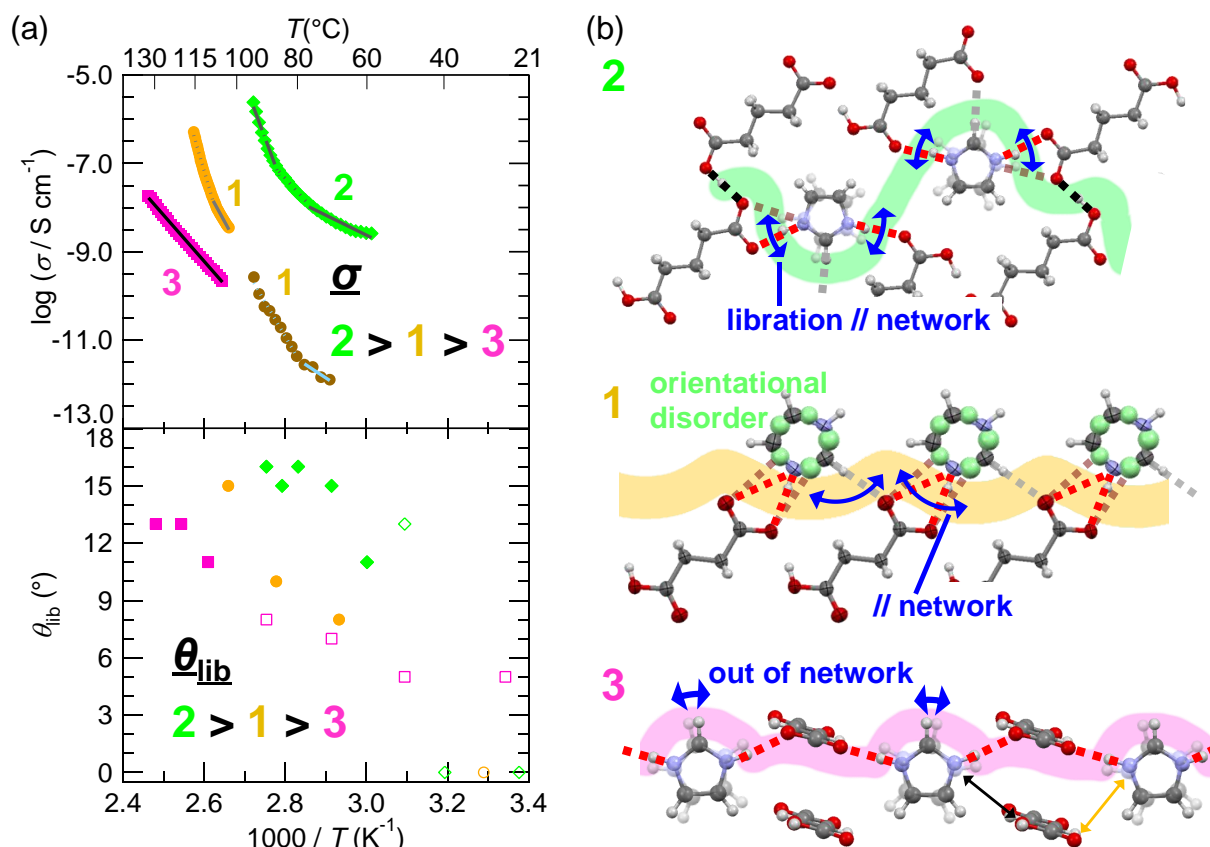


Figure 5-3. (a) (upper) The single-crystal proton conductivity (σ) and (lower) libration angle θ_{lib} vs. $1000/T$ plots for **1** (orange and dark orange circles), **2** (green diamonds), and **3** (pink squares). (b) Molecular arrangements along the possible proton conducting paths of (upper) **2**, (middle) **1**, and (lower) **3**. In the high temperature phase of **1** above 80°C , orientational disorder of imidazolium cation was observed, which is related to the libration motion of imidazolium cation. The larger θ_{lib} , *i.e.*, the larger libration motion, of imidazolium cation contributes the higher σ . The libration motion parallel to the H-bond networks in **1** and **2** is considered to promote the proton conduction more effectively than that out of the network in **3**.

As mentioned above, the important factors for the anhydrous proton conductivity of the imidazolium hydrogen dicarboxylates were revealed by the systematic study. The anisotropy of the proton conductivity related to arrangements and H-bond manners of the constituent molecules demonstrates the crucial roles of the H-bond network structures and H-bonds between the acid and base molecules in the anhydrous proton conduction. The small $\Delta\text{p}K_{\text{a}}$

between the constituent acid and conjugated acid of base molecules is turned to be a key factor for realizing the anhydrous proton conductivity. In addition, the libration motion of imidazolium cations promotes the proton transfer in the H-bond networks, which is affected by molecular arrangements in the networks. Therefore, the author concludes that both of the “static” factors (the H-bond network structures and the proton-donating abilities) and the “dynamics” of constituent organic molecules synergistically play important roles in the anhydrous proton conduction. This is thought as peculiar nature of the Grotthuss-type conduction in anhydrous solids.

The intrinsic proton conductivity and its relationship with the arrangements, properties, and dynamics of the constituent molecules in the anhydrous purely organic crystals had not been unraveled and thus the origins and mechanisms of the proton conduction had been unclear. The author believes that this thesis provides crucial insights into not only the mechanisms of the anhydrous proton conduction but also the material design principle for high performance anhydrous organic proton conductors.

List of Publications

[Related to this thesis]

1. Yoshiya Sunairi, Akira Ueda, Junya Yoshida, Keisuke Suzuki, and Hatsumi Mori, “Anisotropic Proton Conductivity Arising from Hydrogen-Bond Patterns in Anhydrous Organic Single Crystals, Imidazolium Carboxylates” J. Phys. Chem C, **122**, 11623 (2018).
2. Yoshiya Sunairi, Shun Dekura, Akira Ueda, Tomonori Ida, Motohiro Mizuno, and Hatsumi Mori, “Anhydrous Purely Organic Solid-State Proton Conductors: Effects of Molecular Dynamics on the Proton Conductivity of Imidazolium Hydrogen Dicarboxylates” under review.

[Others]

1. Akira Ueda, Kouki Kishimoto, Yoshiya Sunairi, Junya Yoshida, Hiromichi Yamakawa, Tatsuya Miyamoto, Tsubasa Terashige, Hiroshi Okamoto and Hatsumi Mori, “Hysteretic Current–Voltage Characteristics in the Deuterium-Dynamics-Triggered Charge-Ordered Phase of κ -D₃(Cat-EDT-TTF)₂” J. Phys. Soc. Jpn., **88**, 034710 (2019).

Acknowledgements

The thesis is a summary of the author's studies from 2015 to 2020 at the Institute for Solid State Physics (ISSP), The University of Tokyo under the directions of Professor Hatsumi Mori. The author would like to express his gratitude to Professor Hatsumi Mori for her helpful advice.

The author is deeply grateful to Professor Osamu Yamamuro, Associate Professor Toshihiro Okamoto, Associate Professor Keiichi Inoue, and Associate Professor Kenichiro Hashimoto for their helpful advice and useful suggestion.

The author wishes to express his thankful acknowledgement to Dr. Shun Dekura, Dr. Tomoko Fujino for their useful suggestion. The author wishes to express his gratitude to Associate Professor Akira Ueda (Kumamoto University) for his useful suggestion.

The author is deeply grateful to Professor Motohiro Mizuno and Associate Professor Tomonori Ida (Kanazawa University) for their helps to measure the solid-state ^2H NMR spectroscopies. The grateful acknowledgement is also due to Nanotechnology Platform (the Institute for Molecular Science) for their supports to operate the variable-temperature X-ray diffraction experiments. The author wishes to express his grateful acknowledgement to Dr. Yuta Hori (University of Tsukuba) for his operation of theoretical analyses of infrared spectroscopies and energetic landscapes. The author is deeply grateful to Dr. Masato Matsuura and Dr. Takeshi Yamada (Comprehensive Research Organization for Science and Society) for their helps to measure the quasielastic neutron scattering.

The grateful acknowledgement is also due to Mrs. Akiko Kawai for her helps for accounting procedures of expenses involved with my research works.

The author would like to express his gratitude to Dr. Sang Chul Lee and Mr. Takahisa Shikama for their career advice.

The author wishes to express his gratitude to Dr. Toshiki Higashino, Dr Junya Yoshida, Dr. Dongwei Zhang, Mr. So Yokomori, Mr. Ryohei Kameyama, Mr. Takuya Terashi, Mr. Kouki Kishimoto, Mr. Ryohei Doi, Mr. Fumihito Takei, Mr. Toshinobu Takakura, Mr. Jun Ikeda, Mr. Yuta Sugai, Mr. Lei Zhang, Ms. Takako Noritomi, Ms. Natsumi Teraoka, and Mr. Yusuke Takahashi for their cooperation and enjoyable times at ISSP.

The author has been supported by many people who are neither staffs nor students of ISSP. He is also grateful to all friends of undergraduate school days at Tokyo University of Science and all fellows of my graduate school days at The University of Tokyo.

Last but not least, the author expresses his sincere gratitude to his family for their supports.

Chiba, February 2020